

# **Thermoelectric properties in phase-separated half-Heusler materials**

Dissertation zur Erlangung des Grades  
„Doktor der Naturwissenschaften“

im Promotionsfach Chemie  
am Fachbereich Chemie, Pharmazie und Geowissenschaften  
an der Johannes Gutenberg-Universität Mainz

vorgelegt von

**Julia Krez**

geboren in Kapal/Kasachstan



JOHANNES GUTENBERG  
UNIVERSITÄT MAINZ

Mainz 2014

## Abstract

The conversion of dissipated heat into electricity is the basic principle of thermoelectricity. In this context, half-Heusler (HH) compounds are promising thermoelectric (TE) materials for waste heat recovery. They meet all the requirements for commercial TE applications, ranging from good efficiencies via environmentally friendliness to being low cost materials. This work focused on the TE properties of  $\text{Ti}_{0.3}\text{Zr}_{0.35}\text{Hf}_{0.35}\text{NiSn}$ -based HH materials. This compound undergoes an intrinsic phase separation into a Ti-poor and Ti-rich HH phase during a rapid solidification process. The resulting dendritic microstructure causes a drastic reduction of the thermal conductivity, leading to higher TE efficiencies in these materials. The TE properties and temperature dependence of the phase-separated  $\text{Ti}_{0.3}\text{Zr}_{0.35}\text{Hf}_{0.35}\text{NiSn}$  compound were investigated. The TE properties can be adjusted depending on the annealing treatment. The extension of annealing time for 21 days at 1000 °C revealed a reduction of the thermal conductivity and thus an enhancement of the TE performance in this sample. An increase of annealing temperature caused a change of the phase fraction ratio in favor of the Ti-rich phase, leading to an improvement of the electronic properties.

Inspired by the TE properties of the  $\text{Ti}_{0.3}\text{Zr}_{0.35}\text{Hf}_{0.35}\text{NiSn}$  HH compound, the performance of different *n*- and *p*-type materials, realized via site substitution with donor and acceptor elements was examined. The fabrication of a TE *n*- and *p*-type material pair based on one starting compound can guarantee similar TE and mechanical properties and is enormous beneficial for device engineering. As donor dopants V, Nb and Sb were tested. Depending on the lattice position small doping levels were sufficient to attain distinct improvement in their TE efficiency. Acceptor-induced doping with Sc, Y and Co caused a change in the transport behavior from *n*- to *p*- type conduction, revealing the highest Seebeck coefficients obtained in the *MNiSn* system.

Then, the long-term stability of an exemplary *n*- and *p*-type HH compound was proven. Surprisingly, the dendritic microstructure can be maintained even after 500 cycles (1700 h) from 373 to 873 K. The TE performance of both *n*- and *p*-type materials showed no significant change under the long-term treatment, indicating the extraordinary temperature stability of these compounds. Furthermore both HH materials revealed similar temperature-dependence of their mechanical properties. This work demonstrates the excellent suitability of phase-separated HH materials for future TE applications in the moderate temperature range.

## Kurzzusammenfassung

Das grundlegende Prinzip der Thermoelektrik ist die Umwandlung verlorener Wärmeenergie in elektrischen Strom. Hierbei sind halb-Heusler (HH) Verbindungen vielversprechende Materialien, da sie viele der erforderlichen Kriterien, wie hohe thermoelektrische (TE) Effizienz, Umweltfreundlichkeit und geringe Materialkosten, für eine kommerzielle Anwendung erfüllen. Der Fokus dieser Arbeit liegt in der Untersuchung der TE Eigenschaften in  $\text{Ti}_{0.30}\text{Zr}_{0.35}\text{Hf}_{0.35}\text{NiSn}$ -basierenden HH Verbindungen. Diese Materialien separieren bei rascher Abkühlung in eine Ti-arme und Ti-reiche Phase. Die resultierende dendritische Mikrostruktur führt zu einer drastischen Reduzierung der thermischen Leitfähigkeit und ist ein entscheidender Faktor zur Erzielung hoher TE Effizienten in HH-Materialien. Die TE Eigenschaften und das Temperaturverhalten der phasenseparierten  $\text{Ti}_{0.3}\text{Zr}_{0.35}\text{Hf}_{0.35}\text{NiSn}$ -Verbindung wurden untersucht. Eine Temperaturbehandlung von 21 Tage bei  $1000\text{ }^{\circ}\text{C}$  zeigte eine Reduzierung der thermischen Leitfähigkeit und damit eine Verbesserung in der TE Effizienz. Die Erhöhung der Temperatur änderte das Phasen-Verhältnis in den Proben zugunsten der Ti-reicheren HH Phase, was eine Verbesserung der elektronischen Eigenschaften zur Folge hatte.

Inspiziert durch die TE Eigenschaften der  $\text{Ti}_{0.3}\text{Zr}_{0.35}\text{Hf}_{0.35}\text{NiSn}$ -Verbindung, wurde nach leistungsfähigen *n*- und *p*-typ Materialien via Substitution mit Donor- und Akzeptor-Elementen in diesem System gesucht. Die Herstellung eines TE *n*- und *p*-typ Materialpaares basierend auf einer Ausgangsverbindung ist sehr vorteilhaft für den Bau thermoelektrischer Module, da dadurch ähnliche TE und mechanische Eigenschaften gewährleistet werden können. Als Donatoren wurden V, Nb and Sb getestet, wobei bereits geringe Dotiermengen ausreichten, um eine erhebliche Steigerung der TE Leistung in den HH Proben zu erhalten. Akzeptoren wie Sc, Y und Co änderten die Transporteigenschaften von *n*- zu *p*-typ Verhalten. Dabei zeigten die *p*-typ Verbindungen die bisher höchsten Seebeck Koeffizienten basierenden auf dem *MNiSn*-System.

Desweiteren wurde die Langzeitstabilität einer exemplarischen *n*- und *p*-typ HH Verbindung untersucht. Die dendritische Mikrostruktur bleibt auch nach 500 Temperaturzyklen (1700 h) von 373 bis 873 K erhalten und die TE Effizienz beider Materialien zeigte keine signifikante Änderung nach der Langzeit-Behandlung auf. Zudem zeigten beide Materialien ähnliche mechanische Eigenschaften. Die außergewöhnliche Temperaturstabilität dieser HH-Verbindungen verdeutlicht die hervorragende Eignung phasenseparierter HH-Materialien für zukünftige TE Anwendungen im moderaten Temperaturbereich.

# Contents

Table of Contents

List of Publications

List of Figures

List of Tables

List of Symbols, Notations, and Abbreviations

<b>1</b>	<b>Introduction</b> .....	1
1.1	Thermoelectrics – A historical overview .....	1
1.2	Applicability of TE devices.....	5
<b>2</b>	<b>Thermoelectric properties</b> .....	9
2.1	Electronic Behavior .....	9
2.2	Thermal conductivity .....	13
2.3	Optimization of Figure of merit $zT$ .....	16
2.3.1	Enhancement of the electronic properties .....	16
2.3.2	Reduction of the thermal conductivity .....	19
<b>3</b>	<b>Half-Heusler materials</b> .....	21
3.1	Introduction .....	21
3.2	Half-Heusler materials for TE application .....	24
3.3	Phase separation in half-Heusler compounds.....	29
<b>4</b>	<b>Experimental methods</b> .....	32
4.1	Synthesis and chemical characterization .....	32
4.2	Thermal Transport measurements .....	34
<b>5</b>	<b>TE properties of <math>\text{Ti}_{0.3}\text{Zr}_{0.35}\text{Hf}_{0.35}\text{NiSn}</math></b> .....	36
5.1	Properties of $\text{Ti}_{0.3}\text{Zr}_{0.35}\text{Hf}_{0.35}\text{NiSn}$ HH compound .....	36
5.2	Influence of annealing time in $\text{Ti}_{0.3}\text{Zr}_{0.35}\text{Hf}_{0.35}\text{NiSn}$ .....	40
5.3	Influence of annealing temperature in $\text{Ti}_{0.3}\text{Zr}_{0.35}\text{Hf}_{0.35}\text{NiSn}$ .....	44
<b>6</b>	<b>Site substitution in <math>\text{Ti}_{0.3}\text{Zr}_{0.35}\text{Hf}_{0.35}\text{NiSn}</math></b> .....	48
6.1	Donor dopant-induced properties of $\text{Ti}_{0.3}\text{Zr}_{0.35}\text{Hf}_{0.35}\text{NiSn}$ .....	49
6.1.1	$\text{Ti}_{0.3-x}\text{V}_x\text{Zr}_{0.35}\text{Hf}_{0.35}\text{NiSn}$ ( $x= 0.01, 0.03$ and $0.05$ ) .....	49
6.1.2	$\text{Ti}_{0.3-x}\text{Nb}_x\text{Zr}_{0.35}\text{Hf}_{0.35}\text{NiSn}$ ( $x= 0.01, 0.03$ and $0.05$ ) .....	53

6.1.3	$\text{Ti}_{0.3}\text{Zr}_{0.35}\text{Hf}_{0.35}\text{NiSn}_{1-z}\text{Sb}_z$ ( $x= 0.001-0.01$ ).....	58
6.2	Acceptor dopant-induced properties of $\text{Ti}_{0.3}\text{Zr}_{0.35}\text{Hf}_{0.35}\text{NiSn}$ .....	62
6.2.1	$\text{Ti}_{0.3-x}\text{Sc}_x\text{Zr}_{0.35}\text{Hf}_{0.35}\text{NiSn}$ ( $x= 0.01-0.05$ ).....	62
6.2.2	$\text{Ti}_{0.3-x}\text{Y}_x\text{Zr}_{0.35}\text{Hf}_{0.35}\text{NiSn}$ ( $x= 0.01-0.20$ ).....	65
6.2.3	$\text{Ti}_{0.3}\text{Zr}_{0.35}\text{Hf}_{0.35}\text{Ni}_{1-y}\text{Co}_y\text{Sn}$ ( $x= 0.01-0.1$ ).....	68
7	<b>Compatibility of <i>n</i>- and <i>p</i>-type HH materials</b> .....	71
7.1	Mechanical properties .....	71
7.2	Long-term stability .....	73
7.3	Spark plasma sintering .....	77
8	<b>Conclusion</b> .....	81
	<b>Bibliography</b> .....	83
	<b>Curriculum Vitae</b>	

## Publications

1. **J. Krez**, B. Balke, C. Felser, W. Hermes and M. Schwind. Long-term stability in phase-separated half-Heusler materials, *Adv. Mater.* **2014** submitted.
2. **J. Krez**, J. Schmitt, G.J. Snyder, C. Felser, W. Hermes and M. Schwind, Optimization of the carrier concentration in phase-separated half-Heusler compounds, *J. Mater. Chem. A* **2014**, Accepted Manuscript DOI:10.1039/C4TA03000A.
3. L.M. Schoop, J.M. Allred, N. Ni, D. Hirai, **J. Krez**, M. Schwall, H. Ji, N.M. Ali and J.R. Cava,  $\beta$ -HfCuGe - A new polymorph of HfCuGe with a novel structure type, *J. Solid State Chem.* **2013**, 199, 66-70

## List of Figures

<b>Figure 1</b>	Energy split in internal combustion engines <sup>5</sup> .	1
<b>Figure 2</b>	Schematic of the Seebeck effect, Peltier effect and Thomson effect <sup>10</sup> .	2
<b>Figure 3</b>	Chronological overview of TE materials according their improvement in $zT$ <sup>24</sup> .	4
<b>Figure 4</b>	Illustration of a TE module <sup>20</sup> .	5
<b>Figure 5</b>	Illustration of a segmented TEG (left) and a cascaded TEG with a cascading ratio of three (right) <sup>28</sup> .	7
<b>Figure 6</b>	Overview of state-of-the-art $n$ -type (left) and $p$ -type (right) materials (26) with different figure of merit $zT$ maxima at different temperatures. The orange line corresponds to $zT = 1$ .	8
<b>Figure 7</b>	Illustration of the criteria for TE materials required for large-scale power generation.	8
<b>Figure 8</b>	Schematic of the band structure of metals, semiconductor and isolator depending on the atomic distance $d$ <sup>33</sup> .	9
<b>Figure 9</b>	Illustration of the transversal vibration of a) the optical phonons, where the atoms (filled and unfilled circle) oscillate in phase and b) the acoustic phonons with anharmonic oscillation of the atoms <sup>31</sup> .	14
<b>Figure 10</b>	Influence of charge carrier concentration on the Seebeck coefficient $\alpha$ , the electrical conductivity $\sigma$ , the thermal conductivity $\kappa$ and the Power factor $\alpha^2 \sigma$ <sup>20</sup> .	16
<b>Figure 11</b>	Schematic of the influence of multiple bands and resonant states on the density of states (DOS) <sup>37</sup> .	18
<b>Figure 12</b>	a) Brillouin zone of PbTe showing a low band degeneracy of $N_V$ equals 4 for the $L$ -point (orange) and 12 for the $\Sigma$ -point (blue), b) Temperature dependence of the two valance Bands <sup>37</sup> .	19
<b>Figure 13</b>	Ideal material property for a good TE material from the electrons perspective (right) and the phonon perspective (left) <sup>19</sup> .	19
<b>Figure 14</b>	Periodic table of elements including the crystal structure $F\bar{4}3m$ of zinc blende and HH compounds. The various number of HH compounds can be formed by combination of the different elements according the color scheme.	22
<b>Figure 15</b>	Electronic structure of ZrNiSn from <i>ab initio</i> calculations performed by Dr. G.H. Fecher at Max-Planck-Institute for Chemical Physics of Solids (Dresden) depending on Ni $\leftrightarrow$ Vac anti-site disorder. a) Ordered $C1_b$ structure. b) with 1% Ni $\leftrightarrow$ Vac anti-site disorder and c) with 10% Ni $\leftrightarrow$ Vac anti-site disorder.	23

- Figure 16** Electronic structure and the density of states (DOS) of TiNiSn<sup>63</sup>. 24
- Figure 17** Electronic structure of the *n*-type Ti<sub>0.30</sub>Zr<sub>0.35</sub>Hf<sub>0.35</sub>NiSn from *ab initio* calculations performed by Dr. G.H. Fecher at Max-Planck-Institute for Chemical Physics of Solids (Dresden). The Fermi energy is shifted into the conduction band with 10% Nb substitution and into the valence band with 10% Sc substitution. 26
- Figure 18** Influence of electronic doping on the Seebeck coefficient  $\alpha$ . The dashed lines indicate the band extrema of the valence and conduction band<sup>63</sup>. 27
- Figure 19** SEM image (BSE) of the *n*-type Ti<sub>0.3</sub>Zr<sub>0.35</sub>Hf<sub>0.35</sub>NiSn and *p*-type Ti<sub>0.26</sub>Sc<sub>0.04</sub>Zr<sub>0.35</sub>Hf<sub>0.35</sub>NiSn HH compounds. The samples were etched with a HCl:HNO<sub>3</sub>:HF:H<sub>2</sub>O solution to highlight the dendritic phase separation. 29
- Figure 20** Schematic the eutectic solidification of a binary compound under rapid cooling<sup>91</sup>. 31
- Figure 21** Picture of the arc melting setup taken at the University Mainz 32
- Figure 22** Illustration of the Seebeck coefficient  $\alpha$  and electrical conductivity  $\sigma$  measurement on the LSR-3 system, where the sample is clamped between two thermocouples. 34
- Figure 23** a) Schematic of the laser flash method in order to measure the thermal diffusivity  $D$ . A laser irradiates the graphite coated sample via short pulse, while the temperature on the other side of the sample is monitored by an IR detector b) Schematic of the DSC measurement in order to measure the specific heat  $c_p$  and the melting point. 35
- Figure 24** SEM image (BSE) of Ti<sub>0.3</sub>Zr<sub>0.35</sub>Hf<sub>0.35</sub>NiSn emphasizing the intrinsic phase separation in the Ti-poor HH 1 phase (grey) and the Ti-rich HH 2 phase (black), which is dendritically interlaced through the microstructure. 37
- Figure 25** DSC measurement of Ti<sub>0.3</sub>Zr<sub>0.35</sub>Hf<sub>0.35</sub>NiSn exemplifies the eutectic temperature at 1680 K and the melting point at 1780 K. The supercooled melt recrystallized at 1680 K. The peaks at 503 K indicate Sn impurities. 38
- Figure 26** Specific heat capacity  $c_p$  measurement of the *n*-type Ti<sub>0.3</sub>Zr<sub>0.35</sub>Hf<sub>0.35</sub>NiSn HH compound, indicating the Dulong-Petit limit of  $3R$  for  $T \gg \Theta_D$ . 38
- Figure 27** Normalized Kubelka Munk function of pure ZrNiSn and Ti<sub>0.3</sub>Zr<sub>0.35</sub>Hf<sub>0.35</sub>NiSn with the absorption coefficient including the linear fit (red dotted line) which was used to estimate the band gap from the Tauc method. 39
- Figure 28** Hall measurements of the *n*-type Ti<sub>0.3</sub>Zr<sub>0.35</sub>Hf<sub>0.35</sub>NiSn compound with the temperature dependence of the Hall carrier concentration  $n_H$  and the Hall mobility  $\mu_H$  from 300 to 900 K. 40
- Figure 29** PRXD pattern of Ti<sub>0.3</sub>Zr<sub>0.35</sub>Hf<sub>0.35</sub>NiSn samples annealed at 950°C for 3 and 7 days and at 1000 °C for 21 days. Black stars indicate Sn impurities, black rhombus indicate Hf<sub>5</sub>Sn<sub>3</sub> impurity phases. 40



- Figure 30** SEM images (BSE) of the *n*-type  $\text{Ti}_{0.3}\text{Zr}_{0.35}\text{Hf}_{0.35}\text{NiSn}$  samples. a) annealed for 3 days at 950°C, b) annealed for 7 days at 950 °C and c) annealed for 21 days at 1000 °C. 42
- Figure 31** Temperature dependence of the a) electrical conductivity  $\sigma(T)$ , b) Seebeck coefficient  $\alpha(T)$ , c) thermal conductivity  $\kappa(T)$  and d) figure of merit  $zT(T)$  in  $\text{Ti}_{0.3}\text{Zr}_{0.35}\text{Hf}_{0.35}\text{NiSn}$  samples from 300 to 900 K annealed for 3, 7 and 21 days. 43
- Figure 32** PRXD pattern of  $\text{Ti}_{0.3}\text{Zr}_{0.35}\text{Hf}_{0.35}\text{NiSn}$  samples annealed at different temperatures. Black stars indicate Sn impurities, black rhombus indicate  $\text{Hf}_5\text{Sn}_3$  impurity phases. 44
- Figure 33** SEM (BSE) images of  $\text{Ti}_{0.3}\text{Zr}_{0.35}\text{Hf}_{0.35}\text{NiSn}$  samples depending on annealing temperature. 46
- Figure 34** Temperature dependence of the a) electrical conductivity  $\sigma(T)$ , b) Seebeck coefficient  $\alpha(T)$  and c) Power factor  $\alpha^2\sigma(T)$  in  $\text{Ti}_{0.3}\text{Zr}_{0.35}\text{Hf}_{0.35}\text{NiSn}$  samples annealed at different temperatures from 300 to 900 K. 47
- Figure 35** Schematic of the site substitution in the  $\text{Ti}_{0.3}\text{Zr}_{0.35}\text{Hf}_{0.35}\text{NiSn}$  HH compound. 49
- Figure 36** SEM (BSE) images of a)  $\text{Ti}_{0.29}\text{V}_{0.01}\text{Zr}_{0.35}\text{Hf}_{0.35}\text{NiSn}$  and b)  $\text{Ti}_{0.25}\text{V}_{0.05}\text{Zr}_{0.35}\text{Hf}_{0.35}\text{NiSn}$  sample. 50
- Figure 37** Temperature dependence of the a) electrical conductivity  $\sigma(T)$ , b) Seebeck coefficient  $\alpha(T)$ , c) Power factor  $\alpha^2\sigma(T)$  and d) thermal conductivity  $\kappa(T)$  in  $\text{Ti}_{0.3-x}\text{V}_x\text{Zr}_{0.35}\text{Hf}_{0.35}\text{NiSn}$  ( $x = 0, 0.01, 0.03$  and  $0.05$ ) samples from 300 to 900 K. 51
- Figure 38** Hall measurements of the  $\text{Ti}_{0.3-x}\text{V}_x\text{Zr}_{0.35}\text{Hf}_{0.35}\text{NiSn}$  ( $x = 0, 0.01$  and  $0.05$ ) samples. a) Hall carrier concentration  $n_H$  and b) Hall mobility  $\mu_H$  from 300 to 900 K. 52
- Figure 39** Temperature dependence of the figure of merit  $zT(T)$   $\text{Ti}_{0.3-x}\text{V}_x\text{Zr}_{0.35}\text{Hf}_{0.35}\text{NiSn}$  ( $x = 0, 0.01, 0.03$  and  $0.05$ ) samples from 300 to 900 K. 52
- Figure 40** Light microscope image of the  $\text{Ti}_{0.25}\text{Nb}_{0.05}\text{Zr}_{0.35}\text{Hf}_{0.35}\text{NiSn}$  sample etched with a  $\text{HCl}:\text{HNO}_3:\text{HF}:\text{H}_2\text{O}$  solution to emphasize the metallic Nb inclusions. 53
- Figure 41** Temperature dependence of the a) electrical resistivity  $\rho(T)$ , b) Seebeck coefficient  $\alpha(T)$ , c) Power factor  $\alpha^2\sigma(T)$  and d) thermal conductivity  $\kappa(T)$  figure of merit  $zT(T)$  in  $\text{Ti}_{0.3-x}\text{Nb}_x\text{Zr}_{0.35}\text{Hf}_{0.35}\text{NiSn}$  ( $x = 0, 0.01, 0.03$  and  $0.05$ ) samples from 300 to 900 K. 55
- Figure 42** Temperature dependence of a) the Hall carrier concentration  $n_H$  and b) the Hall mobility  $\mu_H$  in  $\text{Ti}_{0.3-x}\text{Nb}_x\text{Zr}_{0.35}\text{Hf}_{0.35}\text{NiSn}$  ( $x = 0, 0.01, 0.03$  and  $0.05$ ) samples from 300 to 900 K. 56
- Figure 43** a) Seebeck coefficient  $\alpha$  vs carrier concentration together with a comparison of literature data (83; 101) and b) the average mass model (solid line) to estimate the optimized carrier concentration for the  $\text{Ti}_{0.3-x}\text{Nb}_x\text{Zr}_{0.35}\text{Hf}_{0.35}\text{NiSn}$  system. The model is consistent in good agreement with values taken from <sup>83,101</sup>. 57
- Figure 44** Temperature dependence of the figure of merit  $zT(T)$  in  $\text{Ti}_{0.3-x}\text{Nb}_x\text{Zr}_{0.35}\text{Hf}_{0.35}\text{NiSn}$  ( $x = 0, 0.01, 0.03$  and  $0.05$ ) samples from 300 to 900 K. 57

- Figure 45** SEM (BSE) image of  $\text{Ti}_{0.3}\text{Zr}_{0.35}\text{Hf}_{0.35}\text{NiSn}_{0.99}\text{Sb}_{0.01}$  sample. 58
- Figure 46** Temperature dependence of the a) electrical resistivity  $\rho(T)$ , b) Seebeck coefficient  $\alpha(T)$ , c) Power factor  $\alpha^2\sigma(T)$  and d) thermal conductivity  $\kappa(T)$  in  $\text{Ti}_{0.3}\text{Zr}_{0.35}\text{Hf}_{0.35}\text{NiSn}_{1-x}\text{Sb}_x$  ( $x = 0, 0.001, 0.002, 0.006$  and  $0.01$ ) samples from 300 to 900 K. 60
- Figure 47** Temperature dependence of the figure of merit  $zT(T)$  in  $\text{Ti}_{0.3}\text{Zr}_{0.35}\text{Hf}_{0.35}\text{NiSn}_{1-x}\text{Sb}_x$  ( $x = 0, 0.001, 0.002, 0.006$  and  $0.01$ ) samples from 300 to 900 K. 61
- Figure 48** SEM (BSE) image of  $\text{Ti}_{0.3-x}\text{Sc}_x\text{Zr}_{0.35}\text{Hf}_{0.35}\text{NiSn}$  sample. 62
- Figure 49** Hall measurements of  $\text{Ti}_{0.3-x}\text{Sc}_x\text{Zr}_{0.35}\text{Hf}_{0.35}\text{NiSn}$  ( $x = 0-0.05$ ) samples. a) Hall carrier concentration  $n_H$  and b) Hall mobility  $\mu_H$  from 300 to 900 K. 63
- Figure 50** Temperature dependence of a) electrical conductivity  $\sigma(T)$ , b) Seebeck coefficient  $\alpha(T)$ , c) Power factor  $\alpha^2\sigma(T)$  and d) thermal conductivity  $\kappa(T)$  in the  $\text{Ti}_{0.3-x}\text{Sc}_x\text{Zr}_{0.35}\text{Hf}_{0.35}\text{NiSn}$  ( $x = 0-0.05$ ) HH compound from 300 to 900 K. 64
- Figure 51** Temperature dependence of the figure of merit  $zT(T)$  of the  $\text{Ti}_{0.3-x}\text{Sc}_x\text{Zr}_{0.35}\text{Hf}_{0.35}\text{NiSn}$  ( $x = 0-0.05$ ) HH samples from 300 to 900 K. 65
- Figure 52** SEM (BSE) images of a)  $\text{Ti}_{0.26}\text{Y}_{0.04}\text{Zr}_{0.35}\text{Hf}_{0.35}\text{NiSn}$  and b)  $\text{Ti}_{0.15}\text{Y}_{0.15}\text{Zr}_{0.35}\text{Hf}_{0.35}\text{NiSn}$ . 66
- Figure 53** Temperature dependence of the a) electrical conductivity  $\sigma(T)$ , b) Seebeck coefficient  $\alpha(T)$ , c) Power factor  $\alpha^2\sigma(T)$  and d) thermal conductivity  $\kappa(T)$  in  $\text{Ti}_{0.3-x}\text{Y}_x\text{Zr}_{0.35}\text{Hf}_{0.35}\text{NiSn}$  ( $x = 0-0.20$ ) samples from 300 to 900 K. 67
- Figure 54** Temperature dependence of the figure of merit  $zT(T)$  of the  $\text{Ti}_{0.3-x}\text{Y}_x\text{Zr}_{0.35}\text{Hf}_{0.35}\text{NiSn}$  ( $x = 0-0.20$ ) HH compounds from 300 to 900 K. 67
- Figure 55** SEM (BSE) image of the  $\text{Ti}_{0.3}\text{Zr}_{0.35}\text{Hf}_{0.35}\text{Ni}_{0.99}\text{Co}_{0.01}\text{Sn}$  sample. 68
- Figure 56** Temperature dependence of the a) electrical conductivity  $\sigma(T)$ , b) Seebeck coefficient  $\alpha(T)$ , c) Power factor  $\alpha^2\sigma(T)$  and d) thermal conductivity  $\kappa(T)$  in  $\text{Ti}_{0.3}\text{Zr}_{0.35}\text{Hf}_{0.35}\text{Ni}_{0.99}\text{Co}_{0.01}\text{Sn}$  ( $x = 0-0.10$ ) samples from 300 to 900 K. 69
- Figure 57** Temperature dependence of the figure of merit  $zT(T)$  of the  $\text{Ti}_{0.3}\text{Zr}_{0.35}\text{Hf}_{0.35}\text{Ni}_{0.99}\text{Co}_{0.01}\text{Sn}$  ( $x = 0-0.20$ ) samples from 300 to 900 K. 70
- Figure 58** Micro-Hardness measurements of the *n*-type  $\text{Ti}_{0.3}\text{Zr}_{0.35}\text{Hf}_{0.35}\text{NiSn}$  and *p*-type  $\text{Ti}_{0.26}\text{Sc}_{0.04}\text{Zr}_{0.35}\text{Hf}_{0.35}\text{NiSn}$  material according to Vickers (HV 0.3) . 72
- Figure 59** Measurement of the thermal expansion coefficient  $\gamma$  in the *n*-type  $\text{Ti}_{0.3}\text{Zr}_{0.35}\text{Hf}_{0.35}\text{NiSn}$  and *p*-type  $\text{Ti}_{0.26}\text{Sc}_{0.04}\text{Zr}_{0.35}\text{Hf}_{0.35}\text{NiSn}$  material. 72
- Figure 60** Cycling conditions of the long-term stability test in the *n*-type  $\text{Ti}_{0.3}\text{Zr}_{0.35}\text{Hf}_{0.35}\text{NiSn}$  and *p*-type  $\text{Ti}_{0.26}\text{Sc}_{0.04}\text{Zr}_{0.35}\text{Hf}_{0.35}\text{NiSn}$  material. 73

- Figure 61** SEM images of the *n*-type  $\text{Ti}_{0.3}\text{Zr}_{0.35}\text{Hf}_{0.35}\text{NiSn}$  material a) before cycling b) after 500 cycles and of the *p*-type  $\text{Ti}_{0.26}\text{Sc}_{0.04}\text{Zr}_{0.35}\text{Hf}_{0.35}\text{NiSn}$  material after c) before cycling and d) after 500 cycles. 74
- Figure 62** TEM image of  $\text{Ti}_{0.3}\text{Zr}_{0.35}\text{Hf}_{0.35}\text{NiSn}$  after long-term annealing for 500 cycles, indicating dislocation defects in the microstructure. 75
- Figure 63** Temperature dependence of a) electrical conductivity  $\sigma(T)$ , b) Seebeck coefficient  $\alpha(T)$ , c) thermal conductivity  $\kappa(T)$  and d) figure of merit  $zT(T)$  in *n*-type  $\text{Ti}_{0.3}\text{Zr}_{0.35}\text{Hf}_{0.35}\text{NiSn}$  material after 50, 100 and 500 cycles from 300 to 900 K. 76
- Figure 64** Temperature dependence of a) electrical conductivity  $\sigma(T)$ , b) Seebeck coefficient  $\alpha(T)$ , c) thermal conductivity  $\kappa(T)$  and d) figure of merit  $zT(T)$  in the *p*-type  $\text{Ti}_{0.26}\text{Sc}_{0.04}\text{Zr}_{0.35}\text{Hf}_{0.35}\text{NiSn}$  material after 50, 100 and 500 cycles from 300 to 900 K. 77
- Figure 65** SEM (BSE) image of the *n*-type  $\text{Ti}_{0.3}\text{Zr}_{0.35}\text{Hf}_{0.35}\text{NiSn}$  sample after spark plasma sintering. 78
- Figure 66** Temperature dependence of a) electrical conductivity  $\sigma(T)$ , b) Seebeck coefficient  $\alpha(T)$ , c) thermal conductivity  $\kappa(T)$  and d) figure of merit  $zT(T)$  in the *n*-type  $\text{Ti}_{0.3}\text{Zr}_{0.35}\text{Hf}_{0.35}\text{NiSn}$  material after spark plasma sintering from 300 to 900 K. 79
- Figure 67** Temperature dependence of a) electrical conductivity  $\sigma(T)$ , b) Seebeck coefficient  $\alpha(T)$ , c) thermal conductivity  $\kappa(T)$  and d) figure of merit  $zT(T)$  in the *p*-type  $\text{Ti}_{0.26}\text{Sc}_{0.04}\text{Zr}_{0.35}\text{Hf}_{0.35}\text{NiSn}$  material after spark plasma sintering from 300 to 900 K. 80

## List of Tables

<b>Table 1</b>	List of elements used for the preparation of the HH compounds	33
<b>Table 2</b>	Lattice parameter, chemical composition and phase fraction of the Ti-poor HH 1 and Ti-rich HH 2 phase in $\text{Ti}_{0.3}\text{Zr}_{0.35}\text{Hf}_{0.35}\text{NiSn}$ depending on the annealing time.	41
<b>Table 3</b>	Lattice parameter and phase fraction of the Ti-poor HH 1 and Ti-rich HH 2 phase in $\text{Ti}_{0.3}\text{Zr}_{0.35}\text{Hf}_{0.35}\text{NiSn}$ HH depending on the annealing temperature.	45
<b>Table 4</b>	Lattice parameters and chemical compositions determined using energy dispersive X-ray analysis of phase-separated <i>n</i> -type $\text{Ti}_{0.3}\text{Zr}_{0.35}\text{Hf}_{0.35}\text{NiSn}$ and <i>p</i> -type $\text{Ti}_{0.26}\text{Sc}_{0.04}\text{Zr}_{0.35}\text{Hf}_{0.35}\text{NiSn}$ HH compounds.	74

## List of Symbols, Notations, and Abbreviations

$\alpha$	Seebeck coefficient or thermopower	BSE	Back scattering electrons
$\gamma$	Thermal expansion coefficient	DoE	US Department of Energy
$^{\circ}\text{C}$	Degree Celcius	DOS	Density of states
$c_p$	Specific heat	DSC	Differential scanning calorimetry
$D$	Diffusivity	EMPA	Electron microscope phase analysis
$\delta\mu$	Chemical potential	LFA	Laser flash apparatus
$\Theta_D$	Debye temperature	LSR	Linseis Seebeck Resistivity device
$\eta$	Thermoelectric efficiency	PGEC	Phonon Glass Electron Crystal
$e$	Elementary charge	PPMS	Physical properties measurement system
$E_F$	Fermi level	PXRD	Powder X-ray diffraction
eV	Electron Volt	SEM	Scanning electron microscopy
$PF$	Power factor	TE	Thermoelectric
$I$	Electrical current	TEG	Thermoelectric generator
K	Kelvin	TM	Transition metal
$k_b$	Boltzmann constant	$zT$	Material figure of merit
$\kappa$	Thermal conductivity	$ZT$	Device figure of merit
$\kappa_e$	Electrical thermal conductivity		
$\kappa_{la}$	Lattice thermal conductivity		
$l$	mean free path		
$L$	Lorentz number		
$m^*$	effective mass		
$n$	Carrier concentration		
$N_v$	Band degeneracy		
$\mu$	Carrier mobility		
$v_g$	Group velocity		
$\rho$	Density		
$\sigma$	Electrical conductivity		
$\tau$	Relaxation time		
$\Delta E_g$	Energy band gap		
$\Delta T$	Temperature gradient		
$\Gamma$	Peltier coefficient		
$\Pi$	Thomson coefficient		
$Q$	Heat		
$T$	Temperature		
$V$	Voltage		

## **Declaration**

Hiermit erkläre ich, dass ich die vorliegende Doktorarbeit selbstständig angefertigt habe. Es wurden nur die in der Arbeit ausdrücklich benannten Quellen und Hilfsmittel benutzt. Wörtlich oder sinngemäß übernommenes Gedankengut habe ich als solches kenntlich gemacht.

Hereby, I affirm that I wrote this work independently. Just specifically marked references and sources have been used for this thesis. Literally or analogously transferred ideas have been indicated as well.

Mainz, 26.05.2014

---

Julia Krez

# 1 Introduction

## 1.1 Thermoelectrics – A historical overview

The search for alternative energy technologies has taken an accelerated pace in recent years as climate change has become more noticeable and the use of nuclear energy introduces political controversy for many countries. The quest for sustainable energy sources has piqued interest in different research fields to find new energy conversion techniques to satisfy the world's rising demand for energy. The Sankey diagram, shown in Figure 1, exemplifies the necessity of energy recovery in conventional consumption processes, since most of the energy is dissipated as waste heat and only 25% is used as mechanical power<sup>1</sup>. However, the challenge is to find a suitable energy conversion technique, which can compete with the efficiency of fossil fuel combustion. In 2008 the DOE (US Department of Energy) has revealed, that about one-third of the energy in the US is consumed by the industrial sector. Depending on the process conditions 20–50% of the used energy is lost as waste heat and 40% of the exhaust gas has a temperature over 230 °C<sup>2,3</sup>. Therefore, a useful tool for the recuperation of thermal energy into electricity may be a thermoelectric generator (TEG)<sup>4</sup>.

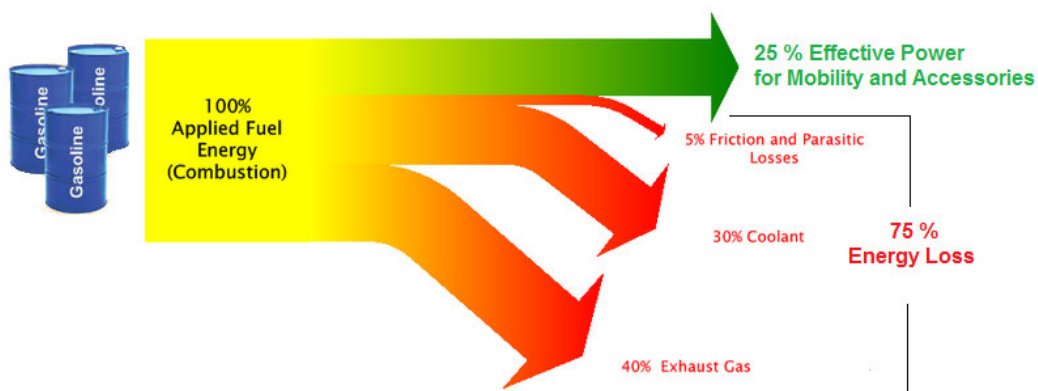


Figure 1 Energy split in internal combustion engines<sup>5</sup>.

Presently, thermoelectric (TE) devices are actively considered as a clean energy source for waste heat recovery. Furthermore they can make a crucial contribution to an improvement in fuel economy, and thus a reduction of CO<sub>2</sub> emissions<sup>4</sup>. Since the European Parliament has restricted the CO<sub>2</sub>-emissions for new automobiles to 95 g/km by 2020, the automobile industry is extremely interested in the applicability of TE devices<sup>6</sup>. In particular, a TEG operates silently, does not have any moving parts or environmentally harmful fluids and has

the ability to generate electricity from exhaust gas without additional engine load<sup>1</sup>. Hence, the captured energy can be used for a vehicle’s electrical components such as air conditioning, lights and windows and therefore contribute to both fuel and emission saving<sup>7</sup>. In order to understand the functionality of a TEG, it is crucial to understand the fundamental theory of thermoelectricity, which is discussed below based on the three TE effects - the *Seebeck effect*, *Peltier effect* and *Thomson effect*.

In 1821<sup>8</sup>, Thomas Johann *Seebeck*, observed an electric voltage  $\Delta V$ , when he applied a temperature gradient  $\Delta T$  along an electric circuit consisting of dissimilar electrical conductors A and B. Whereby, the generated voltage was proportional to the developed temperature difference. The arrangement of such a thermocouple is shown in Figure 2. The ratio of  $\Delta V/\Delta T$  is defined as the Seebeck coefficient  $\alpha$ , or thermopower, and strongly depends on the intrinsic properties of the TE material. A few years later the French physicist, Jean-Charles *Peltier*, showed that an applied electric current through a thermocouple generates a small heating or cooling effect depending on its direction, where the quotient of the transported heat  $Q$  to the external current  $I$  through the junction is define as the Peltier coefficient  $\Pi$ . First, it was not immediately understood that the Seebeck effect and the Peltier effect are thermodynamically reversible. More than 30 years after Seebeck’s discovery of the first TE effect, *William Thomson* realized that there must be a relationship between the Seebeck and the Peltier effect and established the third TE effect, now known as the Thomson effect. The Thomson effect describes that a material exhibits reversible heating or cooling by applying an electrical current and a temperature gradient<sup>9</sup>. Thus, the Thomson coefficient  $\Gamma$  relates to the change in heat  $Q$  transported by  $I$  along  $\Delta T$ .

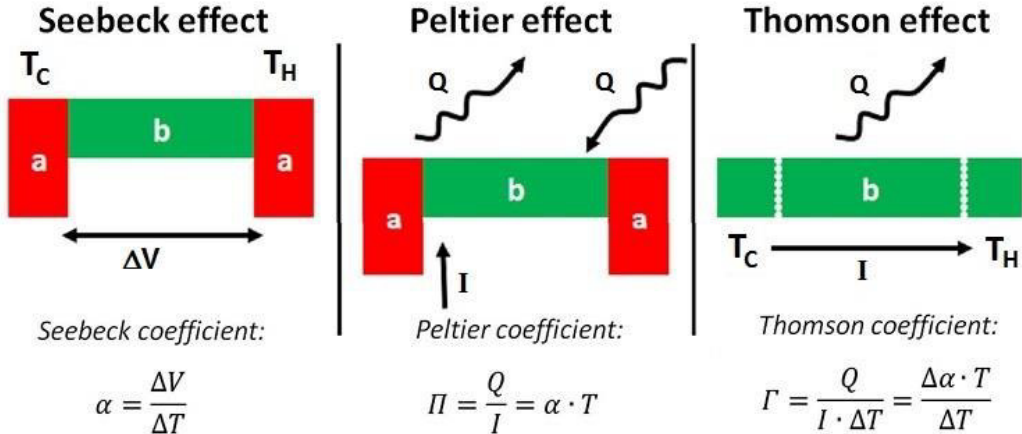


Figure 2 Schematic of the Seebeck effect, Peltier effect and Thomson effect<sup>10</sup>.



In 1911 *Altenkirch*<sup>11</sup> introduced the concept of the figure of merit  $zT$ , which has since been a benchmark for researchers in the development of TE materials. The quality factor  $zT$  of individual materials for TE applications is given by Equation (1):

$$zT = \frac{\alpha^2 \sigma}{\kappa} T = \frac{\alpha^2}{\rho \kappa} T \quad (1)$$

with the Seebeck coefficient  $\alpha$ , the electrical conductivity  $\sigma$ , the electrical resistivity  $\rho$ , the thermal conductivity  $\kappa$  and the temperature  $T$ . Under consideration of all TE parameters (Equation 1) it is obvious that high  $zT$  values can be achieved with a high Seebeck coefficient, high electrical conductivity and low thermal conductivity. A high electrical conductivity is required to minimize Joule heating, while a low thermal conductivity retains the heat junctions and maintains a large temperature gradient<sup>11,12</sup>. A more detailed discussion of the transport properties is given in section 2.

The pioneer in introducing semiconductors as promising materials for TE application was *A.Ioffe*<sup>13,14</sup>. His work led to a very active period in TE research in the 1950s and early 1960s, when many new TE materials were discovered and investigated. At this time, *H.J. Goldsmid* and coworkers<sup>15</sup> showed the high potential of  $\text{Bi}_2\text{Te}_3$  as a TE material, and this material remains the basis for the TE industry up to the present time. *Ioffe's* proposal to employ semiconductor alloys rather than simple binary compounds in order to lower the thermal conductivity lead to today's huge variety of material classes such as skutterudites, clathrates, half-Heusler alloys and complex chalcogenides as promising candidates for TE application. An extensive overview of all material classes and their TE properties can be found in<sup>16,17,18</sup>. Guided by the figure of merit  $zT$ , the most promising materials with high  $zT$  seems to be narrow band gap semiconductors with heavy elements and complex unit cells.

*G. Slack* condensed the requirements for a suitable TE material and established the idea of a phonon-glass electron-crystal (PGEC)<sup>19</sup>. Hence, in order to optimize the figure of merit, the TE compound should have the electrical properties of a crystal and the thermal properties of an amorphous or glass-like material. In other words, it is necessary to separate the electrical and the thermal conductivity, which is not trivial since they are directly related. Until the 1990s, the prevailing opinion was that this conductivity dilemma is unsolvable and caused a decline in the development of efficient thermoelectric materials. Then materials were discovered, in which the electric and thermal conductivity was partially decoupled, leading to a revival in the TE research community<sup>20</sup>. The theoretical predictions by *Dresselhaus* in the

early 1990s suggested that the TE efficiency could be greatly enhanced by quantum confinement of the electron charge carriers<sup>21,22</sup>. The electron energy bands in a quantum-confined structure are progressively narrower as the confinement increases and the dimensionality decreases<sup>20</sup>, leading to an enhancement in the electronic properties in the TE material. These predictions have stimulated a new wave of interest in complex TE materials, where the realization of new ideas mainly emerges from interdisciplinary collaborations between chemistry, physics and material science. Thus, a materials engineering approach must be pursued to either enhance more established materials or to discover completely new classes of materials.

In fact, little enhancement in highly efficient TE materials has been made in the past six decades, because improvement of one TE parameter leads to a deleterious effect on the other. Thus, the figure of merit of the TE compounds for industrial applications has remained static with  $zT \sim 1$  for a temperature difference  $\Delta T = 300$  K. Although the development of a good TE material is challenging, at least on a laboratory scale many new ideas has led to high performance TE materials ( $zT > 1$ )<sup>23</sup>. A chronological progress in the development of TE materials is shown in Figure 3.

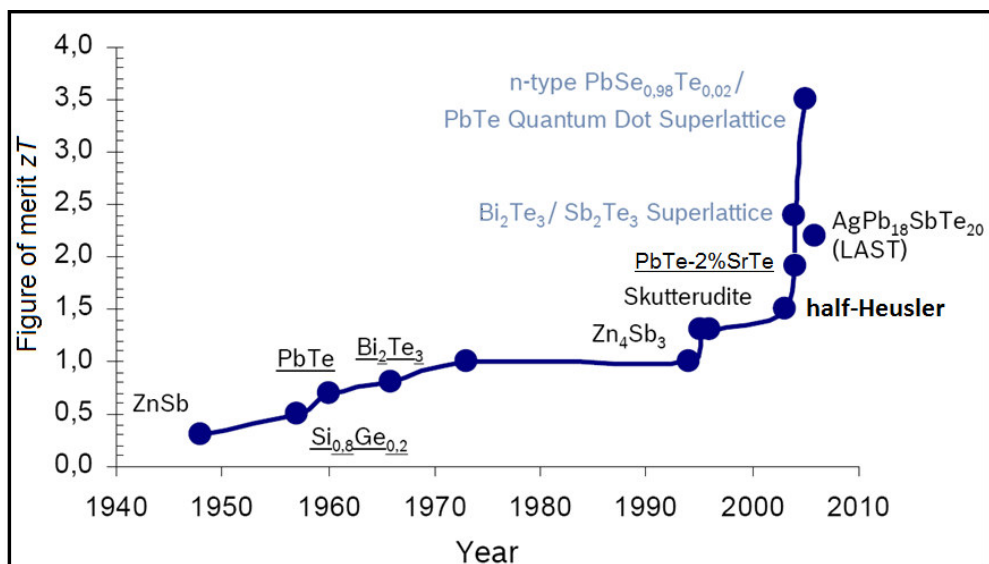


Figure 3 A chronological overview of TE materials according their improvement in  $zT$ <sup>24</sup>.

## 1.2 Applicability of TE devices

A commercially available TE module for power generation or cooling, as shown in Figure 4, consists of many  $n$ - and  $p$ -doped semiconductors, so called TE elements. Each TE element is connected by metal contacts and is sandwiched between electrically insulating ceramic plates, which are high thermal conductive<sup>20</sup>. It is important that the contact material is rigid and exhibits similar thermal expansion coefficients to avoid contact cracks. The TE elements are connected electrically in series but thermally in parallel, to optimize the heat flow from the hot to the cold end<sup>16</sup>. Considering the Seebeck effect, the temperature gradient drives charge carriers from the hot end to the cold end in the material, where the rejected heat must be removed by a heat sink<sup>20</sup>. Thus, electrons diffuse from the hot to the cold end in the  $n$ -type material, and holes in the  $p$ -type material, respectively.

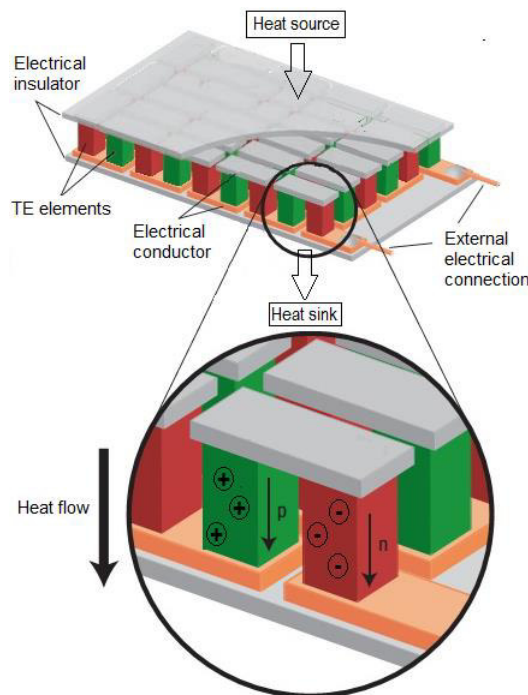


Figure 4 Illustration of a TE module<sup>20</sup>.

However, the information about a single material  $zT$  is meaningless for the determination of this material in a TE device, since an array of TE elements is utilized in a module. Therefore, it is necessary to distinguish between the value of the material's  $zT$ , which is typically higher, and the effective device,  $ZT$ . The difference arises on one hand from the temperature dependence in the transport properties, and on the other hand from the parasitic losses in the device including contact resistance and radiation effects. For instance, the state-of-the-art TE

material Bi<sub>2</sub>Te<sub>3</sub> with a maximum  $zT$  value of 1.1, exhibits an effective device  $ZT$  of only 0.7<sup>20</sup>. Hence the effective device  $ZT$  depends on the number of  $n$ -type and  $p$ -type TE elements in the TEG and is given by Equation 2:

$$ZT = \frac{(\alpha_p \sigma_p)^2 + (\alpha_n \sigma_n)^2}{(\kappa_p + \kappa_n)} T = \frac{(\alpha_p - \alpha_n)^2}{(\rho_p \kappa_p) + (\rho_n \kappa_n)} T \quad (2)$$

The TE efficiency  $\eta_{TE}$  of a TEG, given in Equation 3, is defined by the power input to the load ( $P$ ) over the net heat flow rate ( $Q$ ).

$$\eta_{TE} = \frac{P}{Q} \quad (3)$$

Like all heat engines<sup>20</sup>, the TE device is also limited, according to the laws of thermodynamics by the Carnot efficiency  $\eta_c$  described in Equation 4:

$$\eta_c = \frac{T_H - T_C}{T_H} \quad (4)$$

Thus, the maximum efficiency  $\eta_{TE}$  for a TE device is defined in Equation 5 through the Carnot efficiency  $\eta_c$  and the effective device  $ZT$  (20), and can be written as:

$$\eta_{TE} = \frac{T_H - T_C}{T_H} \cdot \frac{\sqrt{1 + ZT} - 1}{\sqrt{1 + ZT} + \frac{T_C}{T_H}} \quad (5)$$

To break out of the limited applicability of TE devices and realize adoption in other application fields, it is clear that the TE efficiency of a TEG must be increased. The theoretical assumption is that doubling of the device  $ZT$  up to 2 could lead to a tenfold increase in the number of TE purposes<sup>25</sup>. Therefore, the main efforts in TEG optimization are focused on the combination of different materials, which have high TE performance at different temperatures in order to obtain high TE efficiency over a wide temperature range. This can be accomplished by e.g. cascaded or segmented generators, where the  $n$ - and  $p$ -type TE elements (or TE legs) are combined with different materials and joined in series<sup>26</sup>. Ideally, the segmentation helps to improve the TE efficiency, if both materials are operating in their most efficient temperature range. Several studies<sup>25,26,27</sup> have reported, that the segmentation of the state-of-the-art TE materials ( $zT \sim 1$ ) leads to an increase in the efficiency from 10% to 15%. Ngan *et al*<sup>26</sup> have shown that the segmentation of  $p$ -type materials gives a higher boost in efficiency than  $n$ -type materials.

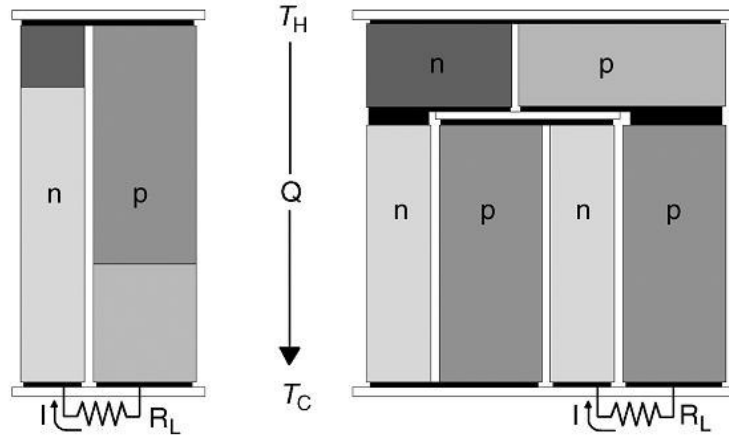


**Figure 5** Illustration of a segmented TEG (left) and a cascaded TEG with a cascading ratio of three (right)<sup>28</sup>.

In a segmented arrangement, shown in Figure 5, each  $p$ - and  $n$ -type leg is subdivided into segments made from different materials. Only a single electrical circuit is used to tap the TE voltage. Thus, the compatibility of the materials is most important here because the TE material properties may change dramatically from one segment to another<sup>28</sup>. A cascade TE module consists of different stages with each stage comprised of  $n$ - and  $p$ -type legs, which are formed from a single  $n$ - and  $p$ -type material. Each stage has its own independent electrical circuit, and thus the compatibility issue plays a minor role here.

Beside waste heat recovery, thermoelectric (TE) devices have been investigated for their use in TE-solar hybrid systems (4), TE-refrigeration<sup>29</sup> and as radioisotope TEGs for deep-space application of NASA's Voyager and Cassini missions<sup>30</sup>. However, the biggest interest for various TE applications requires materials with peak  $zT$  values at different temperatures. In Figure 6 it can be seen, that  $\text{Bi}_2\text{Te}_3$  based compounds are the best performing materials below 500 K, whereas the majority of materials, like PbTe,  $\text{Zn}_4\text{Sb}_3$ , Skutterudites,  $\text{Cu}_2\text{Se}$ , and half-Heusler compounds exhibit peak  $zT$  values in the medium temperature range (500-800 K). For higher temperatures up to 1200 K, Zintl compounds ( $p$ -type) and SiGe are an appropriate material choice<sup>10,26</sup>.

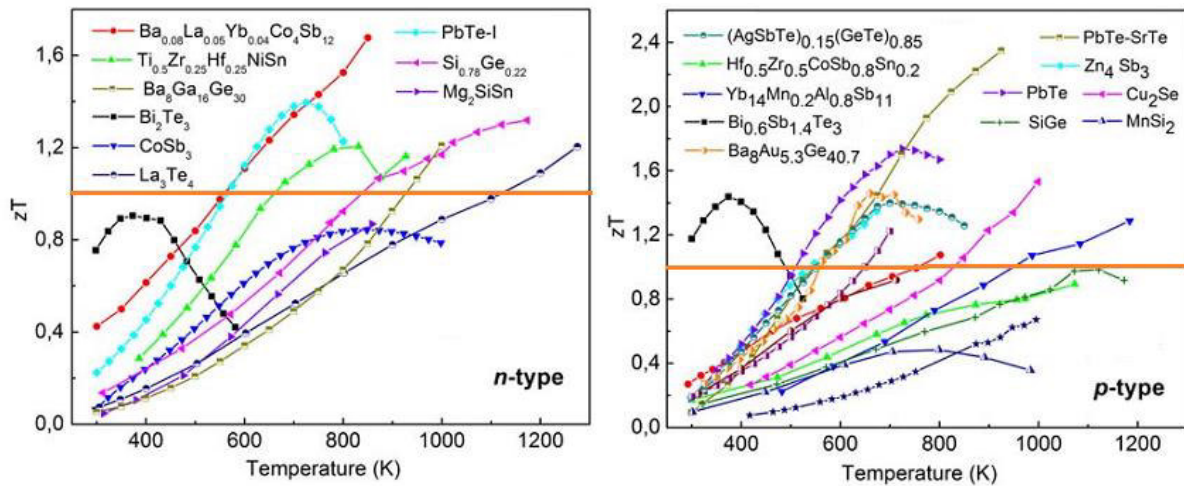


Figure 6 Overview of state-of-the-art *n*-type (left) and *p*-type (right) materials (26) with different figure of merit  $zT$  maxima at different temperatures. The orange line corresponds to  $zT = 1.26$ .

Although  $\text{Bi}_2\text{Te}_3$  and  $\text{PbTe}$  are high performance TE materials and represent the present materials for commercial TE power generation, a general application becomes more difficult, because Te is a rare and the environmentally friendliness of Pb and Bi is questionable. For any TE material to become viable for future applications, it needs to fulfill a set of criteria (Figure 7), beyond those of being an efficient TE material. A commercial and nationwide application of a TE material has to meet the requirements of being non-toxic, cheap and earth abundant, mechanically and thermally stable and furthermore provide the possibility of processable and reproducible high volume manufacturing.

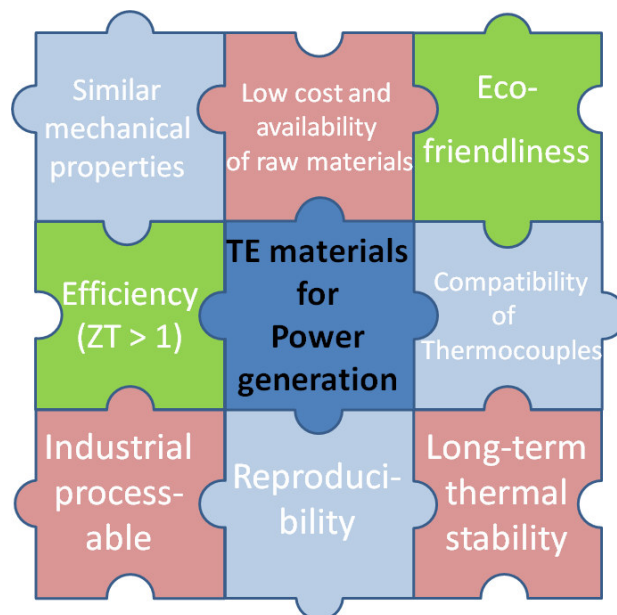


Figure 7 Illustration of the criteria for TE materials required for large-scale power generation.

## 2 Thermoelectric properties

### 2.1 Electronic behavior

The electronic properties in a TE material are mainly given by the Seebeck coefficient  $\alpha$  or thermopower and the electrical conductivity  $\sigma$ . First of all, it is useful to define the difference between a metal, semiconductor and an insulator. One distinctive feature is the size of the band gap  $\Delta E_g$ , which is illustrated in Figure 8. In general, a metal does not have an energy gap between the low energy valence band and the high energy conduction band. A material with semiconducting behavior can exhibit band gaps  $\Delta E_g$  from 0.1 to 4 eV, whereas materials with  $\Delta E_g > 4$  eV are insulating with poor conducting properties<sup>31</sup>. Furthermore, a distinction can be made depending on the carrier concentration  $n$  in a material. In a metal, many carriers and states, typically  $n \approx 10^{22}$  carriers  $\text{cm}^{-3}$ , are available for conduction, thus the electrical conductivity in metals is very high, on the order of  $10^6$  S/cm<sup>3</sup>. The carrier concentration  $n$  for an intrinsic semiconductor is about  $n \approx 10^{13}$ - $10^{15}$  carriers  $\text{cm}^{-3}$ , while a doped semiconductor typically exhibits values of  $n \approx 10^{16}$ - $10^{21}$  carriers  $\text{cm}^{-3}$ <sup>32</sup>. The electrical conductivity of an intrinsic semiconductor, such as Ge or Si, lies around  $10^2$ - $10^2$  S/cm<sup>32</sup>. The carrier concentration in a semiconductor dominates the conductivity, but also the carrier mobility  $\mu$ , where also the temperature dependence of  $\mu$  ( $\mu$  decrease with increasing temperature) has to be taken into account. Thus, the two primary ways to achieve high  $\sigma$  in a semiconductor are either by decreasing the band gap ( $E_G \ll 10 k_b T$ )<sup>4</sup> or by electronic doping, in order to increase the carrier density  $n$ .

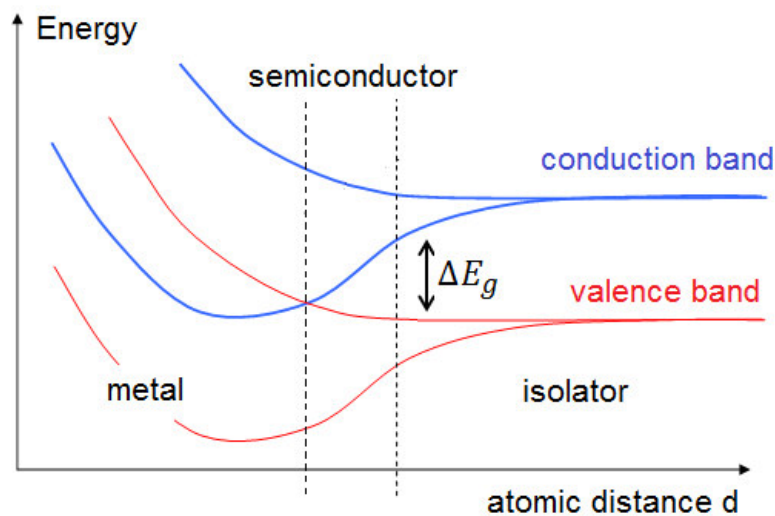


Figure 8 Schematic of the band structure of metals, semiconductor and insulator depending on the atomic distance  $d$ <sup>33</sup>.

The other key attribute in the TE performance  $zT$  is the Seebeck coefficient  $\alpha$ , which can be thought of as the heat per carrier over temperature<sup>4</sup>. In the case of a classical gas, each particle has an energy of  $E = \frac{2}{3}k_bT$ , where  $k_b$  is the Boltzmann constant. The thermopower of a classical electron gas is then approximately  $k_b/e \approx 87 \mu\text{V/K}$ , where  $e$  is the absolute value of the charge of the electron. For metals the Drude model<sup>31</sup> is well suited to describe the transport properties, and the thermopower can be defined as<sup>4</sup>:

$$\alpha \approx \left(\frac{k_b}{e}\right) \frac{k_bT}{E_F}, \quad (6)$$

where  $E_F$  is the Fermi energy (related to the chemical potential  $\Delta\mu$  of the material). Hereby, only the fraction  $k_bT/E_F$ , shown in Equation 6, participates in the conduction process and thus contributes to the thermopower  $\alpha$  of a material. At  $T \approx 0$  K, all states above the Fermi level  $E_F$  are vacant, and all the states below the  $E_F$  are occupied. So, the quantity  $k_b/e \approx 87 \mu\text{V/K}$  is constant and corresponds to the value of  $\alpha$ . However, ME exhibit much lower thermopower values, usually on the order of 1-10  $\mu\text{V/K}$ , due to the electronic and temperature dependence of  $\alpha$  ( $E_F \gg k_bT$ )<sup>4</sup>. The situation for a semiconductor is different, since charge carriers must be excited across the band gap  $\Delta E_g$  to make a contribution to the electronic transport. Thus the thermopower is approximately given by:

$$\alpha \approx \left(\frac{k_b}{e}\right) \frac{E_g}{k_bT} \quad (7)$$

According to Equation 7, the thermopower in semiconductors is much higher than the characteristic value  $k_b/e \approx 87 \mu\text{V/K}$  and increases with decreasing temperatures<sup>4</sup>. Furthermore, semiconductors can exhibit either electron conduction ( $n$ -type conduction with a negative sign of  $\alpha$ ) or hole conduction ( $p$ -type conduction with a positive sign of  $\alpha$ ). In the case of a bipolar contribution to the Seebeck coefficient,  $\alpha$  is the sum of the contributions arising from  $n$ - and  $p$ -type conduction described in Equation 8:

$$\alpha = \frac{\alpha_n\sigma_n + \alpha_p\sigma_p}{\sigma_n + \sigma_p} \quad (8)$$

It is favorable to dope the semiconductor with either donor or acceptor states to allow extrinsic conduction of one type of carriers, otherwise bipolar contributions will cancel out the Seebeck voltage and cause a reduction in the thermopower  $\alpha$ .



The electronic structure of a solid can be discussed in terms of its band structure or the density of states (DOS). Using the Boltzmann transport theory, the Seebeck coefficient  $\alpha$  can be expressed through the Mott equation<sup>9,34</sup>:

$$\alpha = \frac{\pi^2 k_b^2}{3e} T \left\{ \frac{d[\ln(\sigma(E))]}{dE} \right\}_{E=E_F}, \quad (9)$$

with the elementary charge  $e$  and  $\sigma(E)$  the energy-dependent electrical conductivity. The Mott equation describes the variation of the electrical conductivity  $\sigma(E)$  with the energy at the Fermi level  $E_F$ , whereas  $\frac{d[\ln(\sigma(E))]}{dE}$  is the slope of the DOS. The electrical resistivity  $\rho$  is the reciprocal term of the electrical conductivity  $\sigma$ , which is a function of the carrier concentration  $n$  and the mobility  $\mu$  of the charge carriers shown in Equation 10:

$$\frac{1}{\rho} = \sigma = ne\mu \quad (10)$$

Applying the energy dependence of Equation 10 to the Mott Equation 9 gives:

$$\alpha = \frac{\pi^2 k_b^2}{3e} T \left\{ \frac{1}{n} \frac{dn(E)}{dE} + \frac{1}{\mu} \frac{d\mu(E)}{dE} \right\}_{E=E_F} \quad (11)$$

The carrier concentration provides a conflict regarding the optimization of the  $zT$ , since the Seebeck coefficient  $\alpha$  and the electrical conductivity  $\sigma$  depends in opposite ways on the number of charge carriers (Equation 11). Therefore a compromise in the carrier concentration must be found to maintain a high  $\alpha$  without degrading  $\sigma$ <sup>20,35,36</sup>. Dependent on the material this can usually be realized for carrier concentration  $n$  between  $10^{19}$  and  $10^{21}$  carriers per  $\text{cm}^{-3}$ <sup>20</sup>. For a degenerate system (high carrier concentration) the Seebeck coefficient  $\alpha$  is given by<sup>37</sup>

$$\alpha = \frac{8\pi^2 k_b^2}{3eh^2} m^* T \left( \frac{\pi}{3n} \right)^{2/3}, \quad (12)$$

where at lower carrier density (non-degenerate semiconductors)  $\alpha$  is proportional to  $\ln(1/n)$ <sup>9</sup>. Another important factor influencing  $\alpha$  is the effective mass  $m^*$  of the charge carriers. The conflicting situation here is, that large effective masses produces high thermopower  $\alpha$  but cause low electrical conductivity  $\sigma$ . The  $m^*$  in Equation 12 refers to the DOS effective mass  $m_d^*$ <sup>20,38</sup>, which increases with flat, narrow bands (small curvature of the band) that have a high DOS at the Fermi level. Since the inertial effective mass is also related to  $m^*$ , heavy carriers will move with slower velocities and therefore smaller mobilities  $\mu$ , which in turn leads to lower electrical conductivities  $\sigma$ <sup>20</sup>. Hence here it is also required to find a balance between the

effective mass  $m^*$  of the dominant charge carriers and high mobility. High  $m^*$  and low  $\mu$  is typically found in ionic compounds where the electronegativity (EN) difference of the elements is large. Unlike the carrier density, it is not obviously, which effective mass is the optimum. Good TE materials can be found within a range of effective masses and mobilities<sup>20</sup>.

The power factor ( $PF$ ) is typically used to describe the resulting electronic power at a given temperature difference in TE materials and does not include the contribution of the thermal conductivity. Thus, the  $PF$  is given by the product of the thermopower  $\alpha$  and the electrical conductivity  $\sigma$ :

$$PF = \alpha^2 \sigma \quad (13)$$

It is worth mentioning that the Power factor, shown in Equation 13 peaks at higher carrier concentrations than  $zT$ , whereas the difference between the maxima of  $\alpha^2 \sigma$  and  $zT$  is greater for materials with lower lattice thermal conductivities<sup>20</sup>. As mentioned before, a precise adjustment of all the TE parameters and their dependencies must be found to achieve high  $zT$  values. Section 2.3 will present some approaches in order to enhance the electronic properties in a TE material.

## 2.2 Thermal conductivity

The discovery of complex, bulk TE materials with low thermal conductivity, e.g.  $\text{Yb}_{14}\text{MnSb}_{11}$  and  $\text{Ba}_8\text{Ga}_{16}\text{Ge}_{30}$ , has led to a renewed investigation of the fundamental mechanisms of thermal conductivity<sup>23,39</sup>. As known from solid-state physics, the thermal conductivity  $\kappa$  is the sum of electronic ( $\kappa_e$ ) and lattice ( $\kappa_{la}$ ) contributions<sup>31,39</sup>.

$$\kappa = \kappa_e + \kappa_{la} \quad (14)$$

Equation 14 shows another conflicting situation concerning the optimization of the TE performance, since the heat flow is conducted by electrons, holes and lattice vibrations (so called phonons) through the material. The electronic thermal conductivity  $\kappa_e$  is strongly related to the electrical conductivity  $\sigma$  through the Wiedemann-Franz law<sup>20</sup> (see Equation 15), and thus a radical reduction of the thermal conductivity  $\kappa$  will also affect the electrical conductivity  $\sigma$ .

$$\kappa_e = L\sigma T = ne\mu LT, \quad (15)$$

where  $L$  is the Lorentz number,  $2.4 \times 10^{-8} \text{ J}^2/\text{K}^2\text{C}^2$  for free electrons and  $\mu$  the carriers mobility. The Lorentz number is not constant and depends on the temperature and carrier concentration. Therefore an accurate determination of  $\kappa_e$  for each TE material is important, as the lattice thermal conductivity  $\kappa_{la}$  is often calculated from the difference between  $\kappa$  and  $\kappa_e$ <sup>20</sup>. For complex half-Heusler compounds the Lorentz number<sup>40</sup> has been derived from the one-electron model to be  $L = 1.6 \times 10^{-8} \text{ J}^2/\text{K}^2\text{C}^2$ . Furthermore, adverse effects, e.g. bipolar conduction has to be taken into account in order to achieve low thermal conductivities  $\kappa$ . Thereby the band gap size plays a decisive role. The smaller the band gap  $\Delta E_g$ , the more carriers can easily be excited across the energy gap, contributing to  $\sigma$  and  $\kappa_e$ . The influence of bipolar conduction usually can be seen in an upturn in  $\kappa$  at higher temperatures, which will decrease the figure of merit and therefore the TE performance in this temperature range.

The main component of heat flow is carried by phonons through the lattice. These quasi particles occur at various wavelengths and depending on their frequency a distinction can be made between acoustic phonons and optical phonons (Figure 9). In general, lattice vibrations moving in phase are associated with low-frequency acoustic phonons, whereas the high frequency optical phonons represent anharmonic oscillations between two neighboring atoms<sup>31</sup>.

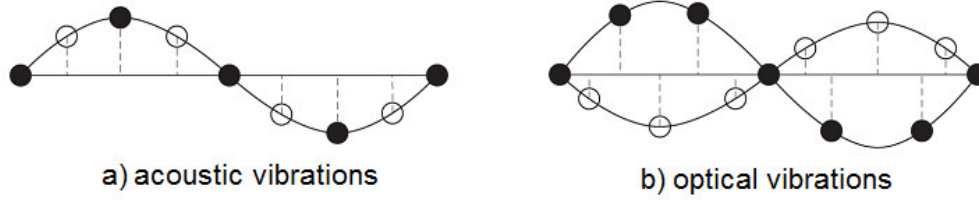


**Figure 9** Illustration of the transversal vibration of a) the optical phonons, where the atoms (filled and unfilled circle) oscillate in phase and b) the acoustic phonons with anharmonic oscillation of the atoms<sup>31</sup>.

The lattice thermal conductivity  $\kappa_{la}$  can be described as the product of heat capacity  $c_p$ , phonon group velocity  $v_g$  and phonon mean free path  $l$  Equation (16). The phonon relaxation time  $\tau$ , is defined as the time between two collisions and is related to  $l$  through the phonon velocity  $v_g = l/\tau$ <sup>39</sup>. Due to symmetry, only one third of the energy is carried along a specified direction, thus the lattice thermal conductivity  $\kappa_{la}$  can be written as:

$$\kappa_{la} = \frac{1}{3} c_p v_g l = \frac{1}{3} c_p v_g^2 \tau \quad (16)$$

The acoustic phonons are the main heat conductors and can be treated with the Debye model. Low thermal conductivity can be achieved in materials with a low Debye temperature,  $\Theta_D$ , and low heat capacity,  $c_p$ . These conditions are best satisfied in alloys with heavy elements such as Pb, Bi, or Te. According to the specific heat, at low temperature, the thermal conductivity increases proportional to  $T^3$ <sup>31</sup>. With increasing temperature more and more phonons are excited and take part in carrying heat, and progressive phonon-phonon interactions occur. The interactions between phonons are known as Normal ( $N$ ) or Umklapp ( $U$ ) processes, whereby the  $U$  process has a greater impact on the thermal conductivity<sup>32</sup>. However, the specific heat of most solids at room temperature and above is nearly constant, in agreement with the Law of Dulong and Petit, i.e. for temperatures  $T \gg \Theta_D$  all vibrational states are sufficiently occupied and  $c_p$  reaches the value of  $3R$ , where  $R$  is the ideal gas constant<sup>31</sup>.

The theoretical relation between the phonon dispersion, atom mass and bond strength between two atoms is not discussed in this work, but it should be mentioned that low bond strength (ionic binding) between the atoms and high atomic masses (heavy elements) diminish the phonon velocities and cause low  $\kappa_{la}$ <sup>32,39</sup>. Thus, traditionally low thermal conductivity  $\kappa$  can be realized in dense materials with soft bonds (small group velocity  $v_g$ ) or in nanostructured and strongly disordered compounds, where the lattice vibrations can be impeded via phonon scattering (short mean free path  $l$ )<sup>39</sup>. Different phonon scattering mechanism can also be

distinguished: phonon-phonon, phonon-defects and phonon-interfaces<sup>41</sup>. Applying Matthiessen's rule<sup>42</sup>:

$$\tau^{-1} = \tau_N^{-1} + \tau_U^{-1} + \tau_{PD}^{-1} + \tau_B^{-1} + \tau_{EP}^{-1}, \quad (17)$$

with the different scattering relaxation times (Equation 17) for normal phonon-scattering ( $N$ ), Umklapp scattering ( $U$ ), point defect scattering ( $PD$ ), boundary scattering ( $B$ ), and electron-phonon interactions ( $EP$ ), respectively. Normal and Umklapp scattering are phonon-phonon interactions, while the  $N$ -process conserves the total phonon momentum, and the  $U$ -process changes phonon momentum. The  $U$ -process is often the dominate mechanism at temperatures above  $\Theta_D$  and generate a noticeable reduction of the thermal conductivity<sup>39</sup>. Point defect scattering arises from mass differences (mass field fluctuations) and strain contrast (strain field fluctuations) within the lattice and can be realized by site substitution (alloying). Multi-component materials or nanostructured compounds exhibit a crucial reduction of  $\kappa_{la}$  due to phonon scattering at boundaries or interfaces. Since phonons vary widely in their wave-length and mean free paths (from less than 1 nm to greater than 10  $\mu\text{m}$ )<sup>20</sup>, there are mechanisms which contribute to stronger phonon scattering at a particular frequency<sup>39</sup>. Thus, Umklapp and point defect scattering target high frequency phonons, while boundary scattering is often the dominant scattering mechanism at low frequencies, which carry the largest portion of heat<sup>38,43</sup>. For  $T > \Theta_D$  the reverse relaxation time  $\tau^{-1}$  for phonon-phonon scattering should be proportional to the temperature  $T$ .

## 2.3 Optimization of figure of merit $zT$

The required criteria for a high-performance TE material is sufficiently unified in the phonon glass electron crystal (PGEC) concept, introduced by *Slack*<sup>19</sup>. In order to improve the figure of merit,  $zT$  high Seebeck coefficient  $\alpha$ , high electrical conductivity  $\sigma$  and low thermal conductivity  $\kappa$  are desired. However, these materials properties are strongly coupled, and the favorable combination and can only be optimized by making compromises (Figure 10). The general strategy towards high TE efficiency can be attained by optimizing the electronic properties due to the optimization of the carrier concentration<sup>44</sup> and by decreasing the thermal conductivity due to an effective phonon scattering at defects and interfaces<sup>20,35,36</sup>.

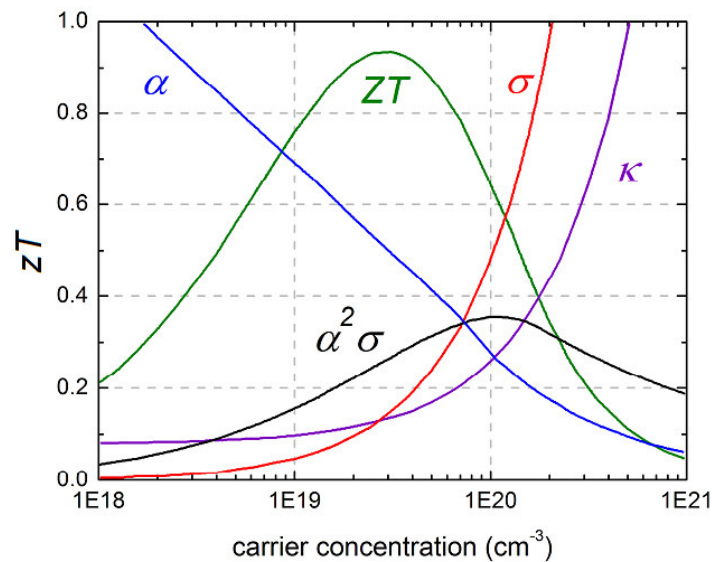


**Figure 10** Influence of charge carrier concentration on the Seebeck coefficient  $\alpha$ , the electrical conductivity  $\sigma$ , the thermal conductivity  $\kappa$  and the Power factor  $\alpha^2 \sigma$ <sup>20</sup>.

### 2.3.1 Enhancement of the electronic properties

Since the studies by *Dresselhaus* in the early nineties<sup>21,22</sup>, different approaches have guided the experimental efforts towards superlattices and nanostructures in the area of TE materials. Quantum well (0-D, 1-D, and 2-D) systems take advantage of a low-dimensional character through physical confinements in quantum dots, nanowires, and thin-film structures to enhance the electronic properties<sup>22</sup>. The improvement in  $zT$  is attributed to creating a nanoengineered material that is efficient in thermal insulation while remaining a good electrical conductor. As mentioned before, a high Seebeck coefficient  $\alpha$  is desired, while an

optimum carrier density for the highest thermopower might be too low to obtain high electrical conductivity.

As discussed in section 2.1 the electronic properties strongly depend on the carrier concentration. At higher temperatures many minority carriers can be excited in compounds with small band gaps, leading to adverse effects such as bipolar conduction of mixed carriers, which will cancel out the Seebeck voltage and thus reduce the thermopower. Therefore, it may be beneficial to increase the band gap  $\Delta E_g$  of a material by varying the chemical composition to suppress bipolar contributions. For instance, the band gap of the HH compound TiCoSb is about  $\Delta E_g = 1.06 \text{ eV}$ <sup>45</sup>, which is twice as high as in ZrNiSn ( $\Delta E_g = 0.5 \text{ eV}$ ). TiCoSb exhibits no bipolar conduction for temperatures up to 900 K, whereas ZrNiSn-based HH materials reveal a decrease in the thermopower already at 600 K. Therefore the main research on *p*-type HH compounds is focused on TiCoSb based materials, where bipolar contributions are suppressed and the TE performance is decisively improved.

The thermopower  $\alpha$  not only depends on the carrier density, but is also dominated by the electronic band structure of the material. At a given carrier concentration the Seebeck coefficient is large for a high DOS, which in turn means a high density states effective mass  $m_d^*$ . Therefore, one approach to increase the electron properties is by engineering distortions of the electronic density of states DOS at the Fermi surface<sup>46</sup>. This can be realized either by a large number of conduction bands  $N_v$ , which is also called band degeneracy<sup>47</sup>, or via flat bands giving a high  $m_b^*$ <sup>38</sup>

$$m_d^* = N_v^{2/3} m_b^* \quad (18)$$

However, high  $m_b^*$  (small curvature) is also associated with low carrier mobility  $\mu$  and leads to low electrical conductivity  $\sigma$  (see Equation 10)<sup>38</sup>. One approach to increase the thermopower, proposed by *Heremans et al* is by introduction of so-called resonant states into the material via doping<sup>34,46</sup>. More recently, a systematic study of gap size and thermoelectric properties has suggested a model for the location of dopant-induced features within the band gap region in the case of 3*d* transition metal substitution in HH compounds. *Simonson et al*<sup>48</sup> have reported the introduction of resonant states near the Fermi level with marginal amounts of V doping in  $\text{Hf}_{0.75}\text{Zr}_{0.25}\text{NiSn}$ , leading to a substantial increase in the electronic properties. Figure 11 illustrates the influence of resonant states and multiple bands on the DOS at the Fermi surface. The sharp resonant state located at the valence band edge can be considered as an electron reservoir, which is responsible for many thermally excited carriers occupying

states far above  $E_F$ , leading to a huge change in the chemical potential  $\delta\mu$  in the TE material<sup>46</sup>. This in turn causes a high Seebeck voltage or respectively a larger thermopower. In HH compounds a high DOS is already available due to the  $d$ -states of the transition metals near the Fermi surface.

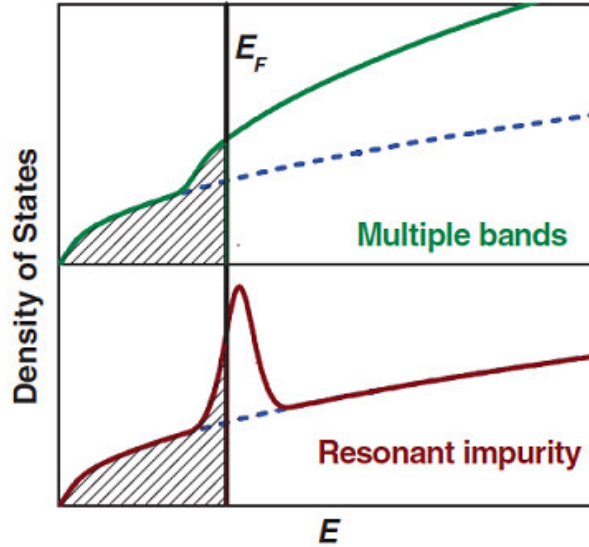


**Figure 11 Schematic of the influence of multiple bands and resonant states on the density of states (DOS)<sup>37</sup>.**

Another approach to achieve large thermopower and sufficient electrical conductivity is to increase the band degeneracy, in other words, increase the number of degenerate conducting bands  $N_v$  contributing to electronic transport at the valence band edge<sup>49</sup>. Band degeneracy increases either when multiple bands have comparable energy (within few  $k_bT$ ), i.e. a degenerated band extrema, or when multiple carrier pockets in the Brillouin zone are degenerate, because they are symmetrically equivalent due to the symmetry of the crystal<sup>38,49</sup>. Since it is not possible to vary the  $N_v$  in a compound without changing the crystal structure, it is possible to converge several bands to obtain larger  $N_v$ . Figure 12 shows the Brillouin zone of PbTe, where the light valence band at the  $L$ -point has a fourfold symmetry ( $N_v = 4$ ) with a direct band gap to the conduction band. The heavier valence band at the  $\Sigma$ -point with a 12-fold symmetry ( $N_v = 12$ ) is located at lower energies. With increasing temperature the light valence band lowers its energy and converges ( $N_v \sim 12-16$ ) at 500 K with the heavier valence band, leading to an increase in the DOS and thus to an increase in the Seebeck coefficient at higher temperatures<sup>38</sup>.



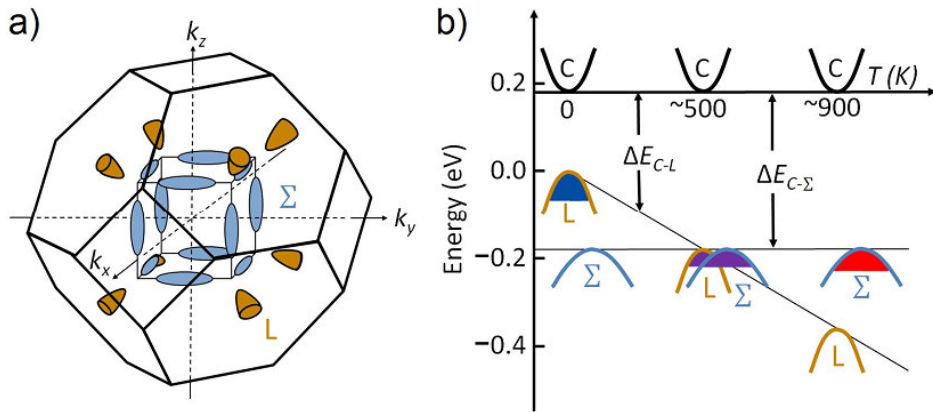


Figure 12 a) Brillouin zone of PbTe showing a low band degeneracy of  $N_v$  equals 4 for the  $L$ -point (orange) and 12 for the  $\Sigma$ -point (blue), b) Temperature dependence of the two valence bands<sup>37</sup>.

### 2.3.2 Reduction of the thermal conductivity

Most work in the improvement of TE materials have been driven by the reduction in the thermal conductivity  $\kappa$ . Since the electronic thermal conductivity  $\kappa_e$  is related to the electrical conductivity  $\sigma$ , the general approach to lower  $\kappa$  while not affecting  $\sigma$ , has been to reduce the lattice thermal conductivity  $\kappa_{la}$  via an effective phonon scattering in the material. Figure 13 illustrates the ideal material properties in a TE compound from the electron's and phonon's perspective. According the PGEC concept phonons should be disrupted like in a glass but the electrons should have high mobility like they do in crystalline semiconductors<sup>4</sup>. In other words a good TE material requires unusual materials properties.

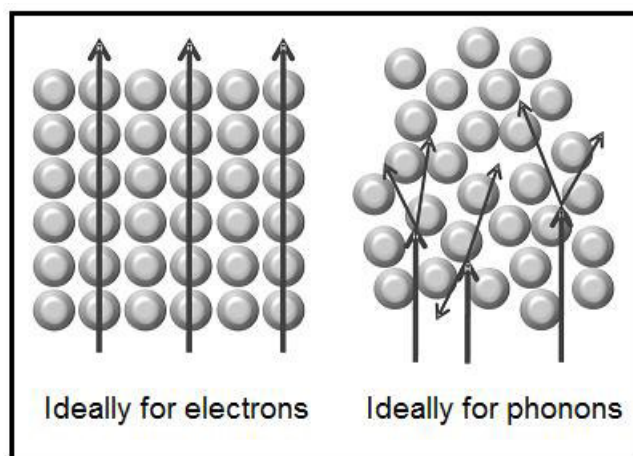


Figure 13 Ideal property for a good TE material from the electrons perspective (right) and the phonon perspective (left)<sup>19</sup>.

*Cahill et al* (50) proposed a minimum scattering length for phonons as a function of the phonon frequency leading to a model of the glassy limit of the lattice thermal conductivity. Slack taught us that the optimization of  $zT$  is limited by the minimum thermal conductivity  $\kappa_{min}$  ( $\approx 0.25 - 0.5$  W/mK)<sup>4,19</sup> as the mean free path is limited essentially by the interatomic distances between the atoms within the crystal. The most recent achievements in the TE community lead to the development of materials that are progressively closer to the PGEC behavior. Whereby, there are three general strategies to reduce the lattice thermal conductivity.

The first is to scatter phonons within the unit cell by creating rattling structures or point defects via site substitution (alloying)<sup>20,36</sup>. The potential to reduce  $\kappa$  through disorder and point defects within the unit cell is large in structures with void positions and has been successfully shown in Clathrates<sup>18</sup>, Skutterudites<sup>23</sup> or half-Heusler compounds<sup>51</sup>. In particular, the alloying approach with isoelectronic elements in HH materials preserves the crystalline electronic structure while the resulting mass and strain field fluctuations disrupt the phonon mean free path and decreases  $\kappa_{la}$ . The second approach is to use complex crystal structures to separate the electron-crystal from the phonon glass. Here the complexity of Zintl compounds is an appropriate example of how to achieve nearly PGEC-like behavior<sup>37</sup>. The combination of covalent and ionic bonding types, e.g.  $\text{Sr}_3\text{Ga}_{0.93}\text{Zn}_{0.07}\text{Sb}_3$ , leads to a complex structure and with  $\kappa_{la} \sim 0.4$  W/mK at 1000 K, resulting in a figure of merit of  $zT = 0.9$  at 1000 K. The third strategy is to scatter phonons at interfaces, for example in nanostructured materials or multiphase compounds<sup>52</sup>. Furthermore, these nanostructures can be formed as thin-film superlattices or intimately mixed composite structures. In the latter case, spark plasma sintering (SPS) is a useful tool to maintain grain boundaries at the nanoscale<sup>53</sup>. The frequency dependence of the phonons creates a need for phonon scattering agents at a variety of length scales. Phonon scattering at interstitials, vacancies or impurities is an effective way to impede high frequency phonons<sup>41</sup>, while low- and mid-frequency phonons are effectively scattered at interfaces and nanostructures<sup>52</sup>.

## 3 Half-Heusler materials

### 3.1 Introduction

Heusler alloys are a versatile class of intermetallic compounds, involving more than 1500 compounds, named after the German chemist *Friedrich Heusler*. The physical features of Heusler materials can easily be predicted by the valence electron count (VEC). This relationship was introduced by *Jeitschko* in 1970<sup>54</sup>. For instance, Heusler compounds with 8 or 18 VEC are semiconducting and extraordinarily stable, due to the closed shell configuration<sup>51</sup>. Their extraordinary potential and multifunctional properties e.g. magneto-caloric, magneto-electronic and semiconducting, promote the development of novel Heusler materials for energy technologies<sup>51</sup>. Today, the research of Heusler materials emerges for various applications such as TE<sup>36</sup>, spintronic<sup>55</sup> and topological insulators<sup>56</sup>. A distinction is made between half-Heusler (HH) alloys  $XYZ$  with a 1:1:1 composition and full-Heusler (FH) alloys  $X_2YZ$  with a 2:1:1 composition. Since this work aims the investigation of HH materials for TE applications, the following discussion will be focused on the characteristics of HH materials. However, a precise overview of Heusler compounds and their properties is given by *Graf et al* in<sup>51</sup>.

HH compounds with the general formula  $XYZ$  crystallize in a non-centrosymmetric cubic  $C1_b$  structure ( $F\bar{4}3m$ , spacegroup 216), which can be derived from the tetrahedral zinc blend-type structure by filling the octahedral lattice sites, shown in Figure 14. The HH structure consists of three interpenetrating fcc sublattices occupied by the elements  $X$ ,  $Y$  and  $Z$ , respectively. The corresponding Wyckoff positions are  $4a$  (0, 0, 0),  $4b$  (1/2, 1/2, 1/2) and  $4c$  (1/4, 1/4, 1/4)<sup>57</sup>. All three elements  $X$ ,  $Y$  and  $Z$  can occupy each atomic position and thus allow three different atomic arrangements within this cubic structure. The tetrahedral  $4d$  (3/4, 3/4, 3/4) position is vacant for HH compounds. The combination of main group and transition elements for  $XYZ$  with 8 or 18 VEC provides a huge diversity for possible composition and a good starting point for material engineering.

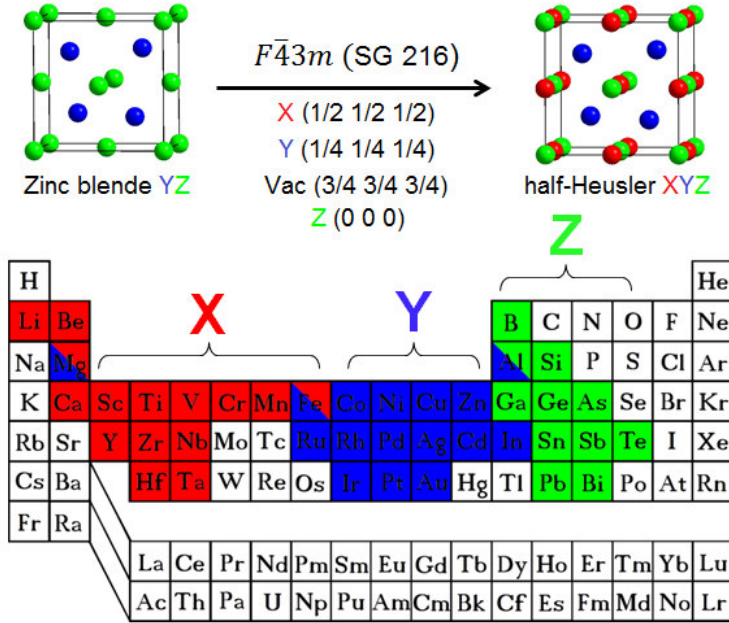


**Figure 14** Periodic table of elements including the crystal structure  $F\bar{4}3m$  of zinc blende and HH compound. The various number of HH compounds can be formed by combination of the different elements according the color scheme.

The chemical bonding in HH compounds is complicated. *Kandpal et al* have shown with electron localization isosurfaces (ELF)<sup>58</sup> in LiAlSi strong covalent bonding between Al and Si atoms, while Li behaves effectively like ionic  $\text{Li}^+$ . The bonding in HH compounds with 8 VEC can simply be described by a molecular orbital approach as  $[X]^{n+}[YZ]^{n-}$ . In the case of HH compounds with 18 VEC the chemical bonding is more sophisticated but can also be considered in good agreement with the Zintl concept<sup>51,58</sup>. In general, the X element is the most electropositive one, and the strength of the interaction between the covalent and ionic part is proportional to the difference in the electronegativity (EN) of the elements<sup>51</sup>.

The size of the band gap  $\Delta E_g$  in HH compounds is given by the interaction of the elements in the crystal structure and can be tuned from zero to 4 eV<sup>51</sup>. The band gap in HH with 18 VEC can be adjusted from zero to  $\sim 1.1$  eV<sup>36</sup> by altering the chemical composition, whereas a larger difference in the EN between the *d* elements leads to larger band gaps<sup>59</sup>. Hence, the calculated energy gap of TiNiSn (0.45 eV)<sup>60,61</sup> is smaller than ZrNiSn (0.50 eV)<sup>59</sup>, due to the larger difference in EN of Zr (1.3) compared to Ti (1.54). However, the experimental data of the band gap in HH compounds usually reveals much lower values, e.g. for TiNiSn (0.12 eV) and ZrNiSn (0.19 eV)<sup>59,62</sup>. This discrepancy between experimental and calculated values is due to anti-site defects within the HH structure. Figure 15 exemplifies the influence of  $\text{Ni} \leftrightarrow \text{Vac}$  anti-site disorder in ZrNiSn. The ordered structure reveals an indirect band gap with a single parabolic conduction band and a triply degenerated valence band at the  $\Gamma$  point

(Figure 15 a)<sup>63</sup>. With 1% Ni $\leftrightarrow$ Vac anti-site disorder, the Fermi energy is shifted to the bottom of the conduction band and impurity-induced states emerge at the top of the valence band (Figure 15 b), leading to a decrease of the band gap  $\Delta E_g$ . With increasing anti-site disorder a distinct broadening of the electronic states in the valence band can be observed (Figure 15 c), which has an adverse effect on the carrier mobility in the compound<sup>64</sup>. The reduction of  $\Delta E_g$  in ZrNiSn due to disorder defects can be diminished to zero eV with about 15% anti-site disorder<sup>65,66</sup>, which will considerably affect the transport properties in the material. Since Ni $\leftrightarrow$ Vac anti-site disorder exists in all HH materials, the compounds reveal intrinsic *n*-type conductivity.

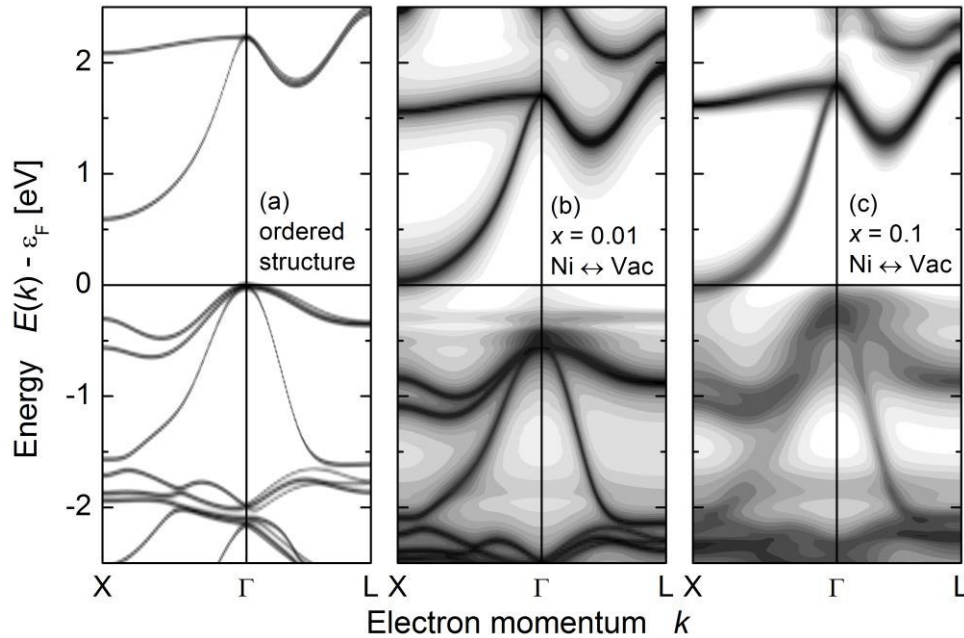


**Figure 15** Electronic structure of ZrNiSn from *ab initio* calculations performed by Dr. G.H. Fecher at Max-Planck-Institute for Chemical Physics of Solids (Dresden) depending on Ni $\leftrightarrow$ Vac anti-site disorder. a) Ordered C1<sub>b</sub> structure. b) with 1% Ni $\leftrightarrow$ Vac anti-site disorder and c) with 10% Ni $\leftrightarrow$ Vac anti-site disorder.

### 3.2 Half-Heusler materials for TE application

Intermetallic HH compounds with 18 VEC, such as  $MNiSn$  and  $MCoSb$  have attracted tremendous attention as suitable materials for TE power generation owing to their favorable electronic properties, such as semiconducting behavior and very flexible electronic structures<sup>36,51</sup>. According to the resulting structural disorder most of the HH materials are narrow band gap semiconductors, with a band gap  $\Delta E_g$  from 0.1 to 0.23 eV, which provides the appropriate number of charge carriers. In 1994, *Sofa* and *Mahan* established a model for TE semiconductors saying that the application temperature of a TE material is about six times lower than its energy gap<sup>67</sup>. Thus, due to their intermediate  $\Delta E_g$ , HH compounds are suitable materials for TE applications at moderate temperatures<sup>36</sup>.

The calculated band structure of  $TiNiSn$  is pictured in Figure 18, showing the indirect band gap of  $\Delta E_g = 0.45$  eV. The electronic structure exhibits the  $sp$  hybridization gap at 5-8 eV below the Fermi energy, which separates the deep lying bonding states resulting from the covalent interaction between Ni and Sn. The sharp density of states (DOS) at about - 2 eV arises mainly from bonding Ni  $d$ -states. The DOS near the Fermi level  $E_F$  emerges from the Ti  $d$ -states and is most important for the transport properties<sup>63</sup>.

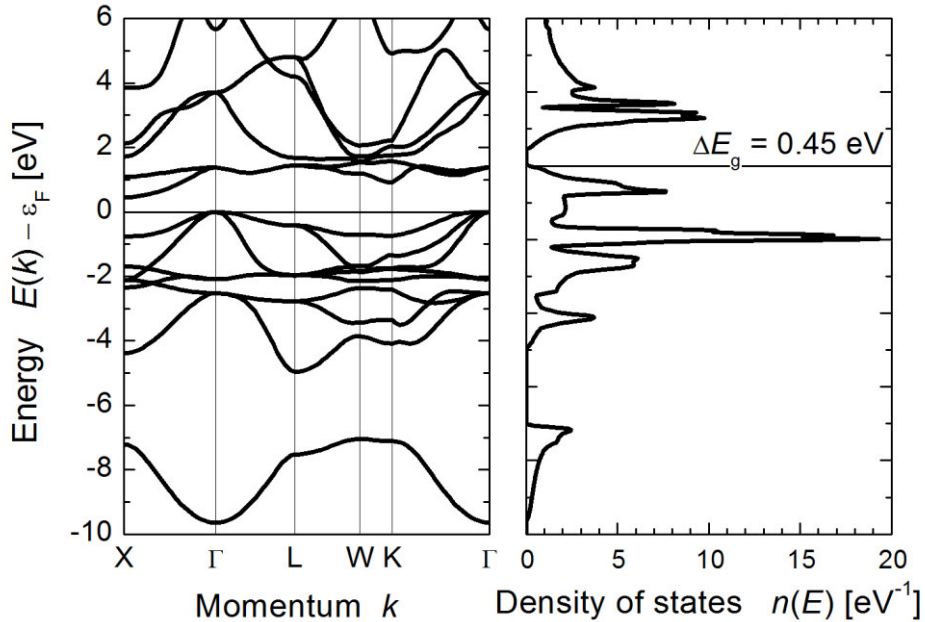
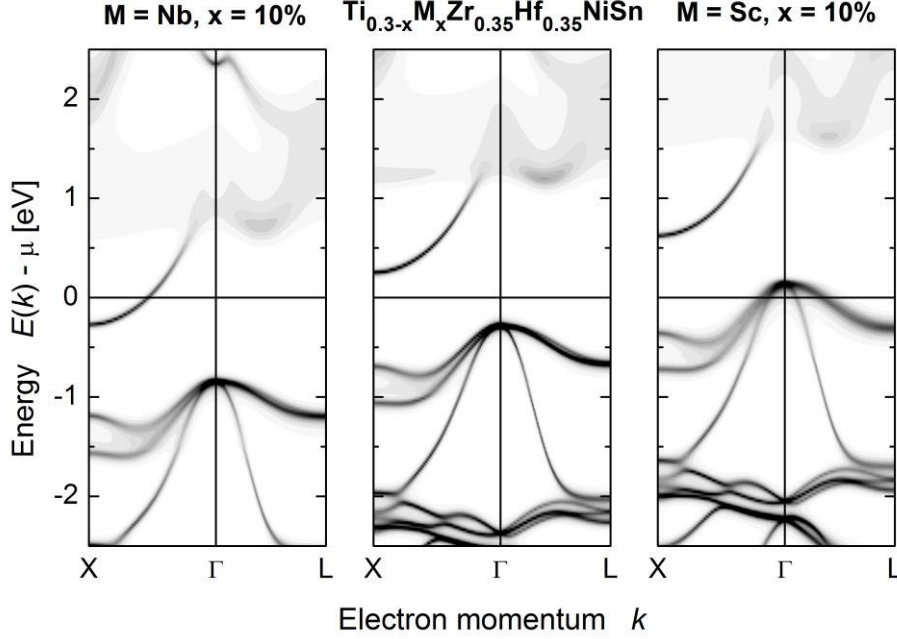


Figure 16 Electronic structure and density of states (DOS) of  $TiNiSn$ <sup>63</sup>.

The great advantage of the HH structure is the possibility to dope each of the three occupied fcc sublattices individually via site substitution (alloying). Hence a huge variety of HH materials can be produced based on one starting compound<sup>36</sup>. Site substitution with isoelectric elements is mainly used to reduce the thermal conductivity due to an enhanced disorder scattering of phonons<sup>68,69</sup>. Whereby, site substitution with non-isoelectronic elements, i.e. electronic doping, significantly affects the transport properties in HH materials. Elements with donor dopant properties (elements with more valence electrons) introduce additional electrons into the HH system, leading to a shift of the Fermi energy towards the conduction band (i.e. higher energies) and increasing of the band gap size. Therefore, minority carriers are suppressed and cause a shift of the Seebeck coefficient to higher temperatures. Acceptor dopants (elements with less valence electrons) introduce holes into the system, shift the Fermi energy towards the valence band (to lower energies) and cause a change of the electronic transport from *n*- to *p*-type conductivity.

Figure 17 illustrates the influence of site substitution in the *n*-type  $\text{Ti}_{0.3}\text{Zr}_{0.35}\text{Hf}_{0.35}\text{NiSn}$  compound with Nb as a donor dopant and Sc as an acceptor dopant. It can be seen, that electron doping changes the position of the Fermi energy with 10% Nb substitution into the conduction band, and with 10% Sc substitution into the valence band. *Tobola et al*<sup>70</sup> have shown that the impact on the transport properties via electronic doping in HH materials depends on the sublattice where the substitution takes place. Thus, adding one electron on the Z-site (e.g. Sn replaced by Sb) does not have the same effect as increasing the number of electrons at the X-site by replacing Ti by Nb, due to the different origin of the electrons and their localization in the DOS. It can be assumed, that a change in the number of electrons on the X site (Ti replaced by a non-isoelectronic TM) has the greatest influence on the electronic properties, since these elements are responsible for the appearance of the electronic states near the Fermi level<sup>48,63</sup>.



**Figure 17** Electronic structure of the  $n$ -type  $\text{Ti}_{0.30}\text{Zr}_{0.35}\text{Hf}_{0.35}\text{NiSn}$  from *ab initio* calculations performed by Dr. G.H. Fecher at Max-Planck-Institute for Chemical Physics of Solids (Dresden). The Fermi energy is shifted into the conduction band with 10% Nb substitution and into the valence band with 10% Sc substitution.

Electronic doping of small amounts of transition metals into the HH system introduces local features in the DOS near to or within the band gap region<sup>48</sup>. This addition of dopant-induced states near the Fermi energy contributes to a larger Seebeck coefficient  $\alpha$  at room temperature. The quantity of dopant for these sharp dopant states depends on the sublattice where the substitution takes places. For instance, minute amounts ( $< 1\%$ ) of Sb-doping on the Sn position leads to significantly improved TE performance<sup>44,69</sup>. However, higher dopant concentration causes a distinct broadening of these dopant-induced states, leading to a rapid degradation of the TE properties. The consequent increase of disorder and carrier scattering will significantly diminish the carrier mobility<sup>64,70</sup>. *Ouardi et al* have shown the impact of acceptor doping in the  $n$ -type  $\text{Ti}_{0.3}\text{Zr}_{0.35}\text{Hf}_{0.35}\text{NiSn}$  HH system. The substitution of 4% Sc on the Ti-position induced a change in transport properties from  $n$ - and  $p$ -type conduction<sup>71</sup>, where the Seebeck coefficient  $\alpha$  reveals a maximum for both  $n$ - and  $p$ -type compound at  $|\alpha| \sim 210 \mu\text{V/K}$  at 600 K. Figure 18 emphasizes the dopant-induced change in the chemical potential  $\delta\mu$ , leading to a peak in the Seebeck coefficient  $\alpha$  near the Fermi level  $E_F$ . Note that small doping levels are already sufficient to cause a considerable shift of the Fermi level and thus an improvement in the electronic properties.



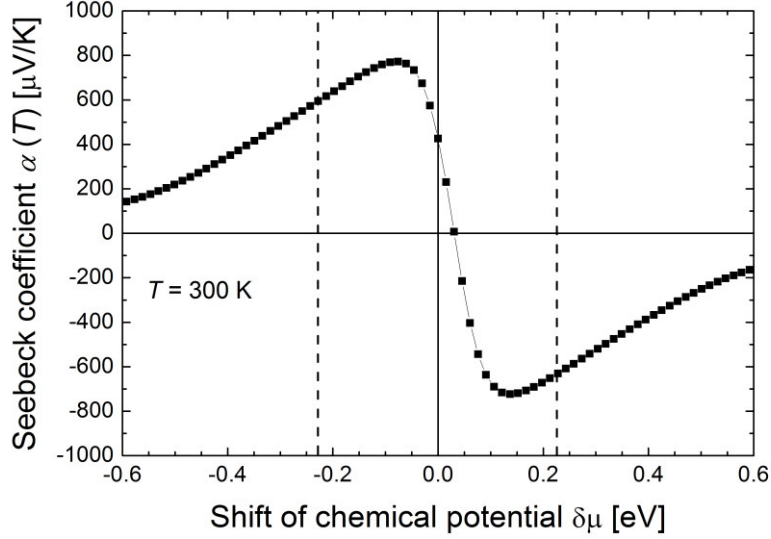


**Figure 18 Influence of electronic doping on the Seebeck coefficient  $\alpha$ . The dashed lines indicate the band extrema of the valence and conduction band<sup>63</sup>.**

In the past few years numerous *MNiSn* and *MCoSb*-based HH compounds have been investigated regarding their TE properties. Although ternary HH compounds exhibit excellent electronic characteristics, like Seebeck coefficients up to  $|\alpha| \sim 300 \mu\text{V/K}$  at room temperature<sup>36,51</sup> and high electrical conductivity ( $\sigma \sim 1000\text{-}10000 \text{ S/cm}$ )<sup>72,73,74</sup>, their TE applicability was limited by their high thermal conductivities  $\kappa > 7\text{-}17 \text{ W/Km}$ <sup>35,68</sup>. But owing to the development in the TE community, the thermal conductivity  $\kappa$  of HH materials could be decisively reduced by the introduction of nanostructures and nanoinclusions<sup>75,76,77</sup> or by site substitution (alloying)<sup>72,78</sup>. The substitution of non- and isoelectronic elements lead to a drastic decline in the thermal conductivity ( $\kappa < 4 \text{ W/Km}$ ) in HH materials<sup>32,69</sup>. The resulting higher disorder due to higher mass and strain fluctuations and an intrinsic phase separation in multi-component HH materials are responsible for the strong reduction in  $\kappa$ . The intrinsic phase separation is a key to high TE properties in HH compounds and will be discussed in the following 3.3 section.

In general, HH materials with 18 VEC are extraordinarily thermal resistant, due to their high melting points. The thermal analysis measurements of *TiNiSn*, *ZrNiSn* and *HfNiSn* exhibit endothermic reactions at 1453 K, 1708 K and 1760 K, which correspond to their melting points, respectively<sup>79</sup>. Hence, a high temperature synthesis is necessary to fabricate HH compounds. Usually HH materials are prepared by arc melting<sup>63,80</sup>, induction heating<sup>81</sup> or solid state reaction<sup>77</sup>. Mechanical alloying of HH compounds is not successful due to the limited energy input<sup>36</sup>. With increasing demand on new TE materials new preparation techniques were developed in recent years such as melt spinning<sup>82</sup> or spark plasma sintering

(SPS)<sup>83</sup>. Spark plasma sintering (SPS) was previously implemented as an effective densification technique and is frequently used to attain nanostructures in compounds. In this procedure a series of dc current pulses with a strength of 1500 A are applied to the powdered sample and the pressing tool, leading to high-rate heating, whereby the main amount of heat is generated in the sample between the powder particles<sup>53,84</sup>. There are a number of proposed mechanisms to account for the enhanced sintering behaviors, which are still under discussion.

In addition to their TE properties *MNiSn* (*n*-type) and *MCoSb* (*p*-type) based HH materials have attracted great interest because they contain low cost and environmentally friendly elements and are easy to synthesize<sup>71,77</sup>. Most recently *Bartholomé et al*<sup>81</sup> investigated the reproducible up-scaling process of *n*-type  $Zr_{0.4}Hf_{0.6}NiSn_{0.98}Sb_{0.02}$  and *p*-type  $Zr_{0.5}Hf_{0.5}CoSb_{0.8}Sn_{0.2}$  into kg batches. The TE module, build out of these HH compounds contained 7 *p*- and 7 *n*-type thermocouples, reaching a maximum power output of 2.8 W.

### 3.3 Phase separation in half-Heusler compounds

For a long time, the applicability of HH materials was limited by their high thermal conductivity  $\kappa$ . In particular, ternary HH materials such as  $M\text{NiSn}$  ( $M = \text{Ti}, \text{Zr}, \text{Hf}$ ) reveal typical  $\kappa$  values  $> 7\text{--}17 \text{ W/Km}$ <sup>35,68</sup>. Today, the research of HH-based TE materials is mainly focused on multi-component HH systems, owing to their lower thermal conductivities ( $\kappa < 4 \text{ W/Km}$ )<sup>36,69,73,80</sup>. A remarkable characteristic of multi-component HH compounds is their intrinsic phase separation when the compounds are solidified by rapid cooling, leading to a significant reduction of  $\kappa$ , and thus to improved TE efficiencies<sup>80,85</sup>. The lower  $\kappa$  values in multi-component HH systems basically occur due to different phonon scattering agents in the structure. The impedances of high-frequency phonons are induced by mass and strain fluctuation due to the site substitution at the  $X$ -site, while the intrinsic phase separation acts as a further  $\kappa$  limiter, and decisively impedes low and mid-frequency phonons effectively at the dendritic interfaces<sup>9</sup>.

It is clear that the intrinsic phase separation is the key to high TE efficiencies in HH materials<sup>85</sup>. The experimental efforts of site substitution in HH compounds significantly improved the TE performances of HH materials. Hereby,  $zT$  values of 1.5 in the  $n$ -type  $\text{Ti}_{0.5}\text{Zr}_{0.25}\text{Hf}_{0.25}\text{NiSn}_{0.998}\text{Sb}_{0.002}$  material<sup>68</sup>, and 1 in the  $p$ -type  $\text{Ti}_{0.12}\text{Zr}_{0.44}\text{Hf}_{0.44}\text{CoSn}_{0.8}\text{Sb}_{0.2}$  material<sup>73</sup> could be attained. This leads to the suggestion that temperature stable eutectic microstructures can establish an entirely new area in the TE community, where the phase-separation microstructure can be independently engineered to fulfill desired TE properties<sup>86</sup>. The typical phase separation that occurs in HH material, when prepared by arc melting is presented in Figure 19. In the following a short introduction will be given to understand the processes behind the formation of phase separation.

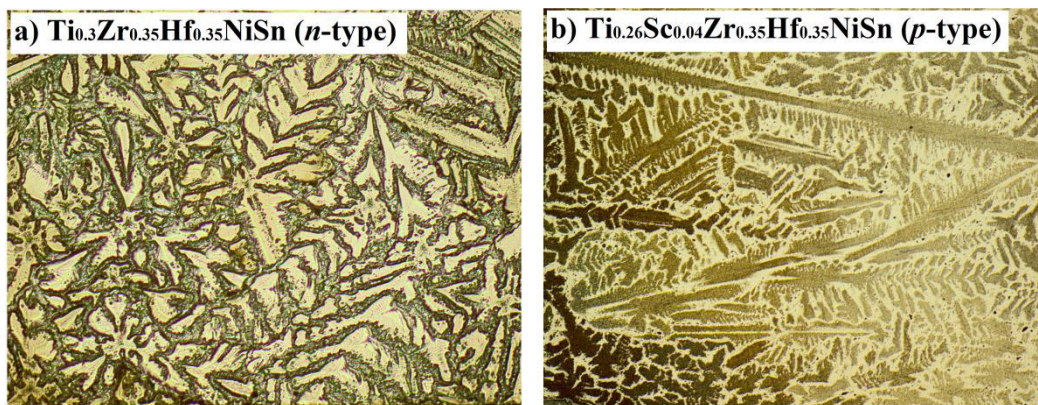


**Figure 19** Light microscope image of a) the  $n$ -type  $\text{Ti}_{0.3}\text{Zr}_{0.35}\text{Hf}_{0.35}\text{NiSn}$  and b)  $p$ -type  $\text{Ti}_{0.26}\text{Sc}_{0.04}\text{Zr}_{0.35}\text{Hf}_{0.35}\text{NiSn}$  HH compounds. The samples were etched with a  $\text{HCl}:\text{HNO}_3:\text{HF}:\text{H}_2\text{O}$  solution to highlight the intrinsic phase separation.

The properties of solid materials are strongly influenced by the solidification process. The solidification of a molten alloy mainly depends on the material properties of the alloy, the mould and on the cooling conditions<sup>87</sup>. Metallic materials can be solidified by electro- or electroless-deposition from salt solution, by vapor or sputter deposition, or by rapid cooling of their melts<sup>88</sup>. For high quality and large crystals the cooling rate has to be slow. According to Ostwald ripening<sup>89</sup>, the smaller crystals dissolve and redeposit onto larger crystals in order to minimize their surface energy. Higher cooling rates usually lead to a higher strain within the structure, due to constitutional changes in the composition and lattice defects, such as point defects and dislocations or the formation of non-equilibrium phases, which might be kinetically favored at the given conditions. Furthermore, a rapid cooling will shorten the diffusion distances and the reaction times<sup>88</sup>, resulting in the formation of a non-uniform distribution of impurity phases and segregates within the ingot. The practical experience of many centuries has led to the common knowledge that the microstructure and specific impurities in a material, e.g. carbon in steel are mainly responsible for the material properties such as stress relief cracking, temper brittleness or recrystallization<sup>90</sup>.

In pure metals, solidification is controlled by the rate at which the latent heat of solidification can be conducted away from the solid/liquid interface. The conduction of the heat can take place either through the solid or the liquid depending on the temperature gradients at the interfaces, which in turns affects the shape of the microstructure. In case of a fast heat dissipation (positive  $\Delta T$ ) in a solid, a uniform crystal growth can be observed with spherical grains due to a planar solidification front. The situation for slow heat dissipation (negative  $\Delta T$ ) is, however, different and can be found for a solid growing in supercooled melts. Here, the solidification front is unstable, resulting in the formation of so-called dendrites<sup>87,91</sup>. The originally spherical solid particles develop arms in many directions in order to remove heat into the melt. An appropriate annealing treatment usually causes a rearrangement of the phases in the microstructure, leading to the resolution of the dendrites in order to minimize the surface energy to attain a thermodynamic equilibrium<sup>87</sup>. However, if the separated phases are stable and do not reveal peritectic decomposition during the annealing treatment, the phase fraction remains constant<sup>90,91</sup>. This means the element composition and lattice parameter are maintained under the annealing conditions. In the case that the system underlies a peritectic decomposition during the annealing treatment, both the element composition and X-ray pattern will change.

A special form of segregation in solids is the eutectic solidification<sup>91</sup>, which results due to a miscibility gap in the composition, leading to dendritic microstructures. A binary phase diagram, pictured in Figure 20<sup>91</sup>, exemplifies the progress in the microstructure during the solidification process. The rapid cooling of a single-phase binary alloy (I) with the composition  $c_0$  will cause the formation of solid particles (a-rich) with the composition  $c_1$  at the intersection with the liquidus line (II). With increasing cooling rate, the melt is progressively depleted in compound  $a$ , resulting in a further grain growth of the main phase particles (III). A simultaneous segregation phase  $a$  and phase  $b$  appear as the eutectic point  $c_E$  is reached. The resulting microstructure consists of particles of the main phase, which are embedded by alternate lamellae of the eutectic composition containing two phases with the composition  $c_a$  and  $c_b$  (IV).

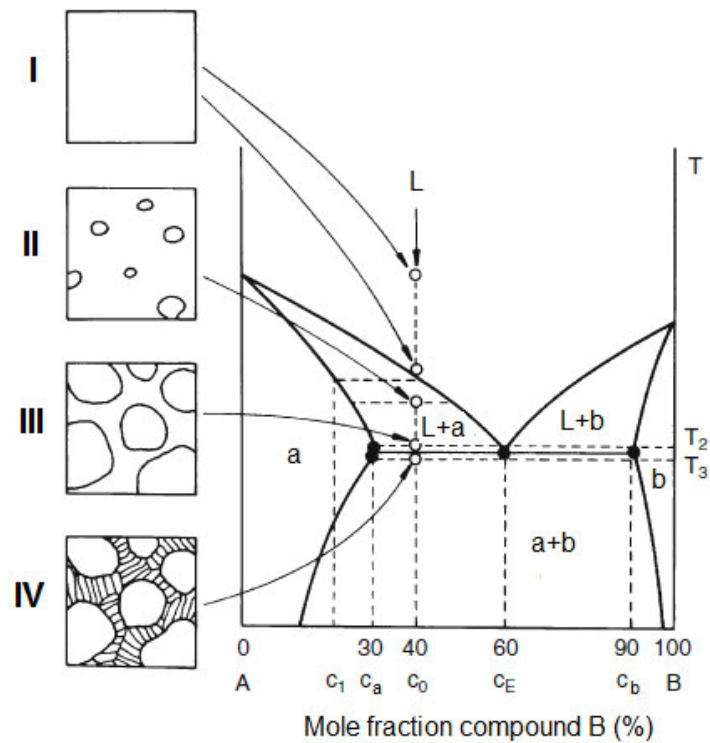


Figure 20 Schematic the eutectic solidification of a binary compound under rapid cooling<sup>91</sup>.

## 4 Experimental methods

### 4.1 Synthesis and chemical characterization

All HH compounds were synthesized by arc melting (Figure 21) of stoichiometric amounts of the constituent elements, shown in Table 1, under high purity Ti-gettered argon gas atmosphere on a water-cooled copper crucible. To ensure the homogeneity, the samples were re-melted several times. The cast alloys were usually annealed in evacuated quartz tubes at 1273 K for 7 days to improve their crystalline order, followed by quenching in ice water.



Figure 21 Picture of the arc melting setup taken at the University Mainz.

In the case of Sb substitution, the samples were prepared by the conventional cold-pressing sintering method (CCS) to ascertain the accurate stoichiometry and homogeneous distribution of Sb in the samples. The elements of the parent compound were pre-alloyed by arc melting, crushed and mixed with the respective amount of Sb, and subsequently milled under argon gas atmosphere for 8 h with a planetary high energy ball mill (Fritsch Planeten-Mikromühle *Pulverisette 7 premium line*). The obtained powder was cold pressed and sintered again by arc melting. Finally, the cast samples were annealed in evacuated quartz tubes at 1273 K for 7 days to improve their crystalline order, followed by quenching in ice water.

The investigation of a nanostructure approach was carried out using the spark plasma sintering (SPS) technique. The annealed samples were milled in an argon gas atmosphere for 6 h with a planetary high energy ball mill (Fritsch Planeten-Mikromühle *Pulverisette 7*). The obtained powder was sintered via SPS at 1050 °C for 10 min. The temperature profile was performed in a pulse mode with a heating rate of 50 K under a pressure of 8 kN.

The crystal structure was analyzed by powder X-ray diffraction (PXRD) at room temperature using  $\text{CuK}\alpha_1$  and  $\text{CrK}\alpha_1$  radiation (Bruker AXS D5000 and Guinier-Huber image plate system G670). The chemical compositions of the obtained samples, with an accuracy of approximately 0.5-0.3 at%, were examined by scanning electron microscopy (SEM) using the Philips XL30 scanning electron microscope. Quantitative electron probe microanalysis (EPMA) of the phases was carried out using an energy-dispersive X-Ray analyzer (Phoenix V 5.29, EDAX) and a wavelength-dispersive X-Ray analyzer (Cameca SX 100), with an acceleration voltage of 20 - 25 kV using the *K*- and *L*-lines in the spectrum. For the correction of the quantitative data the *ZAF* method was applied, which relies on the atomic number (*Z*), the absorption (*A*) and the fluorescence (*F*) of the sample. The microstructure was determined using the imaging method of detected back scattered electrons (BSE). The intensity of this detection mode depends on the atomic number of the elements, where heavy elements have a strong backscattering effect, indicating areas with bright contrasts. Thermal analysis was performed on a Netzsch STA 449.

**Table 1: List of the constituent elements used for the preparation of the half-Heusler compounds**

Element	Shape	Supplier	Purity
<b>Titanium (Ti)</b>	metal wire 1.0 mm	Chempur	99.8%
<b>Zirconium (Zr)</b>	metal sponge 3-6 mm	Chempur	99.8%
<b>Hafnium (Hf)</b>	metal pieces < 55mm	Chempur	99.8%
<b>Nickel (Ni)</b>	metal wire 1.0 mm	Chempur	99.98%
<b>Tin (Sn)</b>	metal granulat	Chempur	99.99 %
<b>Vanadium (V)</b>	metal granulat 2-10 mm	Smart elements	99.9%
<b>Niob (Nb)</b>	metal granulat 2-10 mm	Chempur	99.9%
<b>Antimony (Sb)</b>	powder	Chempur	99,999%
<b>Scandium (Sc)</b>	metal pieces	Smart elements	99.9%
<b>Yttrium (Y)</b>	metal granulat	Smart elements	99.99%
<b>Cobalt (Co)</b>	metal shots	Alfa Aesar	99,95%

## 4.2 Thermal Transport measurements

The electrical conductivity  $\sigma$  and Seebeck coefficient  $\alpha$  were simultaneously measured with a LSR-3 system in a helium gas atmosphere from room temperature up to 900 K. The samples were cut into a rectangular bar and were clamped between two thermocouples as shown in Figure 22. The high temperature data were analyzed using constantan as the reference material. The measurement uncertainty for  $\alpha$  and  $\sigma$  carried out on the LSR-3 is 8%.

The carrier concentration  $n$  and the carrier mobility  $\mu$  were determined by Hall measurements using the Van der Pauw technique from room temperature to 873 K. Four pressure-assisted contacts were placed at the edges of the sample disk. A perpendicular to the sample plane magnetic field was applied to the sample, while a diagonal current was passed through the disk.

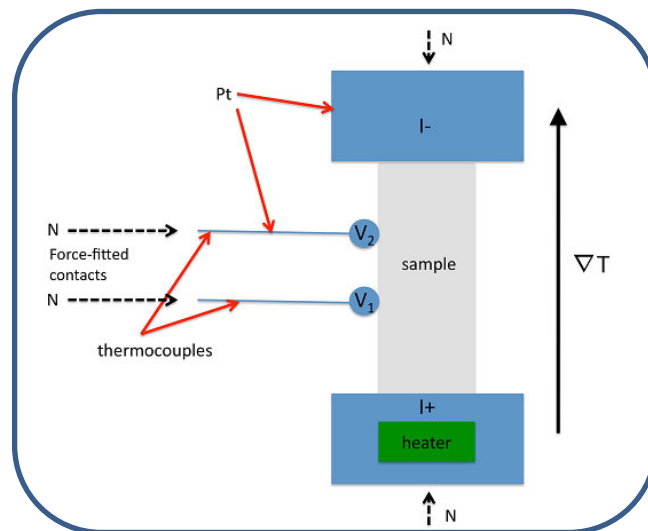


**Figure 22** Illustration of the Seebeck coefficient  $\alpha$  and electrical conductivity  $\sigma$  measurement on the LSR-3 system, where the sample is clamped between two thermocouples.

The thermal conductivity  $\kappa$  was evaluated as a product of the thermal diffusivity  $D$ , the heat capacity  $c_p$  and the measured density  $\rho$ . The density  $\rho$  of the ingots was calculated using the geometrical approach by measuring the weight and dimensions of the rectangular bar. The thermal diffusivity  $D$  was measured by a laser flash method with a Netzsch LFA 457 apparatus. The disk shaped samples were coated with a thin layer of graphite to minimize emissivity errors. The data were analyzed using a radiation model with pulse correction. The heat capacity  $c_p$  was measured by differential scanning calorimetry (DSC) with a Netzsch STA 449 instrument, using a sapphire standard with a diameter of 0.5 and 1.0 mm. The



measurement errors of  $D$  in the LFA 457 and of  $c_p$  in the STA 449 is 3% and 2%, respectively. Errors in  $\rho$  and the thickness of the samples will contribute to the overall measurement uncertainty of at least 5% for the estimation of the thermal conductivity  $\kappa$ . Under consideration of the error propagation, the error in the  $zT$  is about 25%.

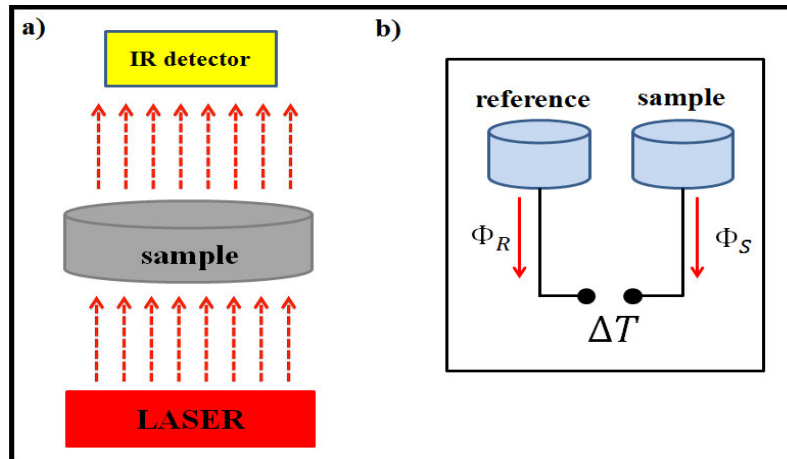


Figure 23 a) Schematic of the laser flash method in order to measure the thermal diffusivity  $D$ . A laser irradiates the graphite coated sample via short pulse, while the temperature on the other side of the sample is monitored by an IR detection<sup>37</sup>. b) Schematic of the DSC measurement in order to measure the specific heat  $c_p$  and the melting point.

## 5 TE properties of $\text{Ti}_{0.3}\text{Zr}_{0.35}\text{Hf}_{0.35}\text{NiSn}$

In order to improve the TE efficiency, *Sakurada et al*<sup>69</sup> have studied the effect of Ti substitution on the TE properties in  $\text{Ti}_x(\text{Zr,Hf})_{1-x}\text{NiSn}$ . Their results revealed that the thermal conductivity can be reduced significantly with  $x = 0.3$  Ti content to  $\kappa \sim 3$  W/Km at room temperature. This strong decline in  $\kappa$  has two origins. First, the high mass strain and disorder within the  $\text{Cl}_b$  structure due to the Ti substitution at the X-site leads to an effective phonon scattering. Secondly, this multi-component HH system reveals an intrinsic phase separation into two HH phases, which provides a further scattering of phonons at the interfaces.

Since HH materials comply with many of the requirements for TE applications at high temperatures, ranging from high TE efficiency  $zT$ , environment-friendliness, via low cost and temperature stability, this approach involving an induced eutectic microstructure can be the key for improving the TE performances of HH compounds beyond the limit of  $zT \sim 1$  for industrial application. Inspired by the great potential of the  $n$ -type  $\text{Ti}_{0.3}\text{Zr}_{0.35}\text{Hf}_{0.35}\text{NiSn}$  HH compound, one aim of this work is focused on the investigation of the intrinsic phase separation and the TE properties in this HH compound in dependency of different annealing conditions.

### 5.1 Properties of $\text{Ti}_{0.3}\text{Zr}_{0.35}\text{Hf}_{0.35}\text{NiSn}$ HH compound

The special characteristic of HH materials based on the  $\text{Ti}_x\text{Zr}_y\text{Hf}_z\text{NiSn}$  system is the intrinsic phase separation, which occurs in a rapid solidification process<sup>80,85</sup>. The  $n$ -type  $\text{Ti}_{0.30}\text{Zr}_{0.35}\text{Hf}_{0.35}\text{NiSn}$  compound undergoes a spontaneous phase separation into two HH phases, shown in Figure 24. The eutectic microstructure consists of a main Ti-poor HH 1 phase (grey phase), which solidifies first and a Ti-rich HH 2 phase (dark phase), which is dendritically interlaced through the microstructure. Due to the rapid solidification method, small constitutional variations occur in the composition, leading to the precipitation of small Sn impurities, which are homogeneously distributed throughout the dendritic microstructure with an average size of about 5-10  $\mu\text{m}$ . The composition of the two HH phases carried out by electron microscope phase analysis (EMPA) was found to be  $\text{Ti}_{0.18}\text{Zr}_{0.40}\text{Hf}_{0.41}\text{NiSn}$  for the Ti-poor HH 1 phase and  $\text{Ti}_{0.65}\text{Zr}_{0.20}\text{Hf}_{0.17}\text{NiSn}$  for the Ti-rich HH 2 phase. It seems that Ti is the driving force of the intrinsic phase separation since the two HH phases differs the most in the Ti content. The formation of these HH 1 and HH 2 phases is strongly kinetically favored. Efforts to attain these two HH phases as single phase materials revealed also phase

separations in the sample, resulting from constitutional changes under the solidification conditions. Due to the lack of a phase diagram of this multi-component HH compound, it can be assumed that this composition is close to the eutectic one. Thermal transport measurements confirm this assumption, since this parent  $\text{Ti}_{0.3}\text{Zr}_{0.35}\text{Hf}_{0.35}\text{NiSn}$  compound shows the lowest thermal conductivity in this  $\text{Ti}_x\text{Zr}_y\text{Hf}_z\text{NiSn}$  system<sup>68,92,93</sup>.

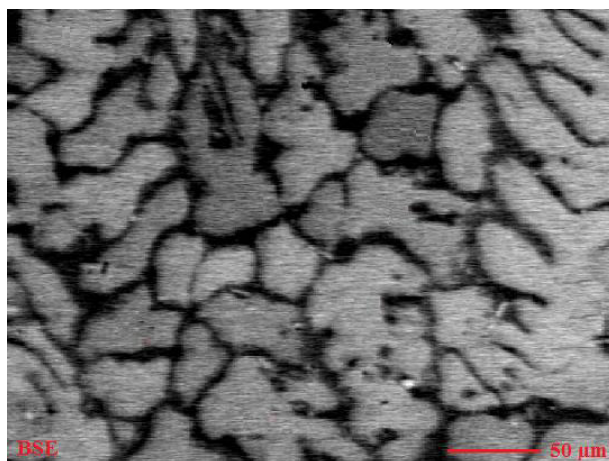


**Figure 24 SEM image (BSE) of  $\text{Ti}_{0.3}\text{Zr}_{0.35}\text{Hf}_{0.35}\text{NiSn}$  emphasizing the intrinsic phase separation in the Ti-poor HH 1 phase (grey) and the Ti-rich HH 2 phase (black), which is dendritically interlaced through the microstructure.**

The thermal analysis of  $\text{Ti}_{0.3}\text{Zr}_{0.35}\text{Hf}_{0.35}\text{NiSn}$  were performed by Dr. M.P. Schmidt at Max Planck Institute for Chemical Physics of Solids (Dresden) carried out by differential scanning calorimetric (DSC) up to 2000 K in argon gas atmosphere with a heating rate of 10 K/min. The DSC curve shows two endothermic reactions at 1680 K and 1720 K (Figure 25), indicating the eutectic and the melting point of  $\text{Ti}_{0.3}\text{Zr}_{0.35}\text{Hf}_{0.35}\text{NiSn}$ , respectively. This incongruently melted compound reveals a strong exothermic recrystallization peak at 1620 K. The supercooling behavior is a result of the decelerated nucleation in the compound. The melting and recrystallization peaks at about 503 K are caused by Sn impurities in the sample.

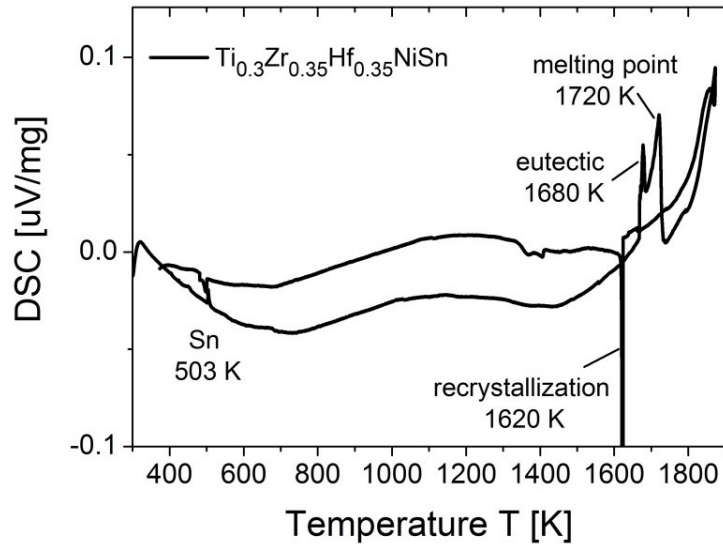


Figure 25 DSC measurement of  $\text{Ti}_{0.3}\text{Zr}_{0.35}\text{Hf}_{0.35}\text{NiSn}$  exemplifies the eutectic temperature at 1680 K and the melting point at 1780 K. The supercooled melt recrystallized at 1680 K. The peaks at 503 K indicate Sn impurities.

Specific heat  $c_p$  measurements of the parent  $\text{Ti}_{0.3}\text{Zr}_{0.35}\text{Hf}_{0.35}\text{NiSn}$  compound were performed by Dr. W. Schnelle at Max Planck Institute for Chemical Physics of Solids (Dresden) using a PPMS. Since the parent compound has a large number of atoms in the unit cell, many phonon modes appear above room temperature. The Deby temperature was determined to be  $\Theta_D$  330 K (Figure 26). For  $T \gg \Theta_D$  the specific heat capacity  $c_p$  reached its Dulong-Petit limit of  $3R$ , corresponding to the value of  $c_p \sim 0.26 \text{ J/gK}$ .

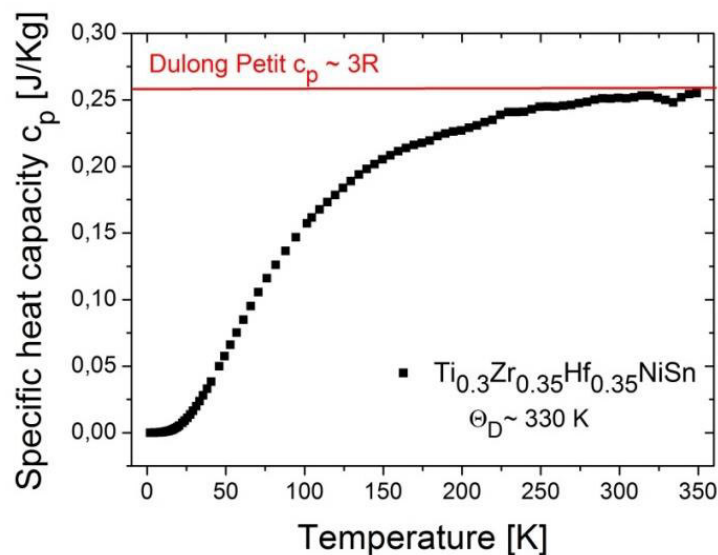
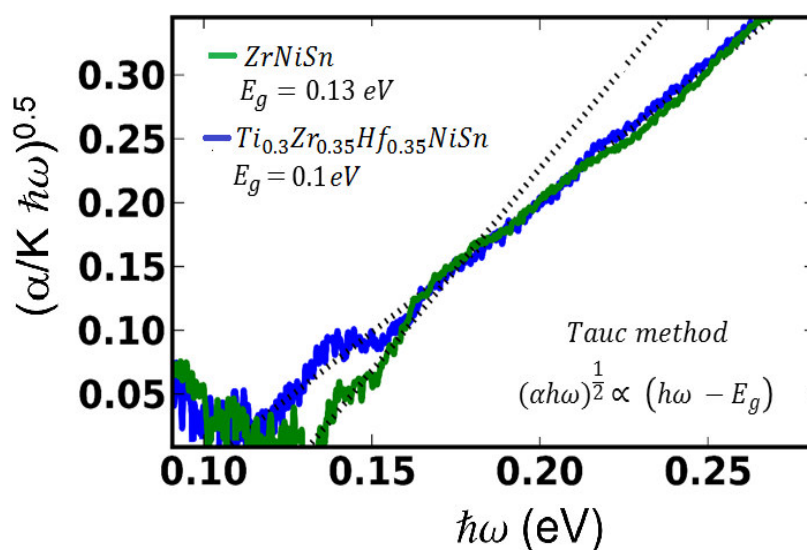


Figure 26 Specific heat capacity  $c_p$  measurement of the *n*-type  $\text{Ti}_{0.3}\text{Zr}_{0.35}\text{Hf}_{0.35}\text{NiSn}$  HH compound, indicating the Dulong-Petit limit of  $3R$  for  $T \gg \Theta_D$ .

The optical band gap measurements were performed by Zachary M. Gibbs at California Institute of technology (CalTech) using the diffuse reflectance infrared Fourier transform spectroscopy method (DRIFTS) at the California Institute of Technology, Pasadena, USA. The measurement revealed an indirect band gap of 0.1 eV (Figure 27) in  $\text{Ti}_{0.3}\text{Zr}_{0.35}\text{Hf}_{0.35}\text{NiSn}$ . The physical properties of HH materials are very sensitive to the structural arrangement. In particular, the size of the band gap decreases with the number of anti-site defects in the  $\text{C1}_b$  structure<sup>64,65</sup>. Thus, most of the HH materials are narrow band gap semiconductors.



**Figure 27** Normalized Kubelka Munk function of pure ZrNiSn and  $\text{Ti}_{0.3}\text{Zr}_{0.35}\text{Hf}_{0.35}\text{NiSn}$  with the absorption coefficient including the linear fit (red dotted line) which was used to estimate the band gap from the Tauc method.

Hall measurements were performed by J. Schmitt at California Institute of Technology (CalTech). Owing to the narrow band gap in  $\text{Ti}_{0.3}\text{Zr}_{0.35}\text{Hf}_{0.35}\text{NiSn}$ , additional charge carriers can easily be activated by thermal excitation. The temperature dependence of the carrier concentration  $n_H$ , shown in Figure 28, revealed the strong increase in the quantity of carriers with increasing temperature. The mobility  $\mu_H$  showed the opposite trend with temperature. The variation in  $\mu_H$  with temperature can be described by the power law equation:  $\mu \propto T^{-\nu}$ , where the value of  $\nu$  is an indicator of the most dominant scattering mechanism in the system. For phase-separated HH compounds, Xie *et al* were able to show that the major mechanism is alloy scattering ( $\nu = 1.5$ )<sup>94</sup>. Thus, the decrease in  $\mu_H$  is mainly caused by different scattering mechanisms of charge carriers.

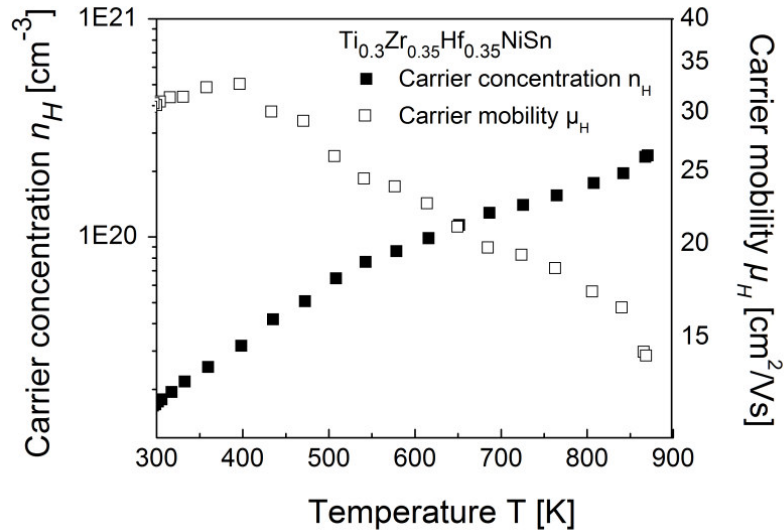


Figure 28 Hall measurements of the  $n$ -type  $\text{Ti}_{0.3}\text{Zr}_{0.35}\text{Hf}_{0.35}\text{NiSn}$  compound with the temperature dependence of the Hall carrier concentration  $n_H$  and the Hall mobility  $\mu_H$  from 300 to 900 K.

## 5.2 Influence of annealing time in $\text{Ti}_{0.3}\text{Zr}_{0.35}\text{Hf}_{0.35}\text{NiSn}$

Usually HH materials are prepared by arc melting. This synthesis method provides a rapid solidification but also cause a high strain and disorder in the structure and impurity phases, such as Sn,  $\text{Ti}_6\text{Sn}_5$  and  $(\text{Zr,Hf})_5\text{Sn}_3$ <sup>36</sup>. In order to eliminate the impurity phases and to stabilize the system in a thermodynamic equilibrium, an annealing treatment is necessary. The effect of annealing time on the TE properties was investigated in the  $\text{Ti}_{0.3}\text{Zr}_{0.35}\text{Hf}_{0.35}\text{NiSn}$  system. The as-cast HH samples were annealed at 950 °C for 3 and 7, and at 1000 °C for 21 days.

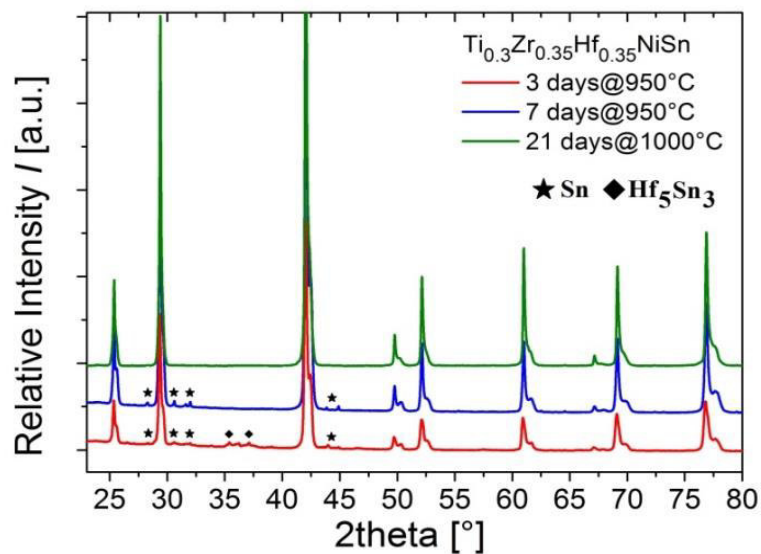


Figure 29 PRXD pattern of  $\text{Ti}_{0.3}\text{Zr}_{0.35}\text{Hf}_{0.35}\text{NiSn}$  samples annealed at 950 °C for 3 and 7 days and at 1000 °C for 21 days. Black stars indicate Sn impurities, black rhombus indicate  $\text{Hf}_5\text{Sn}_3$  impurity phases.

The crystalline structure was determined by powder X-ray diffraction (PXRD) measurements using Cu-K $\alpha$  radiation. The obtained X-Ray pattern, shown in Figure 29, is in excellent agreement with the cubic C1 $_b$  structure (F $\bar{4}3m$ ) found in the literature<sup>95</sup>. The Bragg reflection peak splitting indicates the coexistence of two HH phases, a Ti-poor HH 1 and Ti-rich HH 2 phase. Small amounts of Sn and Hf<sub>5</sub>Sn<sub>3</sub> impurity phases can be found in the 3-days-annealed sample, which can be removed with prolonged annealing treatment<sup>36</sup> according to Ostwald rippling. The lattice parameter  $a$  was determined using a LaB<sub>6</sub> standard. The results of the PXRD measurements of the Ti<sub>0.3</sub>Zr<sub>0.35</sub>Hf<sub>0.35</sub>NiSn samples in dependence of annealing duration are listed in Table 2. The HH 1 phase exhibits a larger lattice parameter, due to the higher amounts of the greater sized Zr (159 pm) and Hf (156 pm) elements in this HH phase. The HH 2 phase can usually be indicated as a broad shoulder (Figure 29) at higher 2 theta values (smaller lattice constant), owing to higher fractions of the smaller Ti (145 pm) in HH 2. No decomposition reaction of HH 1 and HH 2 was observed in the samples, indicating the temperature stability of the phase separation in this temperature regime. The lattice parameter of both HH phases revealed only slightly changes in the HH 1 value after 3- and 21-days annealing. The phase fractions of HH 1 and HH 2 were estimated from the X-ray diffraction pattern. It can be seen, that with extended annealing time the phase fraction ratio slightly changed in favor of the Ti-rich HH 2 phase in the samples (Table 2), owing to element diffusion.

**Table 2 Lattice parameter, chemical composition and phase fraction of the Ti-poor HH1 and Ti-rich HH2 phase in Ti<sub>0.3</sub>Zr<sub>0.35</sub>Hf<sub>0.35</sub>NiSn depending on the annealing time.**

Ti <sub>0.3</sub> Zr <sub>0.35</sub> Hf <sub>0.35</sub> NiSn	Lattice parameter $a$ [Å]	Composition [at%]	Phase fraction HH1:HH2 [wt%]
<b>Annealed for 3 days at 950 °C</b>			
Ti-poor phase (HH 1)	$a = 6.073 \text{ \AA}$	Ti <sub>0.18</sub> Zr <sub>0.40</sub> Hf <sub>0.41</sub> NiSn	80
Ti-rich phase (HH 2)	$a = 6.017 \text{ \AA}$	Ti <sub>0.62</sub> Zr <sub>0.22</sub> Hf <sub>0.20</sub> NiSn	20
<b>Annealed for 7 days at 950 °C</b>			
Ti-poor phase (HH 1)	$a = 6.070 \text{ \AA}$	Ti <sub>0.15</sub> Zr <sub>0.41</sub> Hf <sub>0.43</sub> NiSn	75
Ti-rich phase (HH 2)	$a = 6.011 \text{ \AA}$	Ti <sub>0.65</sub> Zr <sub>0.20</sub> Hf <sub>0.18</sub> NiSn	25
<b>Annealed for 21 days at 1000 °C</b>			
Ti-poor phase (HH 1)	$a = 6.068 \text{ \AA}$	Ti <sub>0.12</sub> Zr <sub>0.43</sub> Hf <sub>0.45</sub> NiSn	70
Ti-rich phase (HH 2)	$a = 6.010 \text{ \AA}$	Ti <sub>0.67</sub> Zr <sub>0.18</sub> Hf <sub>0.16</sub> NiSn	30

The intrinsic phase separation revealed only a weak dependence on the annealing time (Figure 30). The dendritic microstructure can be maintained after 21-days annealing at 1000 °C. Consistent with the PXRD measurements, an increase of the HH 2 phase fraction can be observed with increasing annealing time, resulting in a slightly reduction of the dendritic interfaces. This is surprising because usually long-term annealing causes a resolution of the dendritic microstructure<sup>91</sup>. The nominal composition, presented in Table 2, was examined by EPMA using a wavelength dispersive X-ray detector. The samples showed negligible variations in their element composition. Due to the high melting point (1720 K, see section 5.1) of this HH compound, the intrinsic phase separation is extraordinary temperature stable in the moderate temperature range.

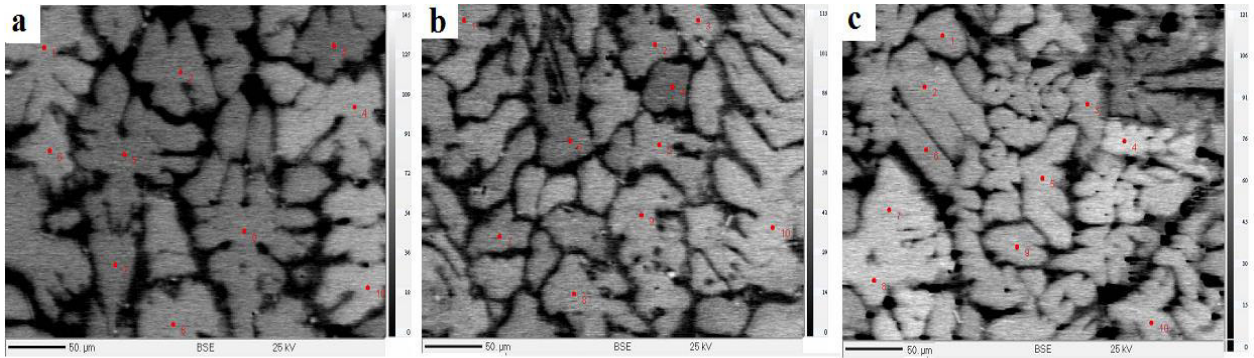


**Figure 30** SEM images (BSE) of the *n*-type  $\text{Ti}_{0.3}\text{Zr}_{0.35}\text{Hf}_{0.35}\text{NiSn}$  samples. a) annealed for 3 days at 950°C, b) annealed for 7 days at 950 °C and c) annealed for 21 days at 1000 °C.

Thermal transport measurements of  $\text{Ti}_{0.3}\text{Zr}_{0.35}\text{Hf}_{0.35}\text{NiSn}$  were performed from 300 to 900 K. The temperature dependence of the electrical conductivity  $\sigma$  increased monotonously with rising temperature, indicating semiconducting behavior (Figure 31 a) and showed almost no dependence on the annealing duration<sup>96</sup>. In comparison to in conventional semiconductors, where  $\sigma$  is about  $10^{-2}$ - $10^{-6}$  S/cm<sup>97</sup>, this HH compound reveals much higher  $\sigma$  values, due to the narrow band gap (0.1 eV) and high carrier concentration. The Seebeck coefficient  $\alpha$  was negative over the whole temperature range, emphasizing the intrinsic *n*-type conduction of this compound. The maximum thermopower can be improved with prolonged annealing from -230 to -250  $\mu\text{V/K}$  (Figure 31 b), owing to a change in the DOS. The extended annealing time caused a distinct reduction of anti-site defects, leading to an improvement of the DOS near the Fermi level, which in turn enhanced the Seebeck coefficient<sup>65,96</sup>. The decrease in  $\alpha$  above 600°K results from higher quantities of carriers due to the thermal excitation<sup>35</sup>. The thermal conductivity was determined as  $\kappa = D * c_p * \rho$ , i.e. the product of the thermal diffusivity  $D$ , the specific heat  $c_p = 0.28$  J/gK and the density  $\rho = 8.35\text{g/cm}^3$ . The obtained thermal



conductivity  $\kappa$  of these samples is reduced compared to ternary HH compounds such as ZrNiSn, which usually exhibits  $\kappa$  values about 7~17 W/Km<sup>35</sup>. The significant reduction of  $\kappa$  is a result of higher contribution of phonon scattering at point defects due to the site substitution and at interfaces owing to the intrinsic phase separation. An extended annealing duration led to a further reduction of  $\kappa$  (Figure 31 c), probably caused by dislocation defects in the microstructure (see section 7.2), which might act as additional scattering centers. The upturn in  $\kappa$  at higher temperatures is caused by the thermal activation of minority carriers. Despite the observed changes in  $\alpha$  and  $\kappa$ , the resulting figure of merit,  $zT$  exhibited similar values for all samples (Figure 31 d). The highest  $zT$  value of 0.68 at 773 K is reached in the 21-days-annealed sample, due to the low thermal conductivity in this sample. This suggests that the TE performance of HH materials becomes better with prolonged annealing treatment. Applying this to TE applications, one might assume that the TE efficiency of HH materials will not deteriorate and can be maintained under operating conditions. These results demonstrate the superior suitability of phase-separated HH materials for TE applications at moderate temperatures.

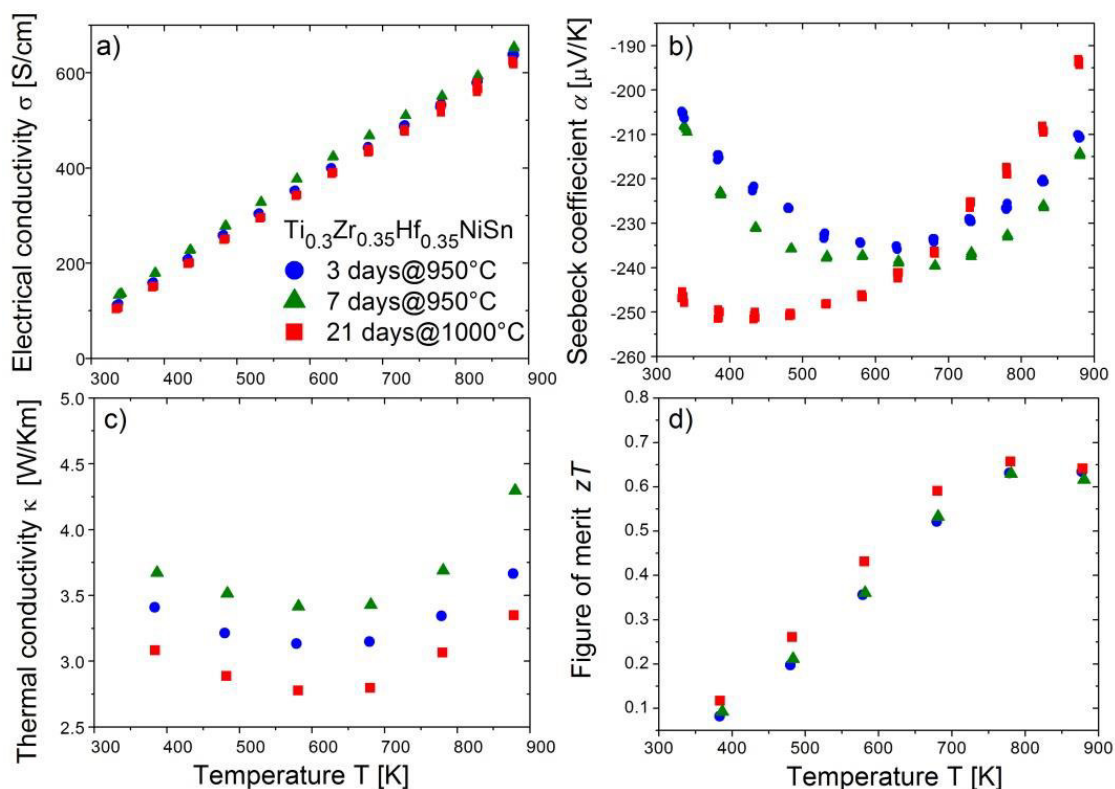


**Figure 31** Temperature dependence of the a) electrical conductivity  $\sigma(T)$ , b) Seebeck coefficient  $\alpha(T)$ , c) thermal conductivity  $\kappa(T)$  and d) figure of merit  $zT(T)$  in  $\text{Ti}_{0.3}\text{Zr}_{0.35}\text{Hf}_{0.35}\text{NiSn}$  samples from 300 to 900 K annealed for 3, 7 and 21 days.

### 5.3 Influence of annealing temperature in $\text{Ti}_{0.3}\text{Zr}_{0.35}\text{Hf}_{0.35}\text{NiSn}$

In the previous section, it was shown that long-term annealing at a certain temperature has only a weak influence of the TE properties in the parent  $\text{Ti}_{0.3}\text{Zr}_{0.35}\text{Hf}_{0.35}\text{NiSn}$  HH compound. Therefore, the influence of annealing temperature for short annealing durations was investigated in this HH material. For this purpose, the samples were cut into rectangular bars and were subjected to different temperature profiles from 750 to 1200 °C for 2 h and 1 day, respectively and were subsequently quenched in ice water.

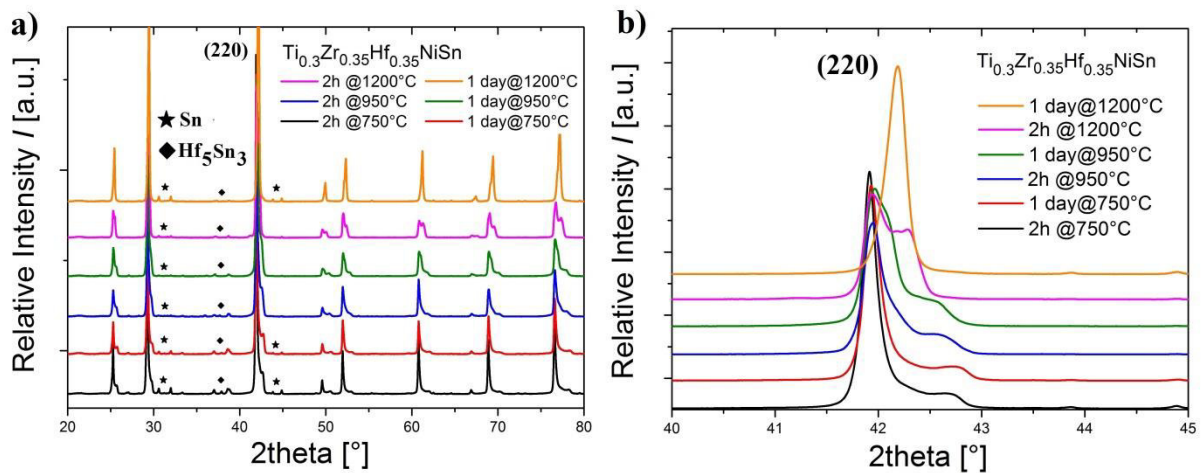


**Figure 32** PRXD pattern of  $\text{Ti}_{0.3}\text{Zr}_{0.35}\text{Hf}_{0.35}\text{NiSn}$  samples annealed at different temperatures. Black stars indicate Sn impurities, black rhombus indicate  $\text{Hf}_5\text{Sn}_3$  impurity phases.

The X-ray powder pattern revealed the cubic  $C1_b$  structure and Sn and  $\text{Hf}_5\text{Sn}_3$  impurity phases in all samples (Figure 32 a). The highest amount of impurities was found in the samples annealed at 1200 °C. The diffraction peak splitting was observed in all samples, besides the sample annealed at 1200 °C for 1 day, which showed a distinct broadening of the Bragg reflexes. The results obtained from PXRD measurements are shown in Table 3. The lattice parameter of HH 1 remained constant in the samples annealed at 750 and 950 °C. The lattice parameter  $a$  of the Ti-rich HH 2 revealed a shift to smaller 2 theta values (larger  $a$  values) with higher annealing temperature and extended annealing time (Table 3 and Figure 32 b), indicating a change of the element composition in the samples.

**Table 3 Lattice parameter and phase fraction of the Ti-poor HH 1 and Ti-rich HH 2 phase in  $\text{Ti}_{0.3}\text{Zr}_{0.35}\text{Hf}_{0.35}\text{NiSn}$  HH depending on the annealing temperature.**

$\text{Ti}_{0.3}\text{Zr}_{0.35}\text{Hf}_{0.35}\text{NiSn}$	Lattice parameter $a$ [Å]	Phase fraction HH1:HH2 [wt%]
<b>annealed at 750 °C for 2 h</b>		
Ti-poor phase (HH 1)	$a = 6.089 \text{ \AA}$	95
Ti-rich phase (HH 2)	$a = 5.978 \text{ \AA}$	5
<b>annealed at 750 °C for 1 day</b>		
Ti-poor phase (HH 1)	$a = 6.087 \text{ \AA}$	94
Ti-rich phase (HH 2)	$a = 5.981 \text{ \AA}$	6
<b>annealed at 950 °C for 2 h</b>		
Ti-poor phase (HH 1)	$a = 6.084 \text{ \AA}$	90
Ti-rich phase (HH 2)	$a = 5.993 \text{ \AA}$	10
<b>annealed at 950 °C for 1 day</b>		
Ti-poor phase (HH 1)	$a = 6.084 \text{ \AA}$	80
Ti-rich phase (HH 2)	$a = 6.014 \text{ \AA}$	20
<b>annealed at 1200 °C for 2 h</b>		
Ti-poor phase (HH 1)	$a = 6.070 \text{ \AA}$	55
Ti-rich phase (HH 2)	$a = 6.036 \text{ \AA}$	45
<b>annealed at 1200 °C for 1 day</b>		
Ti-poor phase (HH 1)	$a = 6.073 \text{ \AA}$	n.a
Ti-rich phase (HH 2)		n.a.

SEM investigations of the  $\text{Ti}_{0.3}\text{Zr}_{0.35}\text{Hf}_{0.35}\text{NiSn}$  compound depending on the annealing temperature are presented in Figure 33. The typical intrinsic phase separation into two HH phases can be observed in all samples. The annealing treatment at 750 °C showed no obvious change in the dendritic microstructure with extended annealing time (Figure 33 a+d). The phase fraction of HH 1 and HH 2 remained constant in the samples annealed at 750 °C (Table 3). An increase in the annealing temperature up to 950 °C, indicates a reduction of the dendritic interfaces in the microstructure, accompany by a change of the phase fraction ratio in favor of the Ti-rich HH 2 phase (Table 3). The samples annealed at 1200 °C showed a further resolution of the two HH phases with prolonged annealing time (Figure 33 c+f), leading to a loss of the dendritic microstructure.

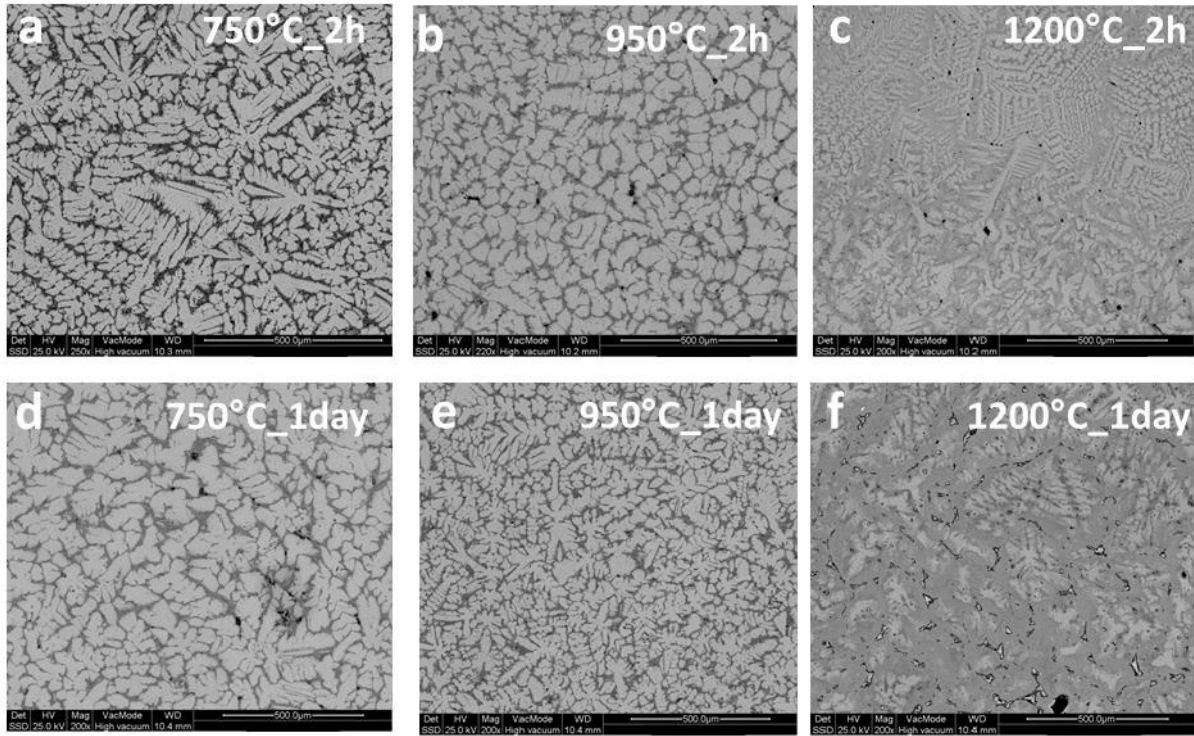


**Figure 33 SEM (BSE) images of  $\text{Ti}_{0.3}\text{Zr}_{0.35}\text{Hf}_{0.35}\text{NiSn}$  HH samples depending on the annealing temperature.**

The TE properties of the  $\text{Ti}_{0.3}\text{Zr}_{0.35}\text{Hf}_{0.35}\text{NiSn}$  samples depending on annealing temperature are presented in Figure 34. The sample annealed at 1200 °C for 1 day could not be measured, due to the modification of the sample bar under the annealing. It is noteworthy, that the TE properties are determined by all existing phases in the sample, also impurity phases. Therefore, the exact impact of annealing temperature on the TE properties in these samples should be considered with particular caution. The electrical conductivity  $\sigma$  showed semiconducting behavior in all samples. The samples annealed at a certain temperature showed a reduction in  $\sigma$  with extended annealing time (Figure 34 a), probably caused by the reduction of metallic impurity phases. The behavior of the Seebeck coefficient  $\alpha$  correlates with the electrical conductivity. The maximum value in  $\alpha$  increased with annealing temperature and annealing time, due to a higher structural order in the samples<sup>66</sup>. The power factor  $PF$  was evaluated from the measured data, and revealed a general improvement of the electronic properties ( $\alpha^2\sigma$ ) with annealing time and temperature, owing to the distinct enhancement in the Seebeck coefficient. The higher Power factor  $PF$  of  $3.5 \cdot 10^{-3} \text{W/K}^2\text{m}$  was attained in the sample annealed at 1200 °C for 2 h.

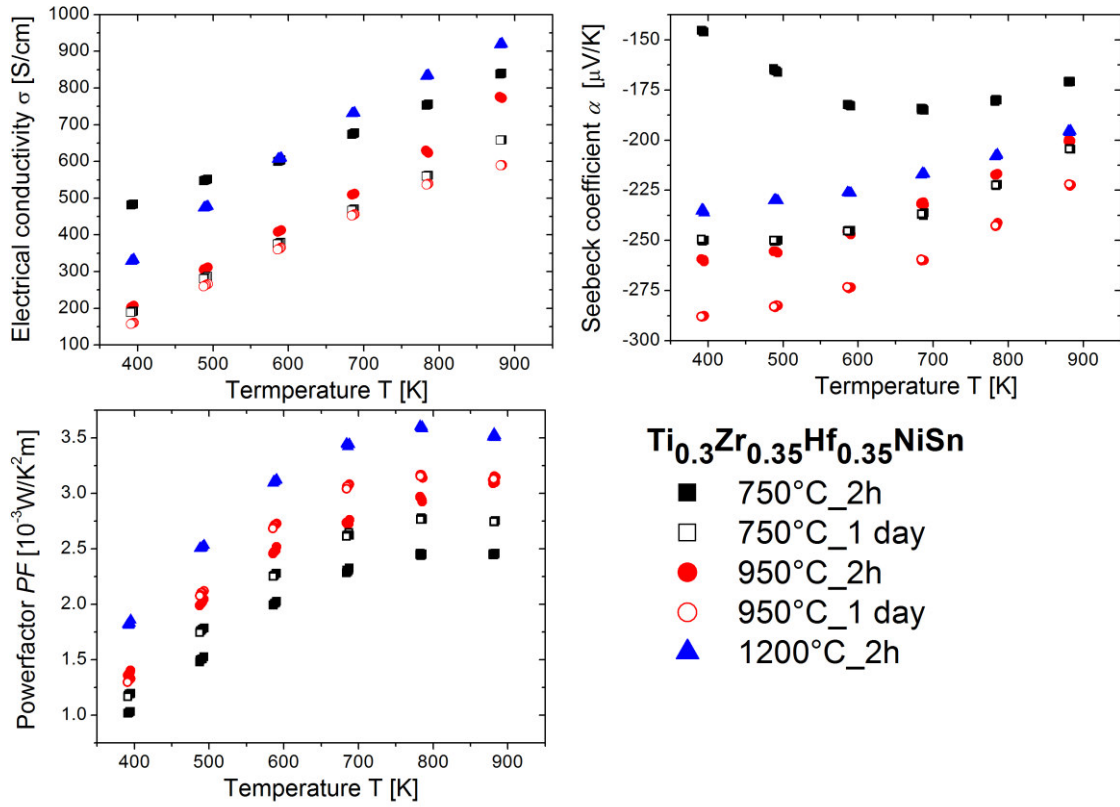


**Figure 34** Temperature dependence of the a) electrical conductivity  $\sigma(T)$ , b) Seebeck coefficient  $\alpha(T)$  and c) Power factor  $\alpha^2\sigma(T)$  in  $\text{Ti}_{0.3}\text{Zr}_{0.35}\text{Hf}_{0.35}\text{NiSn}$  samples annealed at different temperatures from 300 to 900 K.

## 6 Site substitution in $\text{Ti}_{0.3}\text{Zr}_{0.35}\text{Hf}_{0.35}\text{NiSn}$

The general strategy to attain *n*- and *p*-type HH materials for TE applications is realized by site substitution with non-isoelectronic elements. Site substitution provides two major effects on the enhancement of the TE efficiency. First, site substitution on different sublattices of the  $\text{C1}_b$  structure, cause a distinct reduction of the thermal conductivity owing to higher contributions of phonon scattering<sup>36,68</sup>. Second, the electronic doping of the HH system optimizes the electronic properties due to dopant-induced features near the Fermi level<sup>35,48</sup>. Furthermore, HH *n*- and *p*-type compounds based on one parent system, will allow the fabrication of TE material pairs with similar mechanical and TE properties. Thus, the probability of cracks and material distortion in the TE device can be reduced and better TE efficiencies can be attained under operating conditions.

Many reports have demonstrated the great suitability of phase-separated *n*-type HH materials for TE applications<sup>36,68</sup>. There have also been numerous studies on *p*-type HH materials<sup>67,78,98</sup>, although they do not have a sufficiently high TE potential compared to the *n*-type HH materials. This intrinsic *n*-type conduction emerges from anti-site disorder in the HH structure, owing to a shift of the Fermi energy to the conduction band. At this time, many of the fairly good *p*-type HH compounds are based on the *MCoSb* HH system<sup>72,73</sup>. However, in contrast to *MNiSn*-based HH materials, *MCoSb* decomposes above 750 K<sup>99</sup> and this limits its application as a TE material at high temperatures.

To provide a versatile application of HH materials for TE applications, compatible *n*- and *p*-type materials are essential. The second part of this work is aimed on the investigation of electronic doping in the *n*-type  $\text{Ti}_{0.3}\text{Zr}_{0.35}\text{Hf}_{0.35}\text{NiSn}$  HH compound, in order to find new promising *n*- and *p*-type TE materials, which can operate with high efficiency at moderate temperatures. Starting from this parent  $\text{Ti}_{0.3}\text{Zr}_{0.35}\text{Hf}_{0.35}\text{NiSn}$  compound, the optimization of the TE properties was proven via site substitution with donor and acceptor dopants on different sublattices in the  $\text{C1}_b$  structure, as shown in Figure 35. The effect of donor dopants, such as V, Nb and Sb was examined in order to optimize the *n*-type properties. Electronic doping with acceptor elements, such as Sc, Y and Co, was investigated to find suitable *p*-type materials based on the *MNiSn* HH system.

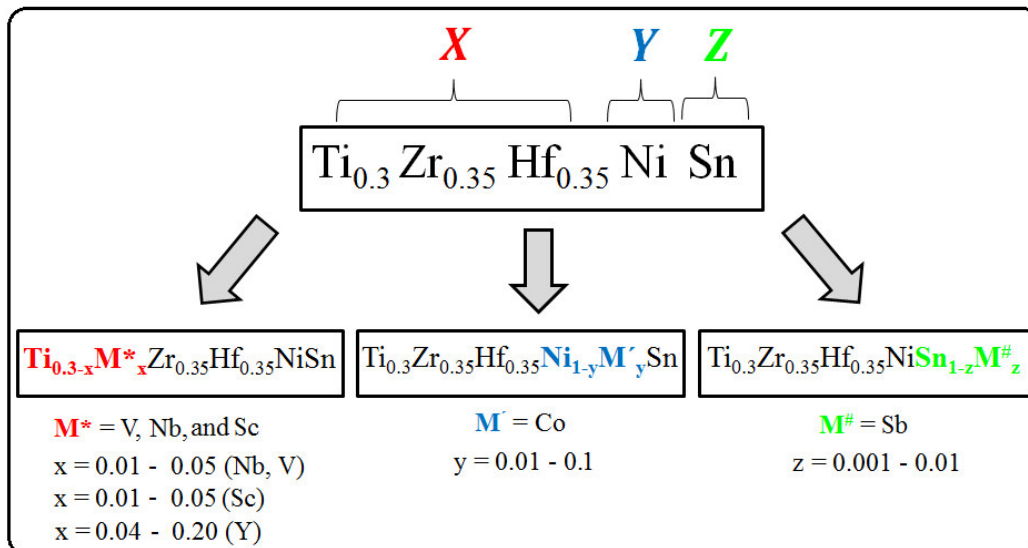
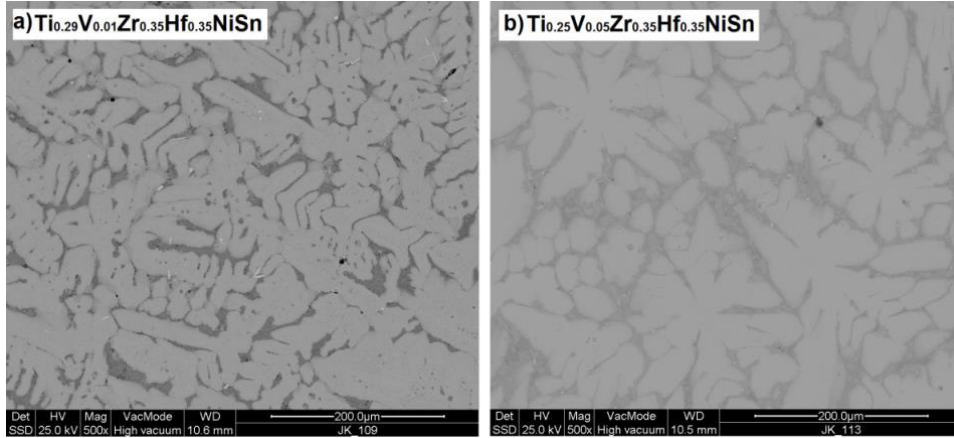


Figure 35 Schematic of the site substitution in the  $\text{Ti}_{0.3}\text{Zr}_{0.35}\text{Hf}_{0.35}\text{NiSn}$  HH compound.

## 6.1 Donor dopant-induced properties of $\text{Ti}_{0.3}\text{Zr}_{0.35}\text{Hf}_{0.35}\text{NiSn}$

### 6.1.1 $\text{Ti}_{0.3-x}\text{V}_x\text{Zr}_{0.35}\text{Hf}_{0.35}\text{NiSn}$ ( $x = 0.01, 0.03$ and $0.05$ )

The donor dopant effect of V ( $3d^5$ ) on the Ti ( $3d^4$ ) sublattice was examined in the *n*-type  $\text{Ti}_{0.3}\text{Zr}_{0.35}\text{Hf}_{0.35}\text{NiSn}$  HH system. All samples of  $\text{Ti}_{0.3-x}\text{V}_x\text{Zr}_{0.35}\text{Hf}_{0.35}\text{NiSn}$  ( $x = 0, 0.01, 0.03$  and  $0.05$ ) were attained in the cubic  $C1_b$  structure, confirming the successful formation of the desired HH structure. The diffraction pattern revealed peak splitting in all samples, due to the resulting intrinsic phase separation into two HH phases<sup>80</sup>. Also small amounts of Sn impurities were observed. The substitution of the smaller V atoms (131 pm) by Ti (145 pm) exhibited no change in the lattice parameter. This can be explained by the influence of impurity phases, which may cause an increase of the unit cell<sup>100</sup>. The lattice constant values were determined to be  $a = 6.069 \text{ \AA}$  and  $a = 6.012 \text{ \AA}$  for the Ti-poor HH 1 and the Ti-rich HH 2 phase, respectively. EMPA revealed small amounts of a Sn impurity, confirming the PXR D measurements. Further, small V inclusions were found in the 5% V sample. The SEM (BSE) images, shown in Figure 36, showed the expected intrinsic phase separation into the HH 1 and HH 2 phase. It can be seen, that the dendritic microstructure was not affected by the V substitution.



**Figure 36 SEM (BSE) images of a)  $\text{Ti}_{0.29}\text{V}_{0.01}\text{Zr}_{0.35}\text{Hf}_{0.35}\text{NiSn}$  and b)  $\text{Ti}_{0.25}\text{V}_{0.05}\text{Zr}_{0.35}\text{Hf}_{0.35}\text{NiSn}$  sample.**

The TE properties of the  $\text{Ti}_{0.3-x}\text{V}_x\text{Zr}_{0.35}\text{Hf}_{0.35}\text{NiSn}$  ( $x = 0, 0.01, 0.03$  and  $0.05$ ) HH samples are presented in Figure 37. For lower V doping levels, the electrical conductivity  $\sigma$  shows typical behavior of a doped semiconductor (Figure 37 a). The substitution of 5% V reveals rather a metal-like behavior in  $\sigma$ , probably due to the V inclusions. The  $\sigma$  value at 323 K drastically improved with increasing V substitution and started to converge at higher temperatures, as reaching the intrinsic conductivity regime. The Seebeck coefficient  $\alpha$  was negative over the whole temperature range for all samples, indicating electrons as majority charge carriers. The thermopower was enhanced with 1% V substitution from  $-240$  to  $-280 \mu\text{V/K}$  (Figure 37 b), suggesting the formation of local features in the DOS near to or within the band gap region<sup>48,100</sup>. These dopant-induced states near the Fermi energy contribute to a greater thermopower at lower temperatures, while above 600 K additional charge carriers, emerging from thermal excitation, minimize this benefit. Furthermore it can be seen, that with higher V content, the maximum of  $\alpha$  is shifted to higher temperatures, leading to an effective suppression of minority carriers. The V-electron doping donates further valence electrons to the HH system, causing a shift of the Fermi level to the bottom of the conduction band and moves to higher energies with increasing V content<sup>63</sup>. The power factor  $PF$  was calculated from  $\sigma$  and  $\alpha$  and is shown in Figure 37 c. Comparing the values at 373 K, it can be seen that the electronic properties ( $\alpha^2\sigma$ ) significantly increase in all V samples, indication that V is an effective donor dopant in this HH system. The highest power factor of  $4.0 \cdot 10^{-3} \text{ W/K}^2\text{m}$  at 723K was attained with 1% V concentration. The thermal conductivity  $\kappa$  decreases with 1% and 3% V substitution (Figure 37 d), owing to an improved disorder scattering. The highest  $\kappa$  values are observed in the 5% V sample, resulting from higher contributions of the electronic thermal conductivity  $\kappa_e$  due to the high electrical conductivity. The typical upturn in  $\kappa$  above



600 K, which is caused by the thermal excitation of minority carries, is shifted to higher temperature for the 5% V sample, due to the suppression of minority carriers.

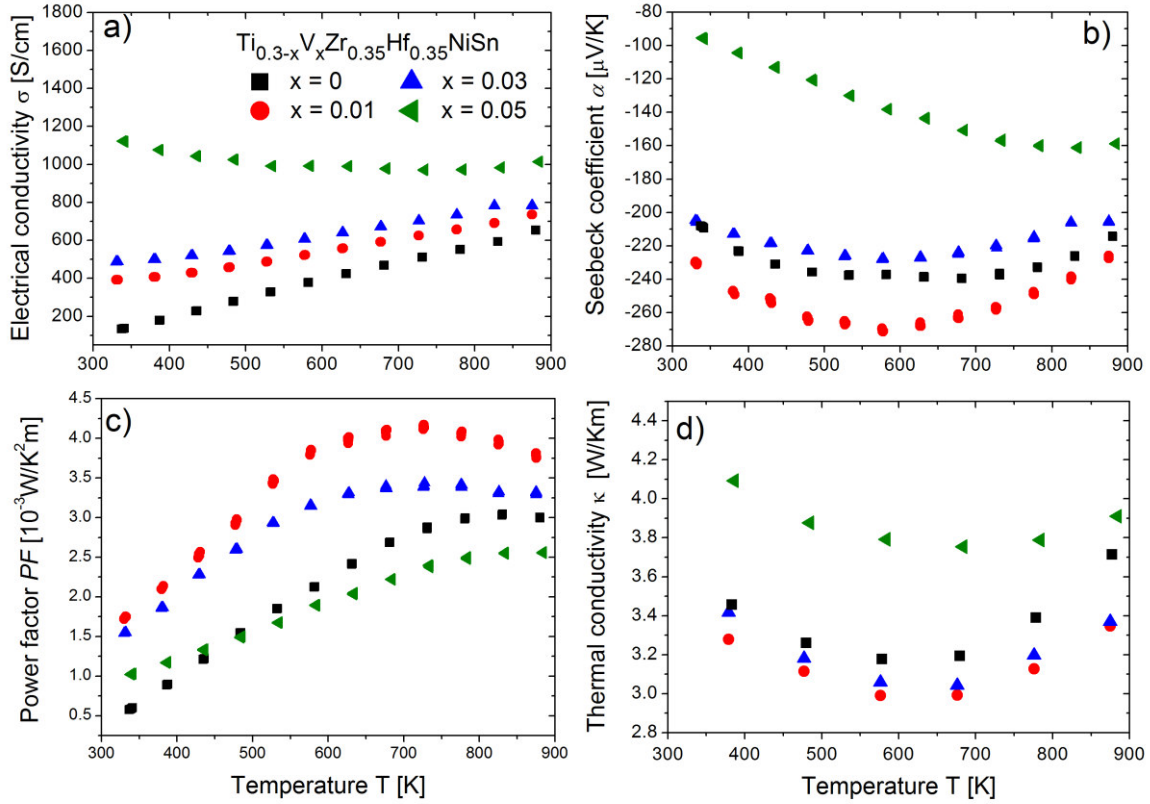


**Figure 37** Temperature dependence of the a) electrical conductivity  $\sigma(T)$ , b) Seebeck coefficient  $\alpha(T)$ , c) Power factor  $\alpha^2\sigma(T)$  and d) thermal conductivity  $\kappa(T)$  in  $\text{Ti}_{0.3-x}\text{V}_x\text{Zr}_{0.35}\text{Hf}_{0.35}\text{NiSn}$  ( $x = 0, 0.01, 0.03$  and  $0.05$ ) samples from 300 to 900 K.

Hall measurements are shown in Figure 38. The carrier concentration  $c_H$  revealed a significant increase with higher V concentration (Figure 38 a), confirming the dopant-induced enhancement in the electronic properties. The temperature dependence of  $c_H$  (Figure 38 a) showed a shallow rise with increasing temperature and V substitution, indicating the successful suppression of thermally excited minority carriers. The Hall mobility,  $\mu_H$  (Figure 38 b) decreased with increasing V concentration, caused by higher scattering of charge carriers. The temperature dependence in  $\mu_H$  follows the power law relation  $\mu \propto T^{-1.5}$ , indicating alloy scattering as the most dominant scattering mechanism in this system<sup>94</sup>.

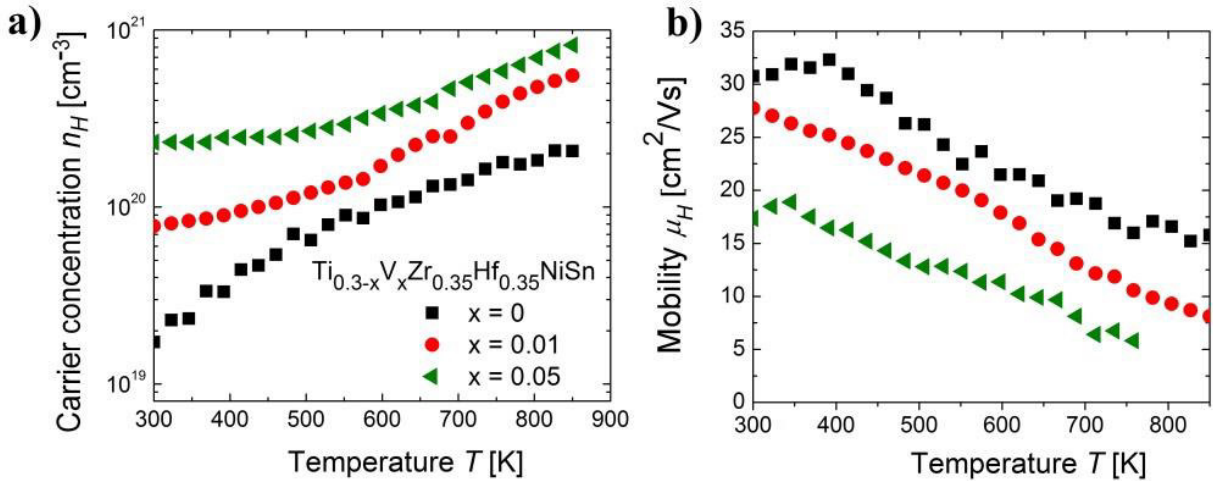


**Figure 38** Hall measurements of  $\text{Ti}_{0.3-x}\text{V}_x\text{Zr}_{0.35}\text{Hf}_{0.35}\text{NiSn}$  ( $x = 0, 0.01$  and  $0.05$ ) samples. a) Hall carrier concentration  $n_H$  and b) Hall mobility  $\mu_H$  from 300 to 900 K.

The figure of merit, shown in Figure 39, is increased with  $x = 0.01$  and  $0.03$ , as both the electronic and thermal TE properties in this samples can be improved. The maximum  $zT$  value of 1 at 773 K was obtained with 1% V concentration. The of the 5% V sample reveals almost no change in the TE performance due to the declining thermopower and high thermal conductivity caused by V inclusions.

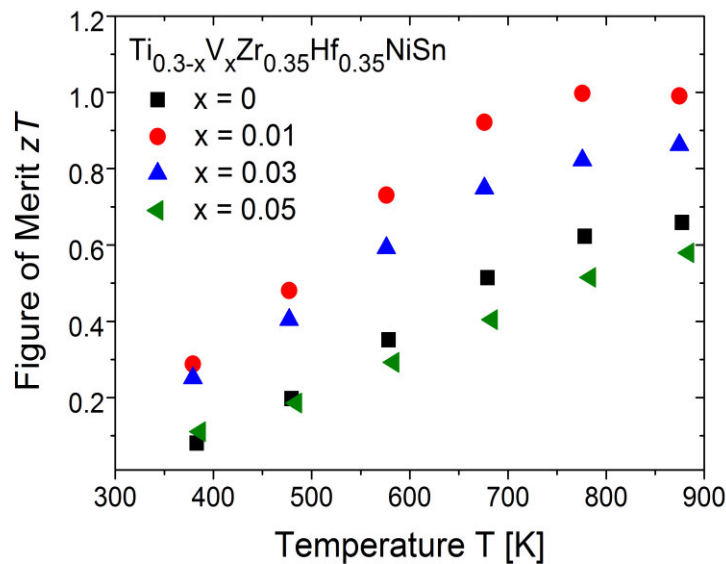


**Figure 39** Temperature dependence of the figure of merit  $zT(T)$  in  $\text{Ti}_{0.3-x}\text{V}_x\text{Zr}_{0.35}\text{Hf}_{0.35}\text{NiSn}$  ( $x = 0, 0.01, 0.03$  and  $0.05$ ) samples from 300 to 900 K.

### 6.1.2 $\text{Ti}_{0.3-x}\text{Nb}_x\text{Zr}_{0.35}\text{Hf}_{0.35}\text{NiSn}$ ( $x= 0.01, 0.03$ and $0.05$ )

The electronic doping with the donor element Nb ( $4d^5$ ) on the Ti ( $3d^4$ ) position was investigated in the parent compound. The data of this section was taken from<sup>101</sup>. The crystalline structure of all samples in  $\text{Ti}_{0.3-x}\text{Nb}_x\text{Zr}_{0.35}\text{Hf}_{0.35}\text{NiSn}$  ( $x = 0, 0.01, 0.03$  and  $0.05$ ) system was verified by powder X-ray diffraction (PXRD) measurements. The obtained X-ray patterns agree with the cubic  $C1_b$  structure ( $F\bar{4}3m$ ) found in the literature<sup>40</sup>, where all samples revealed a splitting of the Bragg reflection peaks due to the coexistence of the HH 1 and HH 2 induced by the phase separation in the parent compound<sup>80,85</sup>. The lattice parameter  $a$  of the Ti-poor HH 1 phase and the Ti-rich HH 2 phase was estimated to be  $a = 6.068 \text{ \AA}$ , and  $a = 6.011 \text{ \AA}$ , respectively. With increasing Nb concentration a decrease in the lattice parameter was observed. A successful substitution of Ti (144 pm) by Nb (143 pm) would exhibit no significant change in the unit cell since the radii of Ti and Nb are very similar. Thus, the decrease in the lattice constant results from the decreased Ti content in the HH system. *Muta et al* examined the impact of Nb substitution on the TE properties of  $X\text{NiSn}$  ( $X = \text{Ti}$  and  $\text{Zr}$ )<sup>83</sup>. However, the influence of Nb substitution on the lattice constant was not discussed.

Besides the intrinsic phase separation into the HH 1 and HH 2 phase, electron microscopy investigations revealed small Nb metallic inclusions in all Nb samples. Since Nb has the highest melting point ( $\sim 2740 \text{ K}$ ) of all elements within the compound, the existence of Nb inclusions shows that Nb was not completely substituted into the Ti lattice substitution. In order to emphasize the presence of Nb, the samples were etched with a  $\text{HCl}:\text{HNO}_3:\text{HF}:\text{H}_2\text{O}$  solution as shown in Figure 40.

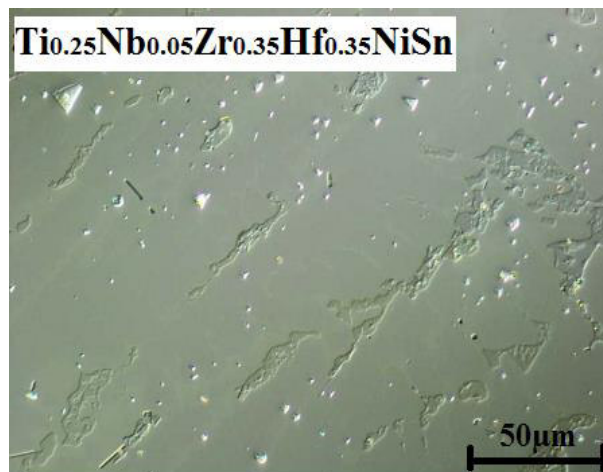


**Figure 40:** Light microscope image of the  $\text{Ti}_{0.25}\text{Nb}_{0.05}\text{Zr}_{0.35}\text{Hf}_{0.35}\text{NiSn}$  sample etched with a  $\text{HCl}:\text{HNO}_3:\text{HF}:\text{H}_2\text{O}$  solution to emphasize the metallic Nb inclusions.

The TE properties of the  $\text{Ti}_{0.3-x}\text{Nb}_x\text{Zr}_{0.35}\text{Hf}_{0.35}\text{NiSn}$  ( $x = 0, 0.01, 0.03$  and  $0.05$ ) are shown in Figure 41. The parent compound,  $\text{Ti}_{0.3}\text{Zr}_{0.35}\text{Hf}_{0.35}\text{NiSn}$ , exhibited an intrinsically semiconducting behavior, as  $\sigma$  increases with temperature (Figure 41 a). The addition of Nb drastically increased the value of  $\sigma$  at room temperature and facilitated the transition from intrinsically conducting to a metal-like behavior. In comparison to the V substitution, the increase in  $\sigma$  with Nb addition is much stronger, probably caused by the metallic Nb inclusions, as  $\sigma$  of the 1% Nb sample is as high as the 4% V sample. The increase of the electrical conductivity with the addition of Nb is compensated by a systematic decrease of the room temperature Seebeck coefficient  $\alpha$  (Figure 41 b). The thermopower was negative over the whole temperature range, indicating  $n$ -type conductivity. The maximum Seebeck coefficient  $\alpha$  of  $-240 \mu\text{V/K}$  was achieved for the parent compound  $\text{Ti}_{0.3}\text{Zr}_{0.35}\text{Hf}_{0.35}\text{NiSn}$ . With increasing Nb concentration the maximum thermopower shifted to higher temperatures, suppressing the thermal excitation of additional carriers above the usual onset around  $600 \text{ K}^{35}$ . The electronic properties  $\alpha^2\sigma$  considerably increased owing to the Nb addition. It is remarkable that although the Nb samples show semimetallic or metallic behavior, large thermopowers are attained. The power factors, shown in Figure 41 c, reveal the greatest enhancement at the moderate temperature range (300-500 K). The highest power factor of  $3.25 \cdot 10^{-3} \text{ W/K}^2\text{m}$  at  $773 \text{ K}$  was observed in the sample with 5% Nb content. According to the Wiedeman-Franz law, the thermal conductivity  $\kappa$  increased with greater Nb concentration, basically caused by the distinct increase of the electronic thermal conductivity of  $\kappa_e$  induced by the metal inclusions observed in the system. Since Nb is not substituted into the Ti lattice the effect of disorder scattering is diminished in the Nb samples. The influence of bipolar conduction, which is derived from the thermal excitation of minority carriers, can be observed in the parent  $\text{Ti}_{0.3}\text{Zr}_{0.35}\text{Hf}_{0.35}\text{NiSn}$  compound and with 1 % Nb addition (Figure 41 d).

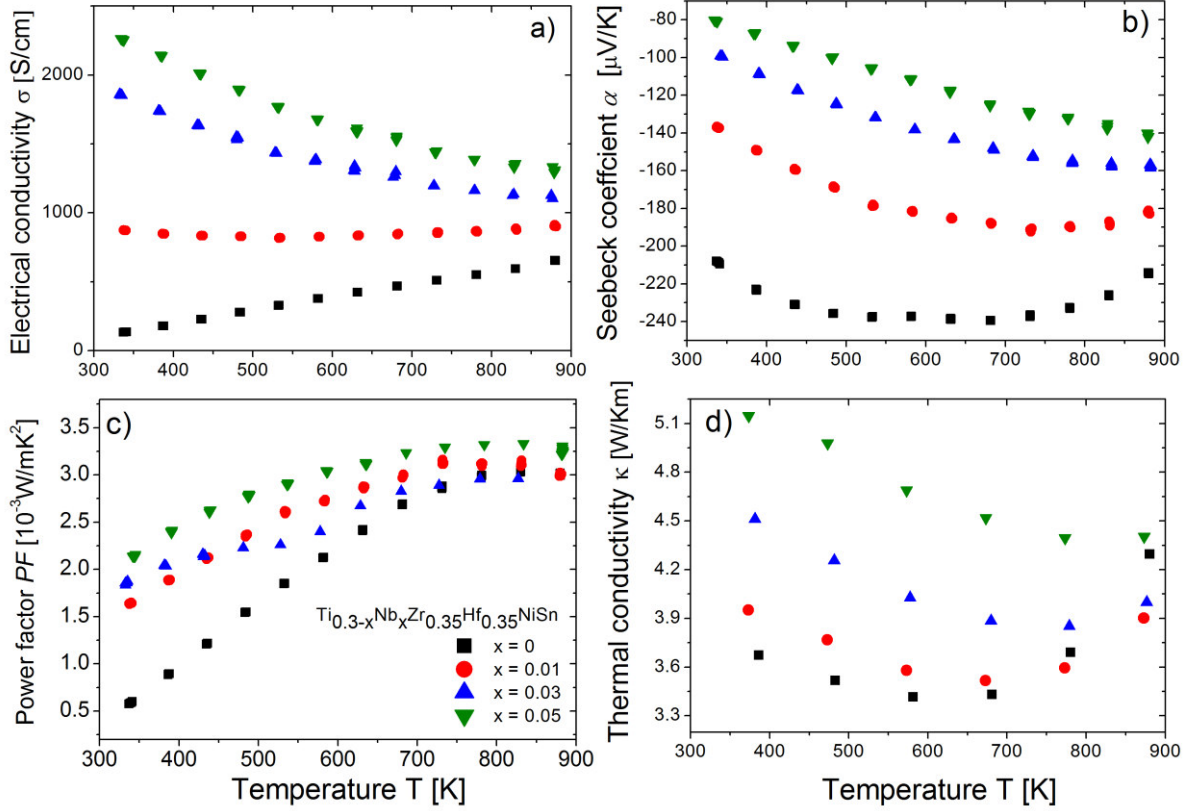


**Figure 41** Temperature dependence of the a) electrical resistivity  $\rho(T)$ , b) Seebeck coefficient  $\alpha(T)$ , c) Power factor  $\alpha^2\sigma(T)$  and d) thermal conductivity  $\kappa(T)$  figure of merit  $zT(T)$  in  $\text{Ti}_{0.3-x}\text{Nb}_x\text{Zr}_{0.35}\text{Hf}_{0.35}\text{NiSn}$  ( $x = 0, 0.01, 0.03$  and  $0.05$ ) samples from 300 to 900 K.

The Hall measurements were performed by J. Schmitt at the California Institute of Technology (CalTech). The Hall carrier concentration of the  $\text{Ti}_{0.3-x}\text{Nb}_x\text{Zr}_{0.35}\text{Hf}_{0.35}\text{NiSn}$  system ( $x = 0, 0.01, 0.03$  and  $0.05$ ) increased significantly with increasing Nb content, and once the slope of the carrier density began to flatten for  $x = 0.03$  and  $0.05$  no intrinsic excitation occurred at high temperatures (Figure 42 a). This emphasized the shift of the Fermi energy deep into the conduction band and thus the effective suppression of minority carriers due to Nb addition. The Hall mobility,  $\mu_H$  (Figure 42 b) decreased with increasing Nb concentration, due to strong scattering of the charge carriers in the system. Since the variation in  $\mu_H$  is in good agreement with the  $\mu \propto T^{-1.5}$ , the major scattering mechanisms here can also be consider to be alloy scattering<sup>94</sup>.

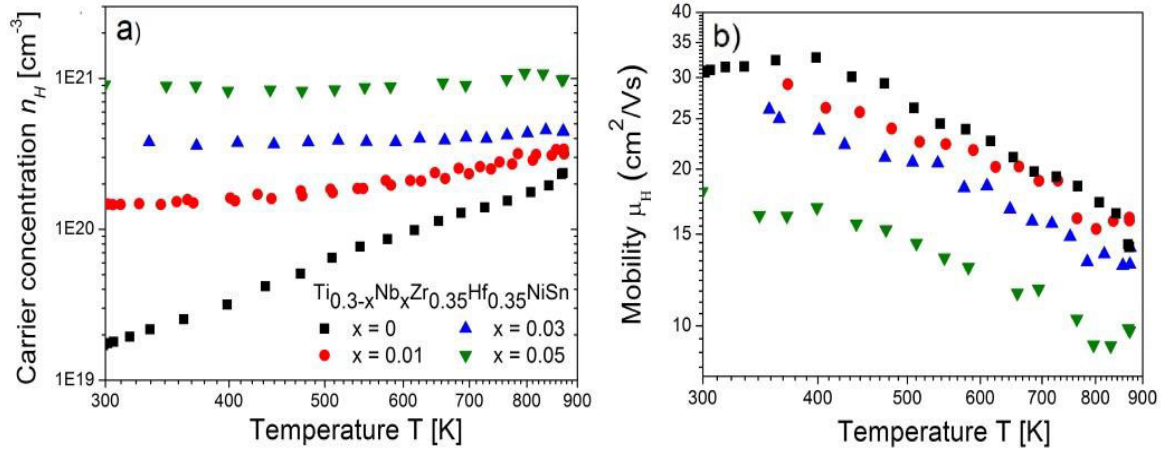


**Figure 42: Temperature dependence of a) the Hall carrier concentration  $n_H$  and b) the Hall mobility  $\mu_H$  in  $\text{Ti}_{0.3-x}\text{Nb}_x\text{Zr}_{0.35}\text{Hf}_{0.35}\text{NiSn}$  ( $x = 0, 0.01, 0.03$  and  $0.05$ ) samples from 300 to 900 K.**

The applicability of a universal transport model for phase-separated HH compounds was proven in order to estimate the optimal carrier concentration, providing a new guideline in seeking higher efficiency TE materials. The experimental transport data of  $\text{Ti}_{0.3-x}\text{Nb}_x\text{Zr}_{0.35}\text{Hf}_{0.35}\text{NiSn}$  ( $x = 0, 0.01, 0.03$  and  $0.05$ ) were analyzed using an average mass model. The calculations were performed by J. Schmitt. It was assumed that electron conduction occurs only within the conduction band for each HH phase to get a mean value for the effective mass  $m^*$ . The calculated Seebeck coefficient derived from the experimental values versus an optimized carrier concentration is given in Figure 43 a. For this evaluation we considered that the onset of the contribution of minority carriers is above 460 K, with an average effective mass value of  $m^* = 2.1 m_e$  for both phases. The agreement between the experimental results<sup>83,102</sup> and the calculation justifies the use of an average effective mass model for the estimation of the effective mass and the prediction of the optimum carrier concentration. The calculations with the average effective mass model revealed the optimal carrier concentration of 3% Nb (Figure 43 b). Hence, the application of the average effective mass model shows the possibility to predict an optimized carrier concentration with a theoretical approach.

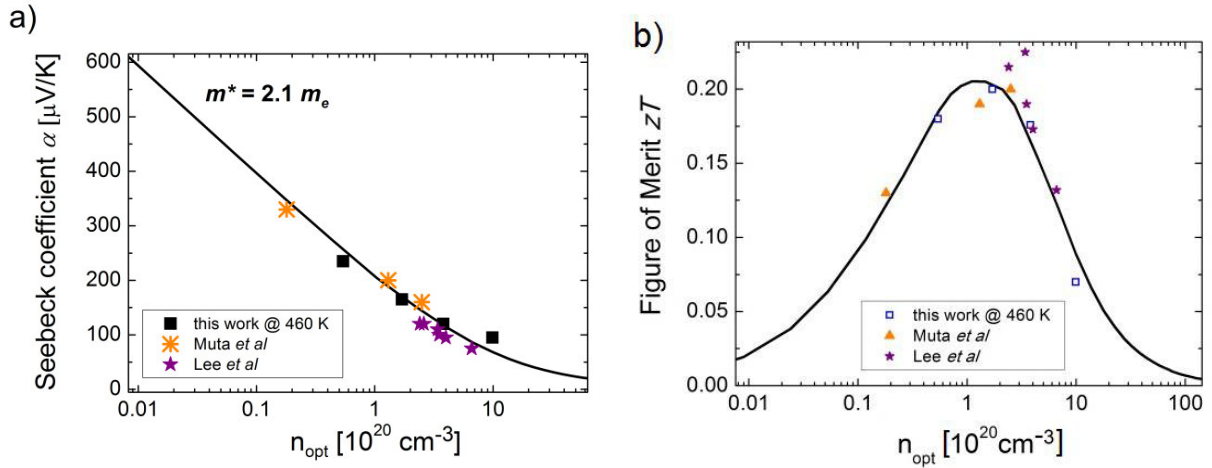


**Figure 43** a) Seebeck coefficient  $\alpha$  vs carrier concentration together with a comparison of literature data<sup>83,102</sup> and b) the average mass model (solid line) to estimate the optimized carrier concentration for the  $\text{Ti}_{0.3-x}\text{Nb}_x\text{Zr}_{0.35}\text{Hf}_{0.35}\text{NiSn}$  system. The model is consistent in good agreement with values taken from<sup>83,102</sup>.

The estimation of the  $zT$  from the measured TE properties is shown in Figure 44, indicating the highest  $zT$  value of 0.78 at 873 K for the 5% Nb sample. However, compared to the parent compound, only a minor effect could be achieved on the improvement of  $zT$  with Nb addition, basically because of the high thermal conductivities due to the metallic inclusions.

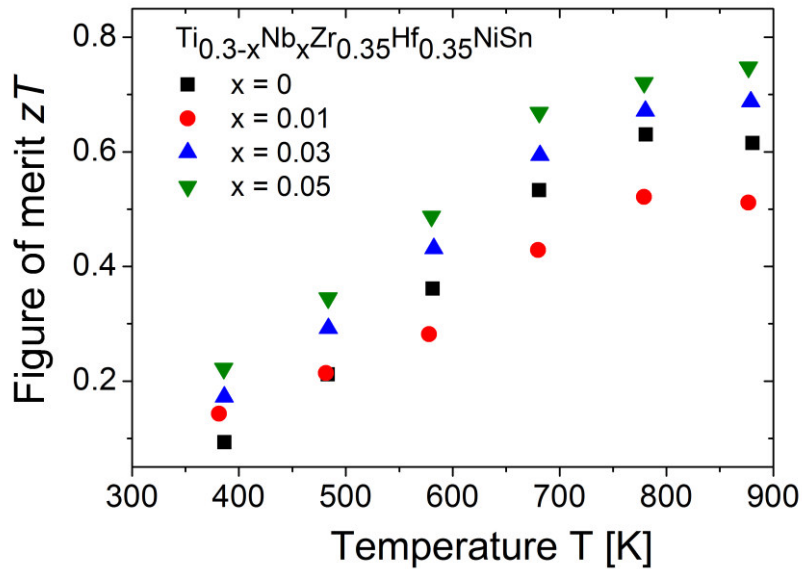


**Figure 44** Temperature dependence of the figure of merit  $zT(T)$  in  $\text{Ti}_{0.3-x}\text{Nb}_x\text{Zr}_{0.35}\text{Hf}_{0.35}\text{NiSn}$  ( $x = 0, 0.01, 0.03$  and  $0.05$ ) samples from 300 to 900 K.

### 6.1.3 $\text{Ti}_{0.3}\text{Zr}_{0.35}\text{Hf}_{0.35}\text{NiSn}_{1-x}\text{Sb}_x$ ( $x= 0.001-0.01$ )

The aforementioned results were focused on the donor dopant-induced effects at the *X*-site in the (Ti,Zr,Hf)NiSn HH system. In the following, the impact of electron doping in the Sn sublattice was examined, since electronic doping of each position in the HH structure has a different effect on the TE properties<sup>48</sup>. The *n*-type doping with Sb is well known in HH materials, and reveals yet the highest *zT* value of 1.5 at 673 K in  $\text{Ti}_{0.5}\text{Zr}_{0.25}\text{Hf}_{0.25}\text{NiSn}_{0.998}\text{Sb}_{0.002}$ . The great benefit with Sb substitution is that the DOS is not affected but the Fermi energy is shifted to higher energies. As a group-V element, Sb introduces one extra electron when substituted on the Sn position, leading to an enhancement of the electronic behavior  $\alpha^2 \sigma$ .

The *X*-ray patterns revealed the cubic  $C1_b$  structure ( $F\bar{4}3m$ ) and splitting of the Bragg reflection peaks due to the intrinsic phase separation in the parent compound in all  $\text{Ti}_{0.3}\text{Zr}_{0.35}\text{Hf}_{0.35}\text{NiSn}_{1-x}\text{Sb}_x$  ( $x = 0, 0.001, 0.002, 0.006$  and  $0.01$ ) samples. The substitution of minute amounts of Sb has no obvious effect on the lattice parameter, thus the lattice constant *a* of the Ti-poor HH 1 phase and the Ti-rich HH 2 phase showed no change with respect to the parent compound. SEM investigations exhibited the expected intrinsic phase separation (Figure 45). To ensure the accurate stoichiometry of the Sb in the compound the samples were prepared using the conventional cold pressing sintering approach. The elements were ball milled and cold-pressed, following by a sintering via arc melting. Despite the modified preparation method the dendritic microstructure did not change compared to the parent compound. It should be considered that arc melting could lead to an off-stoichiometry in the compounds due to evaporation of Sb.

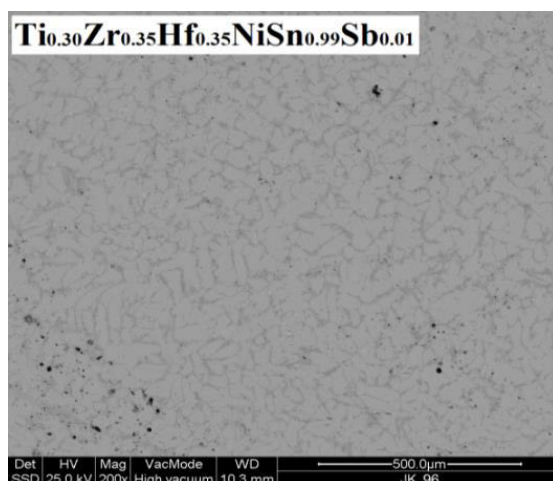
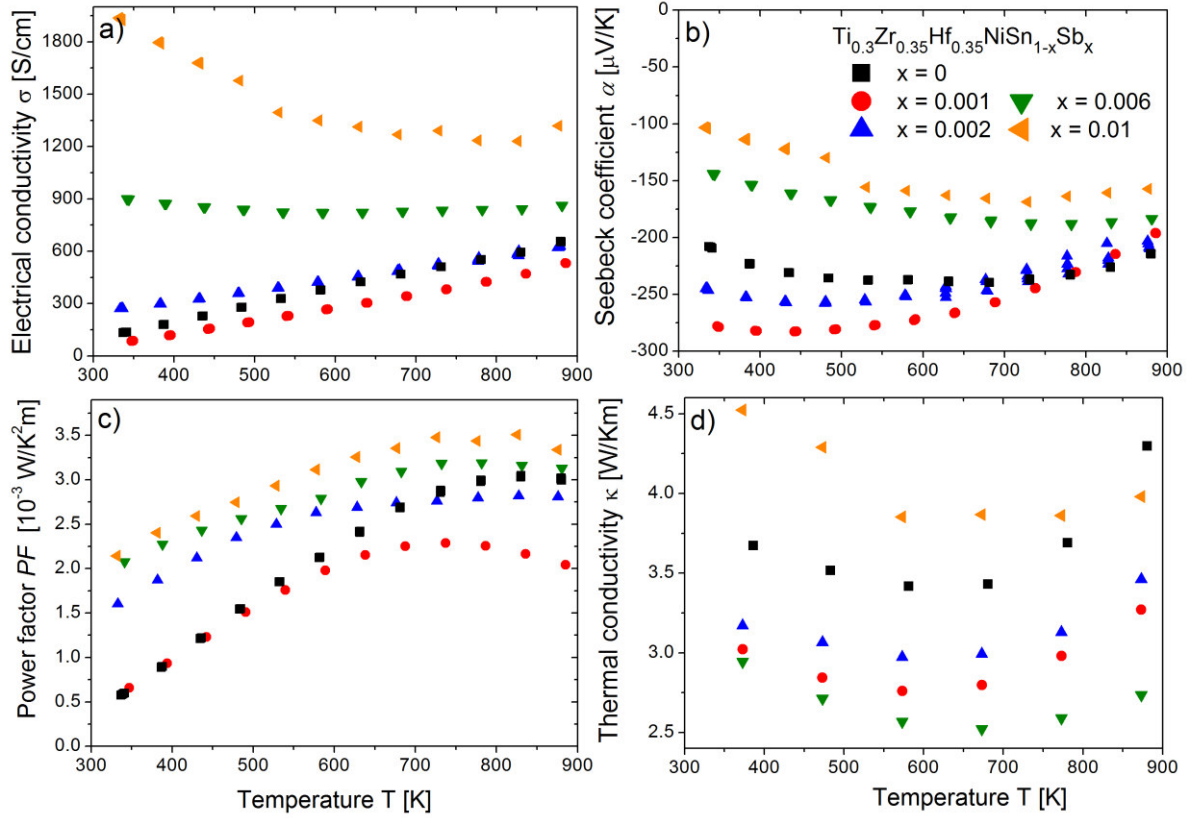


Figure 45 SEM (BSE) image of  $\text{Ti}_{0.3}\text{Zr}_{0.35}\text{Hf}_{0.35}\text{NiSn}_{0.99}\text{Sb}_{0.01}$  sample.



The TE properties of the  $\text{Ti}_{0.3}\text{Zr}_{0.35}\text{Hf}_{0.35}\text{NiSn}_{1-x}\text{Sb}_x$  ( $x = 0, 0.001, 0.002, 0.006$  and  $0.01$ ) are shown in Figure 46. The electrical conductivity  $\sigma$  exhibited a semiconductor-metal transition with increasing Sb substitution (Figure 46 a). The temperature dependence of the  $x = 0.01$  sample showed entirely metallic behavior. This is in a good agreement with previously reported studies of Sb-doping in HH compounds<sup>73,74</sup>. The thermopower  $\alpha$  revealed negative values over the whole temperature range for all samples and followed the opposite trend of  $\sigma$ . The distinct increase of  $\alpha$  at 373 K for  $x = 0.001$  and  $0.002$  corresponds to the shift of the chemical potential due to the electron doping (Figure 46 b). With increasing Sb concentration and the change from the semiconducting to metallic or the semimetallic regime of conduction, the thermopower is diminished and shifts the maximum of  $\alpha$  to higher temperature, as could be seen in the V and Nb samples. The donor-induced enhancement of the electronic properties  $\alpha^2\sigma$  can be observed with increasing Sb substitution. The power factor  $\alpha^2\sigma$  was evaluated from the experimental results, exhibiting a maximum value of  $PF$  of  $3.5 \cdot 10^{-3} \text{W/K}^2\text{m}$  at 823 K with  $x = 0.01$  Sb content (Figure 46 c). In comparison to the Nb substitution, Sb led almost to the same enhancement of the electronic properties. The site substitution with Sb into the Sn lattice caused a significant reduction of the thermal conductivity  $\kappa$  with higher Sb concentrations (Figure 46 d), owing to higher contributions of alloy scattering. The metallic behavior of the  $x = 0.01$  Sb sample, showed the highest  $\kappa$  resulting from the distinct increase of the electronic thermal conductivity of  $\kappa_e$  in accordance to the Wiedeman-Franz law.



**Figure 46** Temperature dependence of the a) electrical resistivity  $\rho(T)$ , b) Seebeck coefficient  $\alpha(T)$ , c) Power factor  $\alpha^2\sigma(T)$  and d) thermal conductivity  $\kappa(T)$  in  $\text{Ti}_{0.3}\text{Zr}_{0.35}\text{Hf}_{0.35}\text{NiSn}_{1-x}\text{Sb}_x$  ( $x = 0, 0.001, 0.002, 0.006$  and  $0.01$ ) samples from 300 to 900 K.

The temperature dependence of the figure of merit  $zT$  is presented in Figure 47. Owing to the reduction of the thermal conductivity and the optimization of the electronic properties the TE performance is improved with Sb substitution at all temperatures. The highest  $zT$  of 0.97 at 873 K was attained with  $x = 0.006$  Sb. The physical properties in the parent  $n$ -type  $\text{Ti}_{0.3}\text{Zr}_{0.35}\text{Hf}_{0.35}\text{NiSn}$  HH system are very sensitive to a particular structural arrangement, and any kind of disorder has a strong influence on the transport behavior. Thus the Z-site seems to be more sensitive to electronic doping than the X-site, since marginal concentration of Sb leads such an improvement in the TE properties<sup>68,85</sup>.

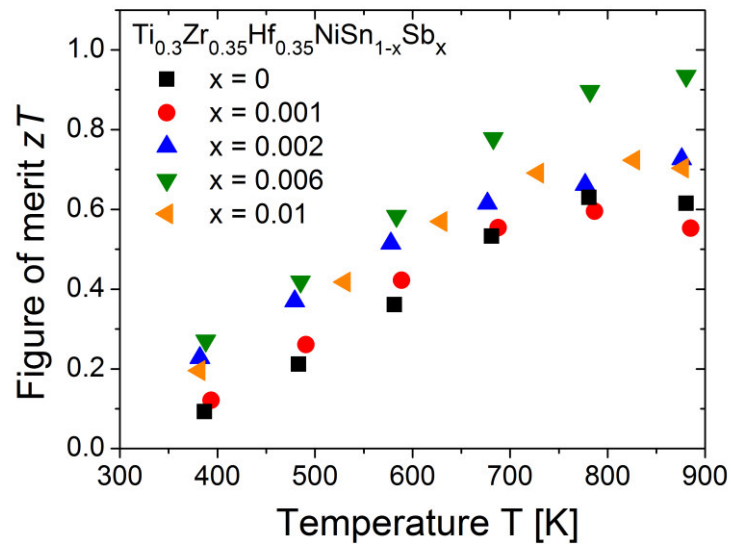


**Figure 47** Temperature dependence of the figure of merit  $zT(T)$  in  $\text{Ti}_{0.3}\text{Zr}_{0.35}\text{Hf}_{0.35}\text{NiSn}_{1-x}\text{Sb}_x$  ( $x = 0, 0.001, 0.002, 0.006$  and  $0.01$ ) samples from 300 to 900 K.

## 6.2 Acceptor dopant-induced properties of $\text{Ti}_{0.3}\text{Zr}_{0.35}\text{Hf}_{0.35}\text{NiSn}$

### 6.2.1 $\text{Ti}_{0.3-x}\text{Sc}_x\text{Zr}_{0.35}\text{Hf}_{0.35}\text{NiSn}$ ( $x = 0.01-0.05$ )

The acceptor-induced change in the *n*-type  $\text{Ti}_{0.3}\text{Zr}_{0.35}\text{Hf}_{0.35}\text{NiSn}$  HH was proven via site substitution with Sc ( $3d^3$ ) on the Ti ( $3d^4$ ) sublattice. The X-ray patterns in all  $\text{Ti}_{0.3-x}\text{Sc}_x\text{Zr}_{0.35}\text{Hf}_{0.35}\text{NiSn}$  ( $x = 0 - 0.05$ ) samples exhibited the cubic  $C1_b$  structure ( $F\bar{4}3m$ ) and splitting of the Bragg reflection peaks as a result of the coexistence of two HH phases. Owing to the larger radius of Sc (Ti 140 pm, Sc 160 pm), the lattice constant increased with increasing Sc substitution, indicating the Sc substitution into the Ti lattice. PXRD and EPMA measurements revealed small amounts of Sn impurities in all samples. Figure 48 exemplifies the intrinsic phase separation found in all samples with Sc substitution.

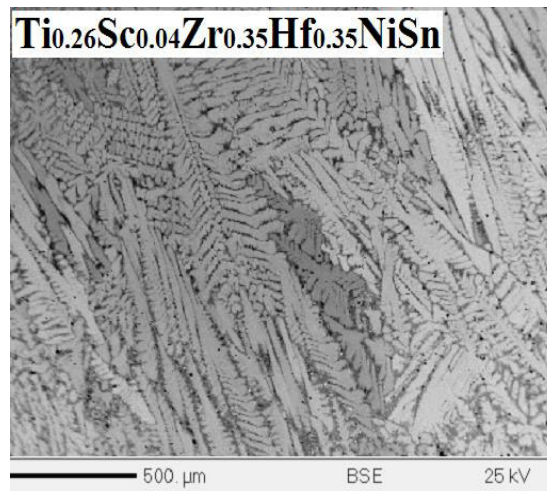


**Figure 48 SEM (BSE) image of  $\text{Ti}_{0.26}\text{Sc}_{0.04}\text{Zr}_{0.35}\text{Hf}_{0.35}\text{NiSn}$  sample.**

Hall measurements of  $\text{Ti}_{0.3-x}\text{Sc}_x\text{Zr}_{0.35}\text{Hf}_{0.35}\text{NiSn}$  ( $x = 0-0.05$ ) are illustrated in Figure 49. To understand the sophisticated transport properties of *p*-type HH materials, first the Hall measurements are discussed before taking a look on the TE properties of the Sc-doped samples. The Hall measurements were performed by J. Schmitt at the California Institute of Technology (CalTech). For lower Sc doping levels the temperature dependence of the carrier concentration  $n_H$  is increased, but revealed *n*-type conduction, since these doping levels are not able to compensate the number of existing electrons (Figure 49 a). Owing to the mixed conduction for the  $0 \leq x \leq 0.03$  Sc content samples, only the higher mobile electrons are detected. As a result, the samples still reveal *n*-type conductivity, despite the change in the sign of the Seebeck coefficient (Figure 50 b). With 4% and 5% Sc concentration the transport

is entirely dominated by holes, since these doping levels are able to compensate the strong intrinsic  $n$ -type conduction. The temperature dependence of the Hall mobility  $\mu_H$  is shown in Figure 49 b. The carrier mobility depends on the band effective mass  $m^*$  and the relaxation time  $\tau$  roughly as  $\mu = \frac{e\tau}{m^*}^{103}$ . Based on *ab initio* calculations, a high  $\mu_H$  value for the  $n$ -type  $\text{Ti}_{0.3}\text{Zr}_{0.35}\text{Hf}_{0.35}\text{NiSn}$  is expected due to their light conduction band. The valence band, however, has been shown to have a higher effective mass; so by substituting Ti with Sc one might expect generally lower  $\mu_H$  values for  $p$ -type materials as the Fermi energy is shifted into the valence band. This is consistent with the experimental results shown in Figure 49 b, where the mobilities of the heavily Sc doped samples are much lower in magnitude than the parent compound.

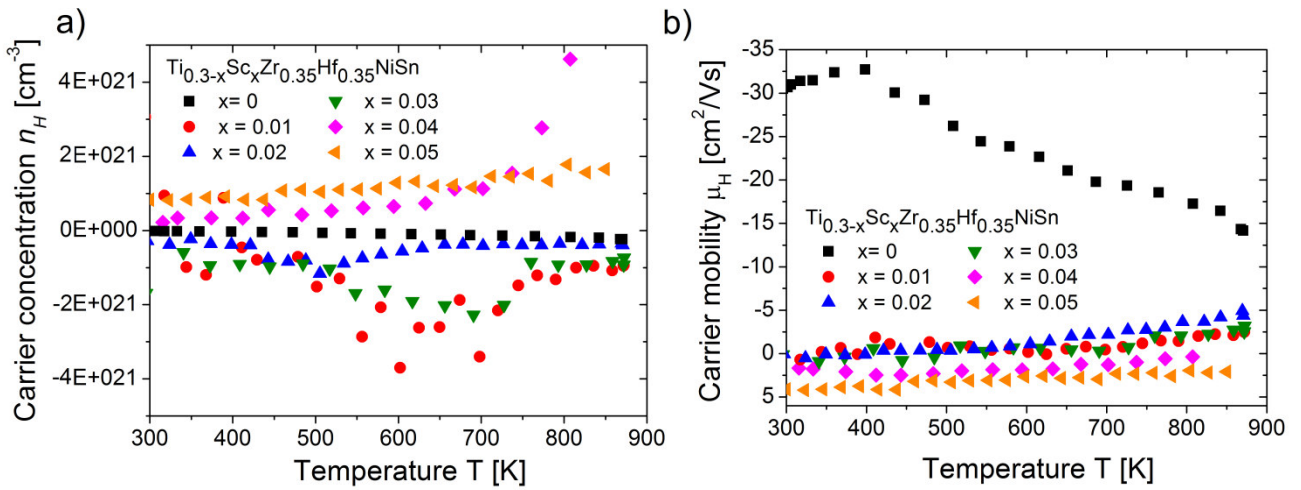


**Figure 49** Hall measurements of  $\text{Ti}_{0.3-x}\text{Sc}_x\text{Zr}_{0.35}\text{Hf}_{0.35}\text{NiSn}$  ( $x = 0-0.05$ ) samples. a) Hall carrier concentration  $n_H$  and b) Hall mobility  $\mu_H$  from 300 to 900 K.

The TE properties of  $\text{Ti}_{0.3-x}\text{Sc}_x\text{Zr}_{0.35}\text{Hf}_{0.35}\text{NiSn}$  ( $x = 0-0.05$ ) are presented in Figure 50. The temperature dependence of the electrical conductivity  $\sigma$  revealed semiconducting behavior, as  $\sigma$  increased with rising temperatures (Figure 50 a). Compared to the electronic doping with donor elements discussed before, hole doping with Sc exhibited much lower  $\sigma$  values ( $\sigma < 500$  S/cm). According to Equation (10),  $\sigma = ne\mu$ , the reduced  $\sigma$  is caused by the diminished mobility in  $p$ -type HH materials, resulting from the contribution of mixed carriers. The parent  $\text{Ti}_{0.3}\text{Zr}_{0.35}\text{Hf}_{0.35}\text{NiSn}$  compound displayed a large negative Seebeck coefficient  $\alpha$ , indicating  $n$ -type behavior at all temperatures (Figure 50 b). At room temperature all Sc-based samples revealed positive values of  $\alpha$ , pointing to the shift of the Fermi energy into the valence band and thus the change of the transport properties from  $n$ - to  $p$ -type conduction. For low substitution levels ( $0.01 \leq x \leq 0.03$ ) the magnitude of  $\alpha$  declined with temperature, since

the maximum thermopower is reached below room temperature. As observed in the Hall measurements (Figure 49) two types of carriers contribute to the transport properties and are responsible for the decrease in the Seebeck coefficient at high temperatures. With 4% and 5% Sc substitution  $\alpha$  is positive over the whole temperature range from 300 to 900 K, indicating that holes are the majority carriers. The maximum Seebeck coefficient of  $\alpha \sim 210 \mu\text{V/K}$  at 600 K was attained with 4% Sc content, which is the highest reported value for a  $p$ -type material based on a (Ti,Zr,Hf)NiSn system<sup>71</sup>. Note that the HH  $\text{Ti}_{0.3}\text{Zr}_{0.35}\text{Hf}_{0.35}\text{NiSn}$  and  $\text{Ti}_{0.26}\text{Sc}_{0.04}\text{Zr}_{0.35}\text{Hf}_{0.35}\text{NiSn}$  compounds revealed equally high  $\alpha$  values, which persist over a broad temperature range and guarantee high TE performance in a wide temperature regime. The decrease in  $\alpha$  above 600 K emerged from the onset of minority carrier activation. The Power factor  $PF$  evaluated from the experimental data, attained its highest value of  $1.5 \cdot 10^{-3} \text{W/K}^2\text{m}$  at 700 K with 4% Sc concentration (Figure 50 c), which is only half of the  $n$ -type value, resulting from the diminished electrical conductivity in the  $p$ -type samples. The thermal conductivity  $\kappa$  can be further reduced in the  $p$ -type samples (Figure 50 d), owing to higher phonon scattering due to the increased disorder in the HH structure. The decrease in  $\kappa$  for temperatures  $> 600$  K is caused by the increasing number of carriers excited into the valence band.

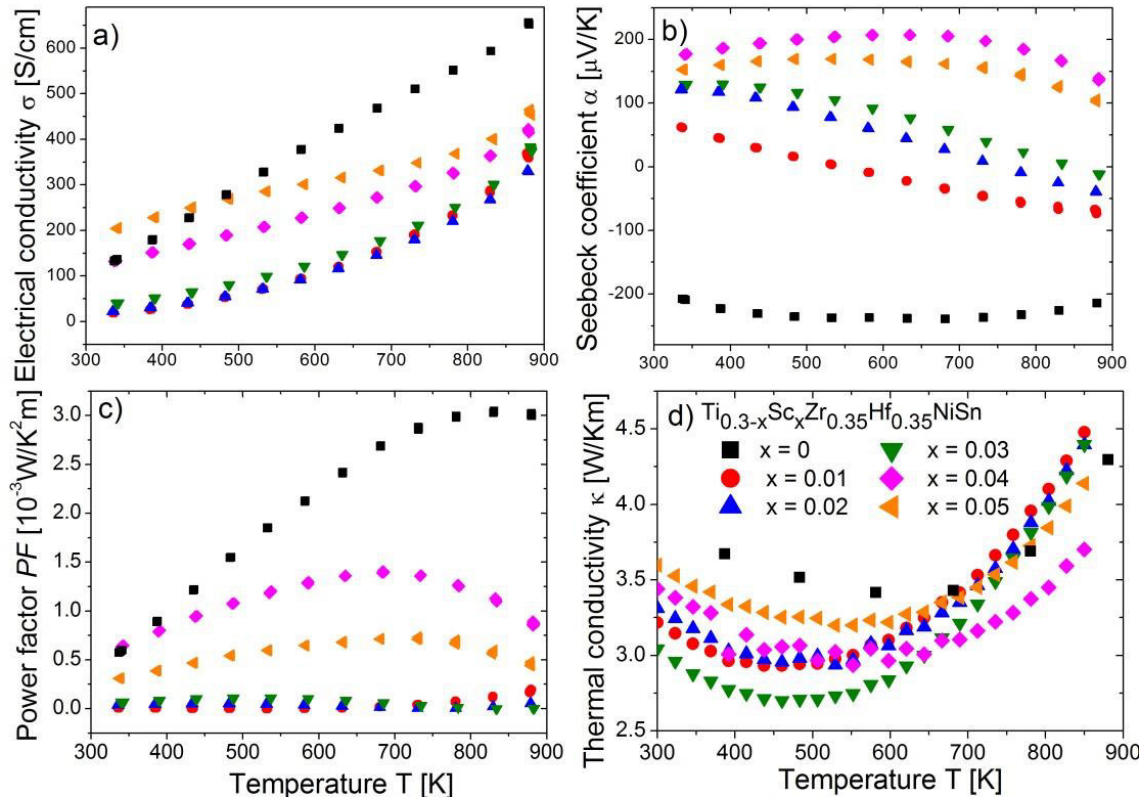


**Figure 50** Temperature dependence of a) electrical conductivity  $\sigma(T)$ , b) Seebeck coefficient  $\alpha(T)$ , c) Power factor  $\alpha^2 \sigma(T)$  and d) thermal conductivity  $\kappa(T)$  in  $\text{Ti}_{0.3-x}\text{Sc}_x\text{Zr}_{0.35}\text{Hf}_{0.35}\text{NiSn}$  ( $x = 0-0.05$ ) samples from 300 to 900 K.

The estimation of the  $zT$  from the measured TE properties is displayed in Figure 51, showing the highest  $zT$  value of 0.3 at 673 K with 4% Sc concentration, which is the highest reported  $zT$  for a  $p$ -type material based on the  $MNiSn$  system in this temperature range. Compared to the parent  $Ti_{0.3}Zr_{0.35}Hf_{0.35}NiSn$  compound, with a maximum  $zT$  of 0.65 at 773 K, all  $p$ -type materials are less sufficient in their TE efficiency, due to the contribution of mixed carriers in the  $MNiSn$  system.

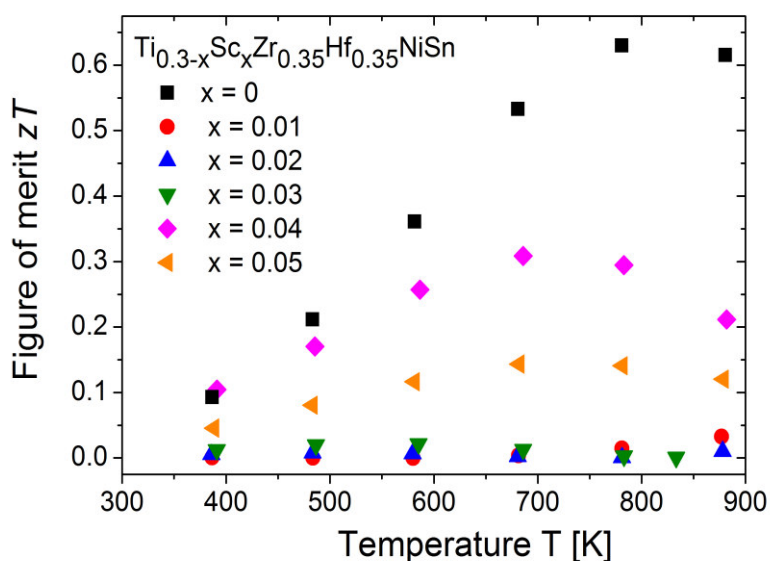
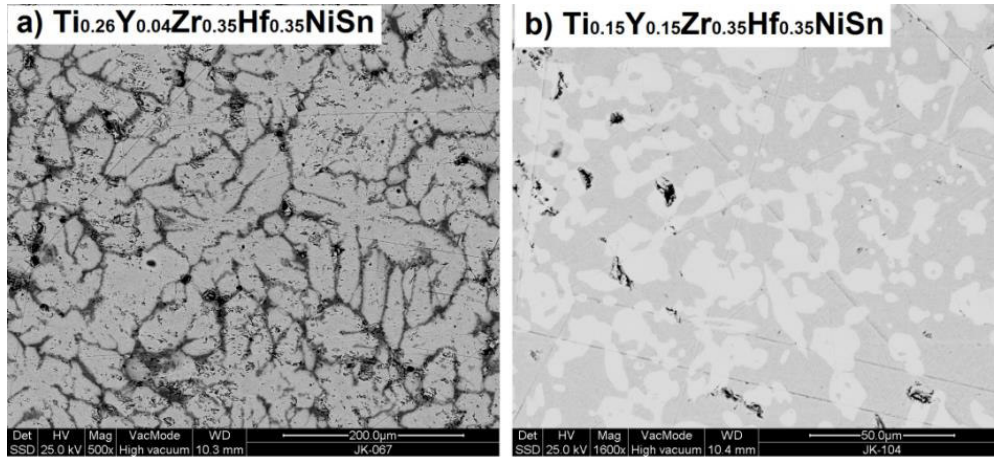


Figure 51 Temperature dependence of the figure of merit  $zT(T)$  of  $Ti_{0.3-x}Sc_xZr_{0.35}Hf_{0.35}NiSn$  ( $x = 0-0.05$ ) samples from 300 to 900 K.

### 6.2.2 $Ti_{0.3-x}Y_xZr_{0.35}Hf_{0.35}NiSn$ ( $x = 0.01-0.20$ )

The influence of Y ( $4d^3$ ) as an acceptor dopant in the  $n$ -type  $Ti_{0.3}Zr_{0.35}Hf_{0.35}NiSn$  HH system was examined. The crystalline structure of all samples in  $Ti_{0.3-x}Y_xZr_{0.35}Hf_{0.35}NiSn$  ( $x = 0, 0.04, 0.07, 0.15$  and  $0.20$ ) exhibited the cubic  $C1_b$  structure ( $F\bar{4}3m$ ) and reflex splitting, due to the intrinsic phase separation. The lattice parameter increased in all samples with Y addition, pointing the substitution of the larger sized Y (178 pm) in the Ti sublattice for  $x \leq 0.07$ . With higher Y concentration, phase impurities such as  $(Zr,Hf)_5Sn_3$  and  $Ni_2Y_3$  were observed, which probably caused the increase in the unit cell. EMPA of the samples revealed the typical eutectic microstructure for  $0 \leq x \leq 0.07$  (Figure 52 a). Consistent with the PXRD measurement, Y-based impurity phases were found for  $x \geq 0.15$ , leading to a change of the dendritic phase separation (Figure 52 b).



**Figure 52** SEM (BSE) images of a)  $\text{Ti}_{0.26}\text{Y}_{0.04}\text{Zr}_{0.35}\text{Hf}_{0.35}\text{NiSn}$  and b)  $\text{Ti}_{0.15}\text{Y}_{0.15}\text{Zr}_{0.35}\text{Hf}_{0.35}\text{NiSn}$  samples.

The TE properties of  $\text{Ti}_{0.3-x}\text{Y}_x\text{Zr}_{0.35}\text{Hf}_{0.35}\text{NiSn}$  ( $x = 0, 0.04, 0.07, 0.15$  and  $0.20$ ) were investigated from 300-900 K and are shown in Figure 53. The temperature dependence of the electrical conductivity  $\sigma$  revealed semiconducting behavior over the whole temperature range (Figure 53 a), also showing here the lower values in  $\sigma$  due to bipolar contribution. The Seebeck coefficient  $\alpha$  of the parent compound and the  $x = 0.20$  Y sample revealed  $n$ -type conduction (Figure 53 b); in the Y-based sample the observed impurities might affect the transport properties. It can be seen from the change in the sign of  $\alpha$  from negative to positive, that holes become dominant for samples containing  $x \geq 0.07$  Y at room temperature. The maximum in  $\alpha$  is shifted to higher temperatures with increasing Y concentration, indicating a shift of the Fermi energy into the valence band. The maximum value in  $\alpha$  of  $50 \mu\text{V/K}$  is attained with 15% Y, which is much lower compared to the Sc substitution ( $\alpha > 200 \mu\text{V/K}$ ). The strong decline in the thermopower at higher temperatures resulted from higher quantities of carriers caused by thermal excitation and the adverse effect of impurity phases. The Power factors  $PF$  exhibit poor electronic properties of the Y-based samples, owing to the diminished electrical conductivity and small Seebeck coefficient values (Figure 53 c). The temperature dependence of the thermal conductivity  $\kappa$  showed a reduction in its values at 373 K with increasing Y substitution (Figure 53 d), resulting from higher contributions to phonon scattering at point defects and impurities. The impact of mixed carriers caused the increase in  $\kappa$  above 600 K.



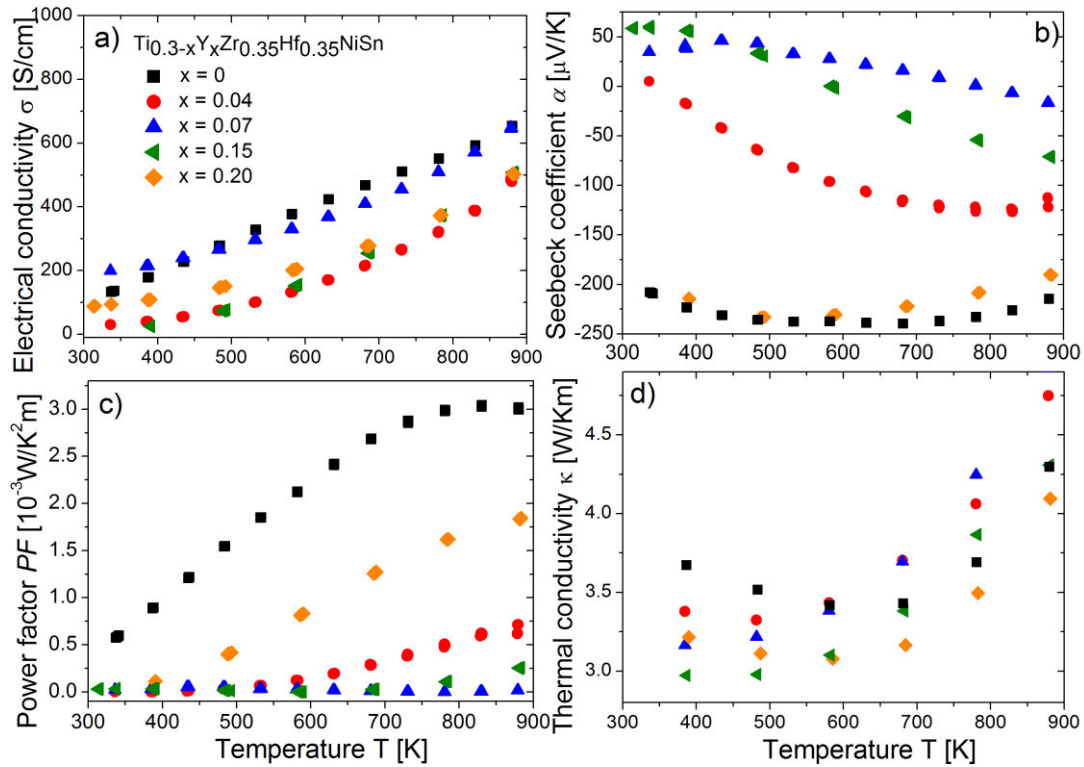


**Figure 53** Temperature dependence of the a) electrical conductivity  $\sigma(T)$ , b) Seebeck coefficient  $\alpha(T)$ , c) Power factor  $\alpha^2\sigma(T)$  and d) thermal conductivity  $\kappa(T)$  in  $\text{Ti}_{0.3-x}\text{Y}_x\text{Zr}_{0.35}\text{Hf}_{0.35}\text{NiSn}$  ( $x = 0-0.20$ ) samples from 300 to 900K.

The figure of merit  $zT$  as a function of the temperature is shown in Figure 54. The highest  $zT$  value of 0.4 at 873 K was attained with 20% Y, which unfortunately exhibited  $n$ -type conductivity (Figure 53 b). In comparison to the site substitution with Sc ( $zT = 0.3$  at 673 K), hole doping reveals poor TE performance and thus is less suitable as  $p$ -type material.

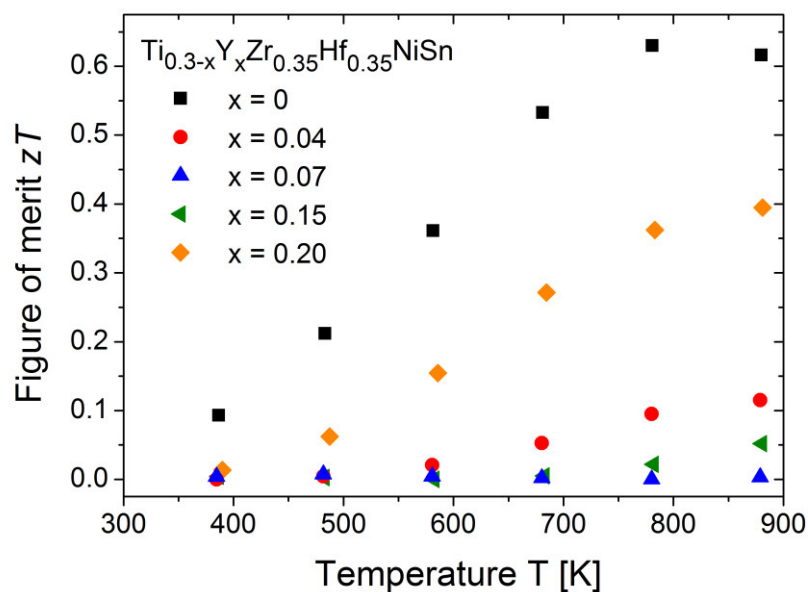


**Figure 54** Temperature dependence of the figure of merit  $zT(T)$  of  $\text{Ti}_{0.3-x}\text{Y}_x\text{Zr}_{0.35}\text{Hf}_{0.35}\text{NiSn}$  ( $x = 0-0.20$ ) samples from 300 to 900 K.

### 6.2.3 $\text{Ti}_{0.3}\text{Zr}_{0.35}\text{Hf}_{0.35}\text{Ni}_{1-y}\text{Co}_y\text{Sn}$ ( $x= 0.01-0.1$ )

The acceptor-induced effect of Co ( $3d^9$ ) substitution on the Ni ( $3d^{10}$ ) sublattice was investigated in the *n*-type  $\text{Ti}_{0.3}\text{Zr}_{0.35}\text{Hf}_{0.35}\text{NiSn}$  compound. The crystalline structure of all  $\text{Ti}_{0.3}\text{Zr}_{0.35}\text{Hf}_{0.35}\text{Ni}_{1-x}\text{Co}_x\text{Sn}$  ( $x = 0, 0.04, 0.07$  and  $0.10$ ) samples revealed the cubic  $C1_b$  structure and the splitting of the Bragg reflexes, owing to the intrinsic phase separation. The lattice parameter did not change with Co substitution, which is consistent with the theory, since the atomic radii of Ni (124.6 pm) and Co (125.3 pm) are very similar. The lattice parameter  $a$  of the Ti-poor phase (HH 1) and the Ti-rich phase (HH 2) was estimated to be  $a = 6.069 \text{ \AA}$ , and  $a = 6.008 \text{ \AA}$ , respectively. EMPA measurements showed no change in the dendritic phase separation with respect to the site substitution of Ni by Co (Figure 55). Besides small Sn inclusions no other impurity phases were observed in the Co-based samples, confirming the PXRD data.

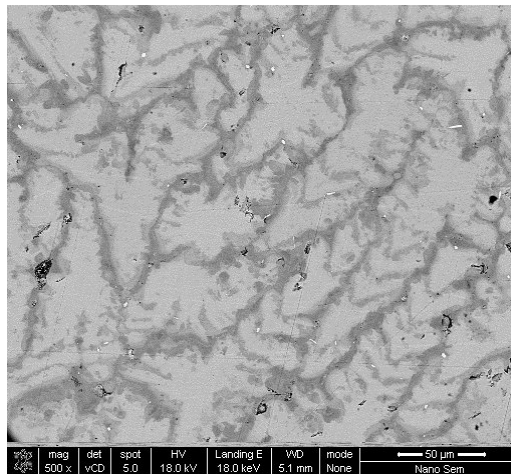
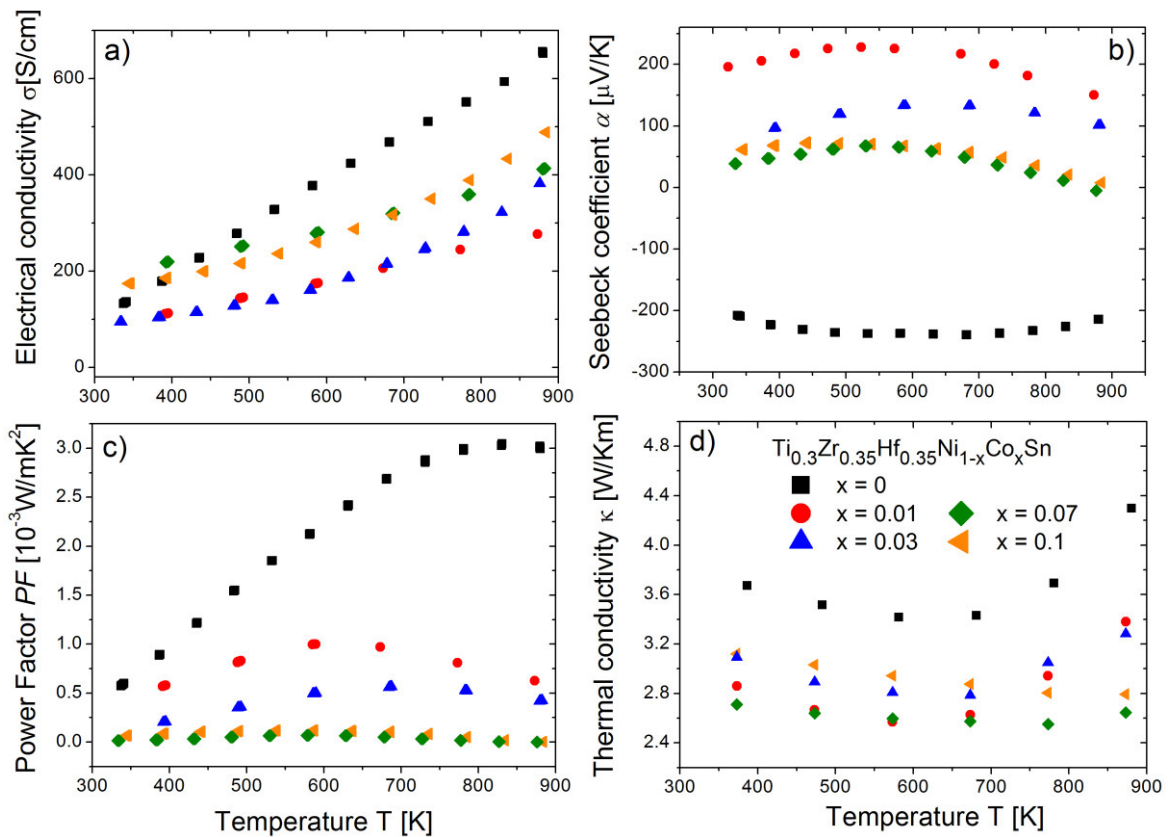


Figure 55 SEM (BSE) image of the  $\text{Ti}_{0.3}\text{Zr}_{0.35}\text{Hf}_{0.35}\text{Ni}_{0.99}\text{Co}_{0.01}\text{Sn}$  sample.

The TE properties of  $\text{Ti}_{0.3}\text{Zr}_{0.35}\text{Hf}_{0.35}\text{Ni}_{1-x}\text{Co}_x\text{Sn}$  ( $x = 0, 0.04, 0.07$  and  $0.10$ ) are shown in Figure 56. The temperature dependence of the electrical conductivity  $\sigma$  shows typical semiconducting behavior and is reduced with Co substitution, caused by the diminished mobility of the carriers in the valence band (Figure 56 a). With increasing acceptor dopant concentration,  $\sigma$  increased due to the higher quantity of carriers introduced into the HH system, but is still lower than the parent compound. The behavior of the Seebeck coefficient  $\alpha$  correlates with  $\sigma$ . As Co is substituted for Ni, the Fermi level is shifted to lower energies<sup>104</sup>, thus  $\alpha$  changes its sign from negative to positive, indicating that the transport is controlled by free holes (Figure 56 b). The intrinsic *n*-type system is overcompensated with holes with 1% Co concentration, showing the maximum  $\alpha$  value of  $230 \mu\text{V/K}$  at 573 K, which is higher than

observed with 4% Sc substitution on the Ti position. The acceptor-induced influence on the Seebeck coefficient seems to be more sensitive on the Y-site (Ni replaced by Co) than on the X-site (Ti replaced by Sc). With 3% Co the maximum of  $\alpha$  is shifted to higher temperatures, emphasizing a further shift of the Fermi level into the valence band. For temperatures  $> 600$  K,  $\alpha$  shows the typical decline due to the increased number of minority carriers caused by thermal excitation<sup>105</sup>. The power factor  $PF$  value of  $1.0 \cdot 10^{-3} \text{W/K}^2\text{m}$  at 573 K with  $x = 0.01$  is decreased by a factor of 3 compared to the parent compound (Figure 56 c). The thermal conductivity  $\kappa$  is significantly reduced by Co substitution on the Ni sublattice, resulting from higher disorder and thus stronger phonon scattering in the material.



**Figure 56** Temperature dependence of the a) electrical conductivity  $\sigma(T)$ , b) Seebeck coefficient  $\alpha(T)$ , c) Power factor  $\alpha^2\sigma(T)$  and d) thermal conductivity  $\kappa(T)$  in  $\text{Ti}_{0.3}\text{Zr}_{0.35}\text{Hf}_{0.35}\text{Ni}_{1-x}\text{Co}_x\text{Sn}$  ( $x = 0-0.10$ ) samples from 300 to 900 K.

The temperature dependence of the TE performance  $zT$  is presented in Figure 57. The maximum  $zT$  of 0.25 at 673 K is reached with 1 % Co content, which is lower than that attained when substituting 4% Sc substitution. Owing to the lower electronic properties in the Co-doped samples, the TE performance was not improved by Co substitution.

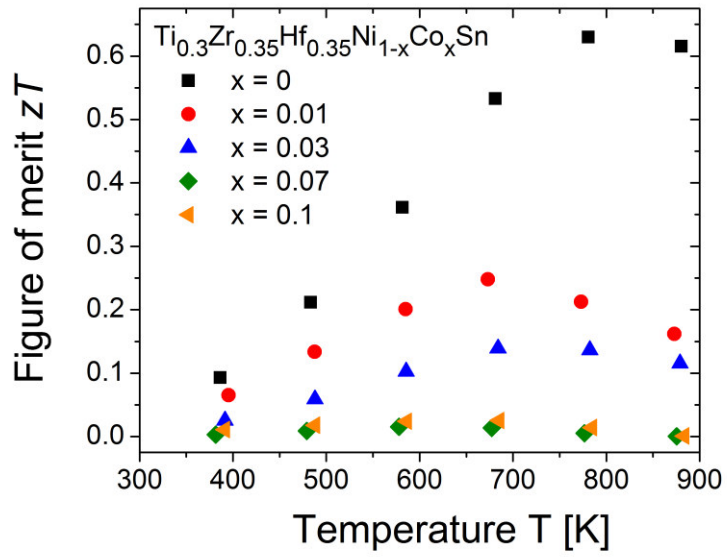


**Figure 57** Temperature dependence of the figure of merit  $zT(T)$  of the  $\text{Ti}_{0.3}\text{Zr}_{0.35}\text{Hf}_{0.35}\text{Ni}_{1-x}\text{Co}_x\text{Sn}$  ( $x = 0-0.20$ ) samples from 300 to 900 K.

## 7 Compatibility of *n*- and *p*-type HH materials

Besides the temperature dependence of the TE properties in a material, it is vital to know the influence of temperature on the material's mechanical properties, like hardness and thermal expansion. In particular for the optimal operation of TE devices, micro cracks and material deterioration must be avoided. A manufacturing method, which allows the fabrication of compatible *n*- and *p*-type TE material pairs of different dimensions, might also be important for TE engineering. For these purposes, spark plasma sintering is a suitable technique. Furthermore, the long-term stability of the TE material needs to be guaranteed under operation conditions. The investigation of the long-term efficiency of a commercially available bulk-Bi<sub>2</sub>Te<sub>3</sub> TEG with 31 thermocouples has shown a reduction of  $\alpha$  and  $\sigma$ , which was caused by material deterioration and micro cracks of the thermocouples<sup>106</sup>. This study emphasized the urgency of alternative materials for TE applications. Currently, there are no reports on the importance of the long-term stability of HH or the preservation of their TE properties through repeated heating and cooling. In regard of the mechanical properties, long-term stability and manufacturing method, the exemplary *n*-type Ti<sub>0.3</sub>Zr<sub>0.35</sub>Hf<sub>0.35</sub>NiSn and *p*-type Ti<sub>0.26</sub>Sc<sub>0.04</sub>Zr<sub>0.35</sub>Hf<sub>0.35</sub>NiSn HH compound were investigated.

### 7.1 Mechanical properties

The micro hardness was determined by hardness measurements according to Vickers. Therefore, five indentations were performed using a diamond pyramid with a force of 300 pond (1 pond = 9.8 mN) and a holding time for 10 seconds. The micro hardness of the *n*-type material and *p*-type material was found to be  $884 \pm 38$  HV and  $915 \pm 12$  HV, respectively. These HH compounds can be considered as hard and brittle materials. For comparison, the hardness of Martensite, a carbon rich steel, is about 770-1200 HV<sup>90</sup>. In general, structural disorder, such as point and dislocation defects are responsible for the high hardness in materials.

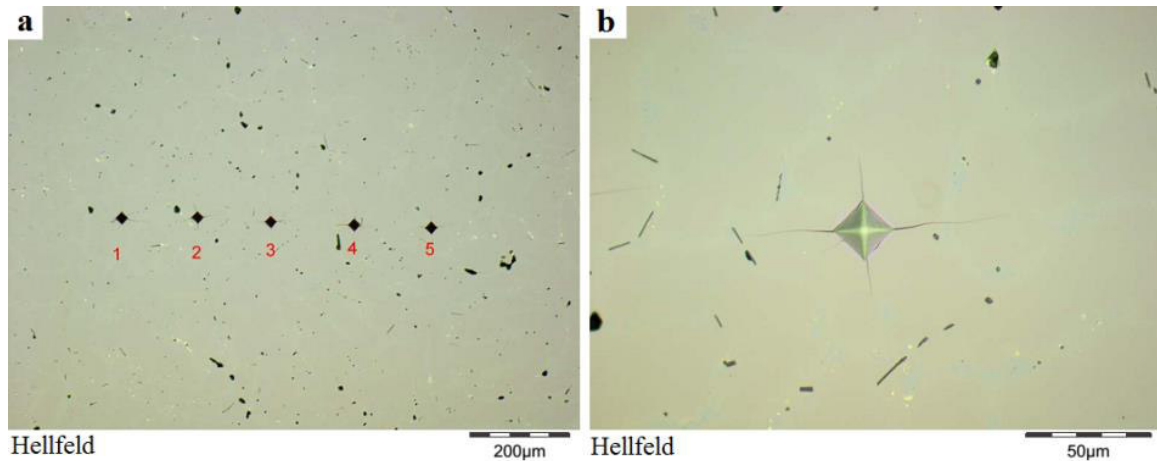


**Figure 58** Micro-Hardness measurements of the *n*-type  $\text{Ti}_{0.3}\text{Zr}_{0.35}\text{Hf}_{0.35}\text{NiSn}$  and *p*-type  $\text{Ti}_{0.26}\text{Sc}_{0.04}\text{Zr}_{0.35}\text{Hf}_{0.35}\text{NiSn}$  material according to Vickers (HV 0.3).

In order to avoid micro cracks in the TE device, it is favorable to use materials with similar thermal expansion coefficients. The thermal expansion coefficient of the *n*- and *p*-type HH material was determined with a heat dilatometer at Fraunhofer Institute for Physical Measurement Technique IPM Freiburg. The temperature dependence of the thermal expansion coefficient revealed no significant change, since the composition of both *n*- and *p*-type materials is very similar, emphasizing the great benefit of site substitution in HH materials.

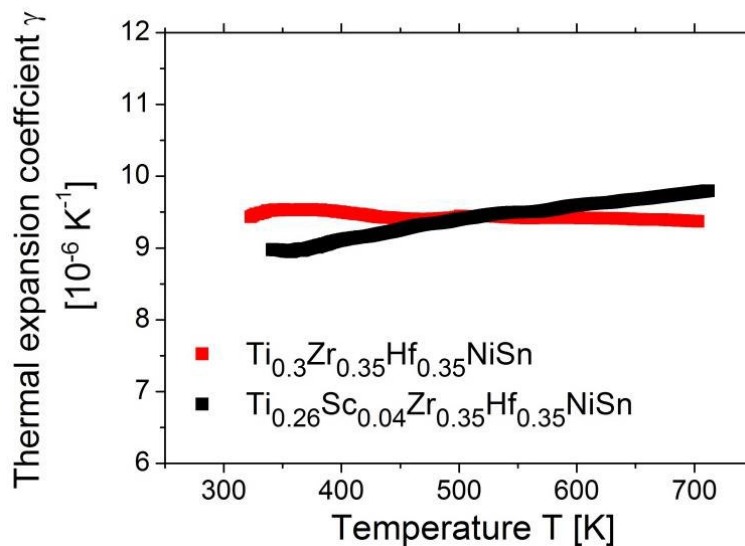


**Figure 59** Measurement of the thermal expansion coefficient  $\gamma$  in the *n*-type  $\text{Ti}_{0.3}\text{Zr}_{0.35}\text{Hf}_{0.35}\text{NiSn}$  and *p*-type  $\text{Ti}_{0.26}\text{Sc}_{0.04}\text{Zr}_{0.35}\text{Hf}_{0.35}\text{NiSn}$  material.

## 7.2 Long-term stability

The long-term stability of the *n*-type  $\text{Ti}_{0.3}\text{Zr}_{0.35}\text{Hf}_{0.35}\text{NiSn}$  and *p*-type  $\text{Ti}_{0.26}\text{Sc}_{0.04}\text{Zr}_{0.35}\text{Hf}_{0.35}\text{NiSn}$  HH material were proven after 500 heating-cooling cycles from 373 to 873 K, lasting about 1700 h. For this purpose, the bars and disks of the 7 days at 950°C annealed *n*-type and *p*-type HH compounds were sealed in evacuated quartz-tubes and subsequently subjected to the temperature profile sketched in Figure 60. The samples were measured on the LSR and LFA, in order to attain the TE properties, and subsequently subjected again to the temperature profile. The duration of one cycle was programmed from room temperature up to 873 K with a heating rate of 10 K/min. The holding time at 873 K was approximately 10 min, before the furnace started to cool down.

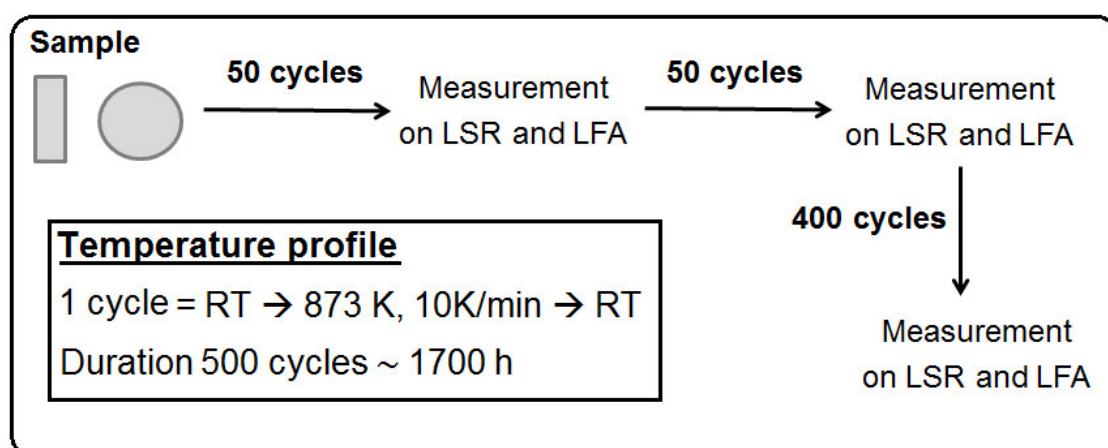


**Figure 60** Cycling conditions of the long-term stability test in the *n*-type  $\text{Ti}_{0.3}\text{Zr}_{0.35}\text{Hf}_{0.35}\text{NiSn}$  and *p*-type  $\text{Ti}_{0.26}\text{Sc}_{0.04}\text{Zr}_{0.35}\text{Hf}_{0.35}\text{NiSn}$  material.

The data of this section was taken from<sup>107</sup>. The crystalline structure of the compounds before and after 500 cycles was determined by PXRD measurements using Cr  $K\alpha_1$  radiation. The obtained X-ray pattern exhibited no change in the crystal structure after the long-term treatment. The change in the lattice parameter in both *n*- and *p*-type HH materials was within the error of the PXRD measurement and can be found in Table 4. The composition determined by EMPA revealed no variation after 500 cycles, and no additional phase impurities were observed (Table 4).

**Table 4 Lattice parameters and chemical compositions determined using energy dispersive X-ray analysis of phase-separated *n*-type  $\text{Ti}_{0.3}\text{Zr}_{0.35}\text{Hf}_{0.35}\text{NiSn}$  and *p*-type  $\text{Ti}_{0.26}\text{Sc}_{0.04}\text{Zr}_{0.35}\text{Hf}_{0.35}\text{NiSn}$  HH compounds.**

	Lattice parameter $a$ [Å]		Composition
	Before cycling	after 500 cycles	
<b><math>\text{Ti}_{0.3}\text{Zr}_{0.35}\text{Hf}_{0.35}\text{NiSn}</math> (<i>n</i>-type)</b>			
Ti-poor phase (HH 1)	6.068(2)	6.070(1)	$\text{Ti}_{0.18}\text{Zr}_{0.40}\text{Hf}_{0.41}\text{NiSn}$
Ti-rich phase (HH 2)	6.012(3)	6.009(7)	$\text{Ti}_{0.65}\text{Zr}_{0.2}\text{Hf}_{0.17}\text{NiSn}$
<b><math>\text{Ti}_{0.26}\text{Sc}_{0.04}\text{Zr}_{0.35}\text{Hf}_{0.35}\text{NiSn}</math> (<i>p</i>-type)</b>			
Ti-poor phase (HH 1)	6.071(7)	6.069(5)	$\text{Ti}_{0.14}\text{Sc}_{0.04}\text{Zr}_{0.4}\text{Hf}_{0.41}\text{NiSn}$
Ti-rich phase (HH 2)	6.041(6)	6.039(4)	$\text{Ti}_{0.62}\text{Sc}_{0.04}\text{Zr}_{0.20}\text{Hf}_{0.17}\text{NiSn}$

The SEM images, shown in Figure 61, revealed the intrinsic phase separation in both *n*- and *p*-type HH compounds. Surprisingly, the dendritic microstructure showed no obvious change in both *n*- and *p*-type materials under the cycling conditions. The PXRD and EMPA results emphasized the extraordinary temperature stability of these HH materials in a moderate temperature range. Due to the high melting point ( $\sim 1720$  K) of this (Ti,Zr,Hf)NiSn HH system the resulting phase separation is stable under the given conditions, which is of utmost importance to maintain low thermal conductivities in these HH materials. The ratio between the Ti-poor HH 1 phase and the Ti-rich HH 2 phase before and after the cycling test was determined to be 75:25 % in both *n*- and *p*-type samples.

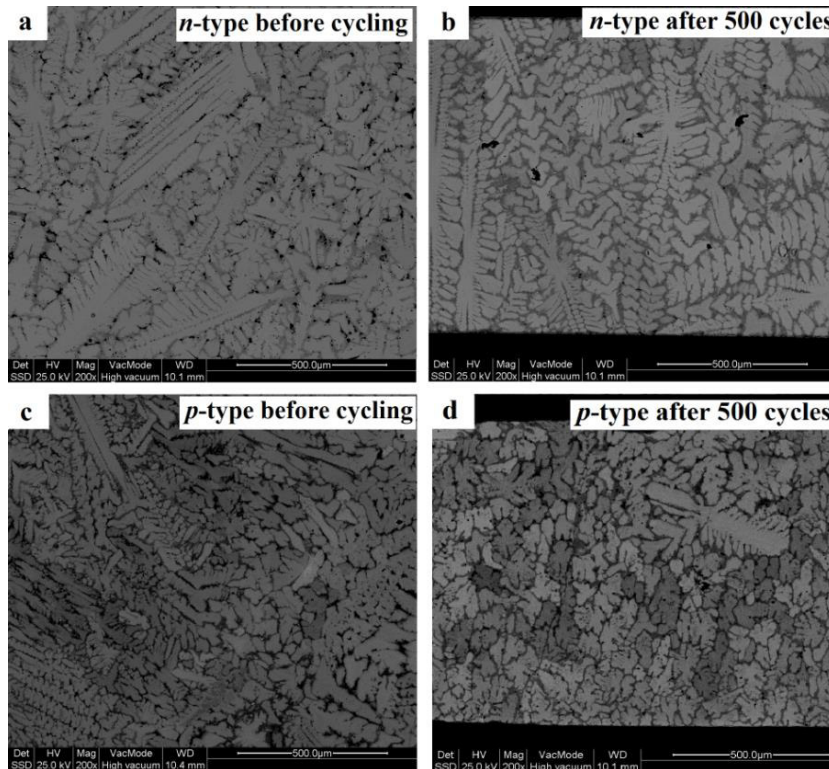


**Figure 61: SEM images of the *n*-type  $\text{Ti}_{0.3}\text{Zr}_{0.35}\text{Hf}_{0.35}\text{NiSn}$  material a) before cycling b) after 500 cycles and of the *p*-type  $\text{Ti}_{0.26}\text{Sc}_{0.04}\text{Zr}_{0.35}\text{Hf}_{0.35}\text{NiSn}$  material after c) before cycling and d) after 500 cycles.**



TEM measurements performed by S. Selle at Fraunhofer Institute for Mechanics of Materials IWM in Halle of *n*-type  $\text{Ti}_{0.3}\text{Zr}_{0.35}\text{Hf}_{0.35}\text{NiSn}$  after the long-term treatment for 500 cycles. Figure 62 indicated dislocation defects (bright areas) in the microstructure. The enlarged section of the microstructure revealed similar element composition of the dislocation and the HH 1 phase. It can be assumed that these lattice defects on the nano scale are responsible for the low thermal conductivity in phase-separated HH materials.

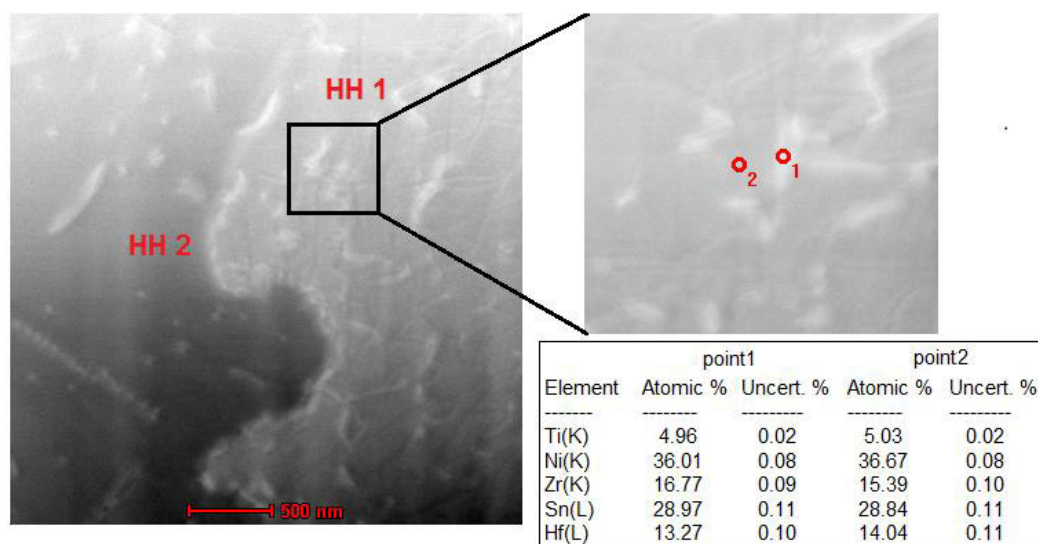


**Figure 62** TEM image of  $\text{Ti}_{0.3}\text{Zr}_{0.35}\text{Hf}_{0.35}\text{NiSn}$  after long-term annealing for 500 cycles, indicating dislocation defects in the microstructure.

The TE properties of the *n*-type  $\text{Ti}_{0.3}\text{Zr}_{0.35}\text{Hf}_{0.35}\text{NiSn}$  HH compound were measured before and after 50, 100 and 500 cycles (1700 h). The temperature dependence of the electrical conductivity  $\sigma$  revealed an increase after 50 cycles owing to the enhanced structural order due to the additional annealing treatment (Figure 63 a)<sup>36</sup>. The Seebeck coefficient  $\alpha$  correlates with  $\sigma$ , and is negative at all temperatures, indicating electrons as the majority charge carriers, The peak value in the thermopower,  $|\alpha| \sim -210 \mu\text{V/K}$ , was attained at 600 K (Figure 63 b). The decrease in  $\alpha$  above 600 K is caused by the thermal excitation of intrinsic carries. The thermal conductivity  $\kappa$  of the parent compound is shown in (Figure 63 c). Due to the improved structural order in this sample,  $\kappa$  increases slightly after 500 cycles. The upturn in  $\kappa$  above 600 K is caused by the excitation of minority carriers. The figure of merit,  $zT$  was evaluated from the measured data. Under consideration of the measurement uncertainty and error propagation, the error in  $zT$  was estimated to 25%. In regard to this acceptable error, the TE performance did not change drastically after 500 cycles. The TE properties are stable since the intrinsic phase separation can be maintained under the cycling conditions.

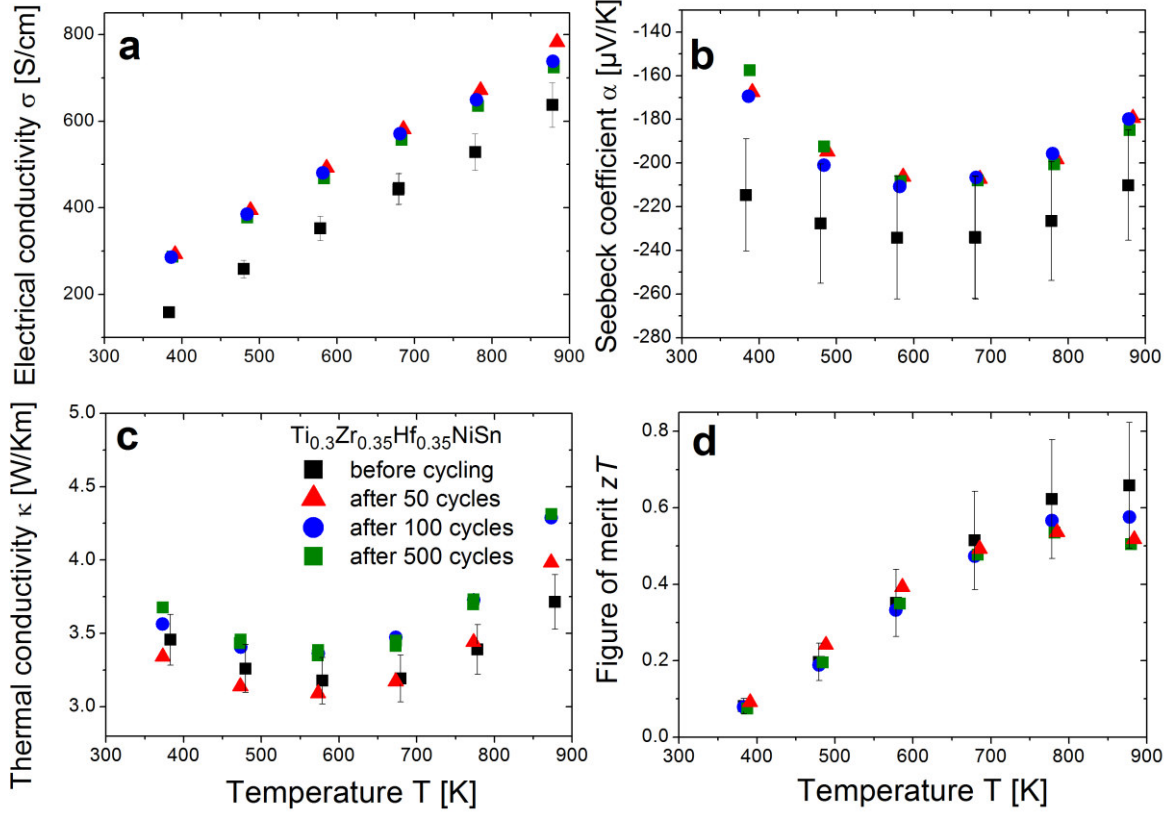


**Figure 63: Temperature dependence of a) electrical conductivity  $\sigma(T)$ , b) Seebeck coefficient  $\alpha(T)$ , c) thermal conductivity  $\kappa(T)$  and d) figure of merit  $zT(T)$  in the  $n$ -type  $\text{Ti}_{0.3}\text{Zr}_{0.35}\text{Hf}_{0.35}\text{NiSn}$  material after 50, 100 and 500 cycles from 300 to 900 K.**

The temperature dependence of the electrical conductivity  $\sigma$  shows semiconducting behavior (Figure 64 a). The  $\sigma$  values for the  $p$ -type are lower than those for the  $n$ -type, caused by the diminished mobility of carriers due to the shift of the Fermi level into the heavier valence band<sup>20</sup>. The site substitution of 4% Sc in the  $n$ -type  $\text{Ti}_{0.3}\text{Zr}_{0.35}\text{Hf}_{0.35}\text{NiSn}$  compound causes a shifting of the Fermi energy into the valence band, resulting in  $p$ -type conductivity in this compound. The Seebeck coefficient  $\alpha$  is positive over the entire temperature range, reaching a maximum of  $\alpha \sim 210 \mu\text{V/K}$  at 600 K (Figure 64 b), which is the highest reported value for a  $p$ -type material based on a (Ti,Zr,Hf)NiSn system. The decrease in the absolute  $\alpha$  above 600 K arises from the usual onset of minority carrier activation. The thermal conductivity  $\kappa$  is further reduced for the  $p$ -type compound ( $\kappa \sim 2.5 \text{ mW/K}$ ) below 600 K (Figure 64 c), owing to higher phonon scattering contribution due to the site substitution. It can be seen in Figure 64 d, that the TE properties exhibit only a weak dependence on cycling conditions (1700 h) and can be improved under the long-term treatment.

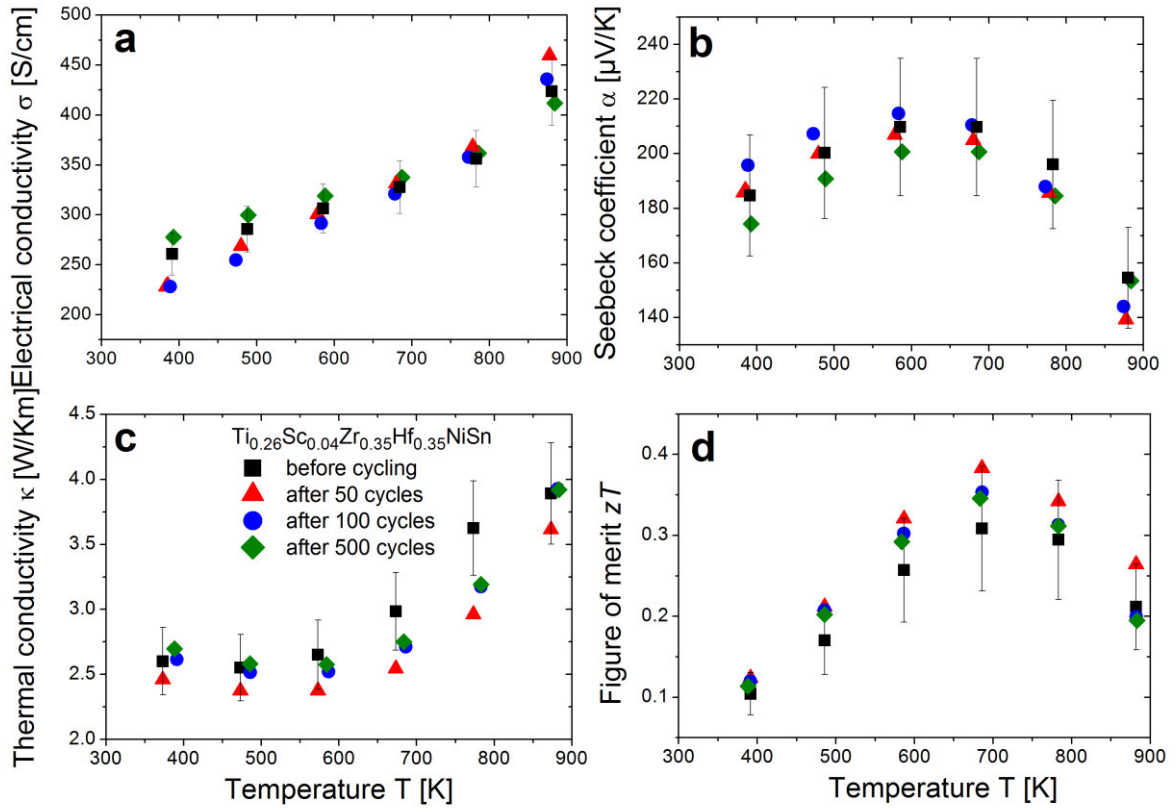


**Figure 64:** Temperature dependence of a) electrical conductivity  $\sigma(T)$ , b) Seebeck coefficient  $\alpha(T)$ , c) thermal conductivity  $\kappa(T)$  and d) figure of merit  $zT(T)$  in the  $p$ -type  $\text{Ti}_{0.26}\text{Sc}_{0.04}\text{Zr}_{0.35}\text{Hf}_{0.35}\text{NiSn}$  material after 50, 100 and 500 cycles from 300 to 900 K.

### 7.3 Spark plasma sintering

Spark plasma sintering (SPS) is a newly developed process – a synthesis and processing technique – which makes possible sintering and compacting powders at low temperatures by applying a high-temperature spark plasma. Although the mechanism of this highly efficient densification process is not understood by now, SPS is frequently used in the fabrication of intermetallic compounds, structural and functional ceramics and composites and nanocrystalline materials<sup>53,84</sup>. In particular for optimal industrial processing of TE devices, this technique is extremely beneficial. Furthermore, the densification of nanopowder can lead to a further reduction in the thermal conductivity due to a higher phonon-scattering at grain boundaries.

In comparison to arc melting synthesis, the manufacturing of the  $n$ -type  $\text{Ti}_{0.3}\text{Zr}_{0.35}\text{Hf}_{0.35}\text{NiSn}$  and  $p$ -type  $\text{Ti}_{0.26}\text{Sc}_{0.04}\text{Zr}_{0.35}\text{Hf}_{0.35}\text{NiSn}$  HH compounds via SPS has been proven. The 7-days at 950 °C annealed samples were ball milled under argon gas atmosphere and subsequently sintered at 1050 °C using the SPS technique. The PXRD measurements of both  $n$ - and  $p$ -type HH compounds revealed the  $\text{C1}_b$  structure and the Bragg reflex splitting, indicating the

coexistence of the different HH phases. The microstructure and element distribution of the spark plasma sintered-samples, shown in Figure 65, are very different from those of the arc melted samples<sup>108</sup>. It can be seen that the dendritic microstructure is lost and various sized grains appear after the SPS synthesis. Furthermore, different impurity phases such as Sn, Ti<sub>6</sub>Sn<sub>5</sub> and Zr<sub>5</sub>Sn<sub>3</sub> were observed, and in the *p*-type compound also Sc segregation. The formation of the binary compounds and the Sc inclusions results from the slow cooling rate in the SPS process.

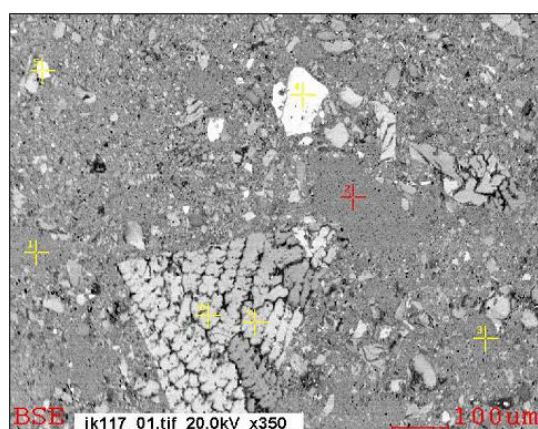


**Figure 65 SEM (BSE) image of the *n*-type Ti<sub>0.3</sub>Zr<sub>0.35</sub>Hf<sub>0.35</sub>NiSn sample after spark plasma sintering.**

The TE properties of the Ti<sub>0.3</sub>Zr<sub>0.35</sub>Hf<sub>0.35</sub>NiSn HH compound after SPS are shown in Figure 66. The temperature dependence of the electrical conductivity  $\sigma$  in the *n*-type compound showed semiconducting behavior after SPS synthesis (Figure 66 a), and slightly increased owing to metallic segregations resulting from the slow cooling. The Seebeck coefficient  $\alpha$  was negative at all temperatures, indicating the intrinsic *n*-type conductivity of the HH compound after SPS and arc melting preparation. The thermopower correlates with  $\sigma$  (Figure 66 b), showing a decline in the maximum  $\alpha$  value from -240 to -227  $\mu\text{V/K}$  after SPS, probably caused by impurity phases. The influence of minority carriers emerging from thermal excitation can be seen above 600 K in both *n*-type samples. As expected, the thermal conductivity  $\kappa$  is significantly reduced in the SPS-sample (Figure 66 c), owing to the higher contributions of phonon scattering at interfaces and impurities. The upturn in  $\kappa$  above 600 K is caused by higher quantities of carriers due to thermal excitation. However, the figure of merit  $zT$  of the *n*-type compound is improved after the SPS, with a maximum  $zT$  value of 0.75 at 773 K (Figure 66 d).

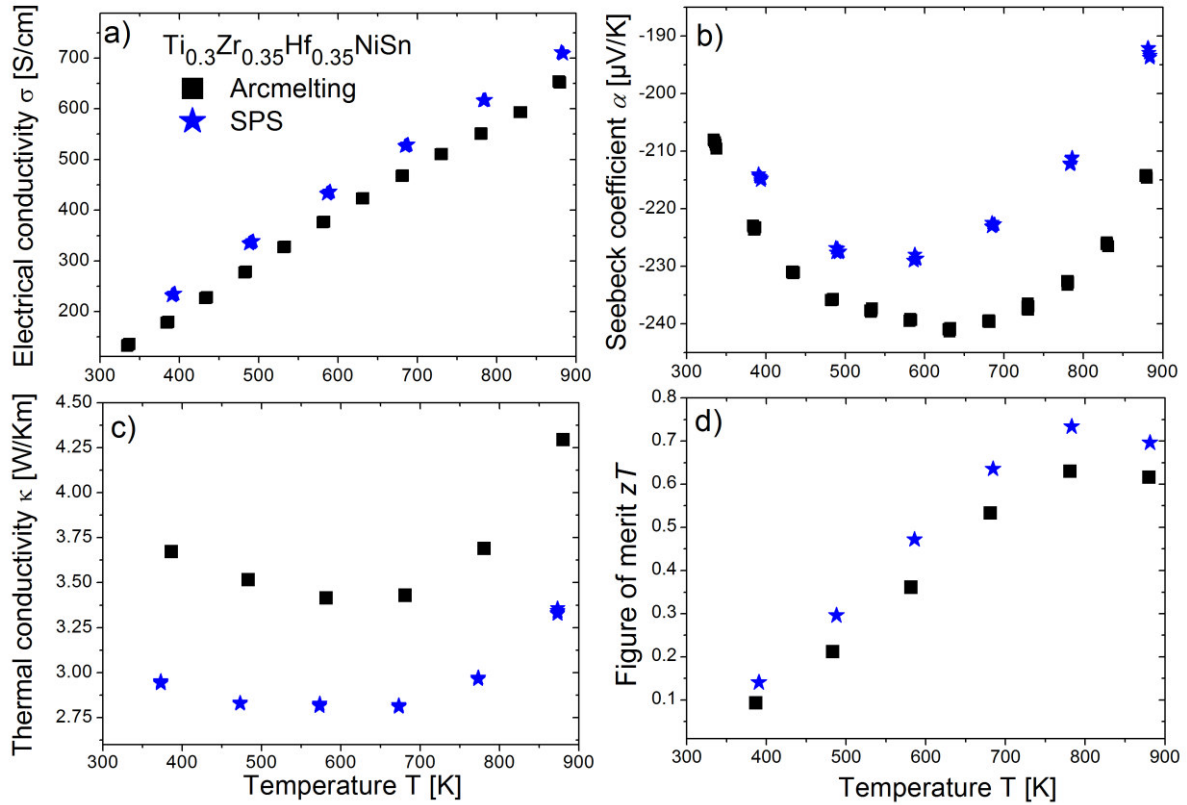


**Figure 66** Temperature dependence of a) electrical conductivity  $\sigma(T)$ , b) Seebeck coefficient  $\alpha(T)$ , c) thermal conductivity  $\kappa(T)$  and d) figure of merit  $zT(T)$  in the *n*-type  $\text{Ti}_{0.3}\text{Zr}_{0.35}\text{Hf}_{0.35}\text{NiSn}$  material after spark plasma sintering from 300 to 900 K.

The thermal transport measurements of the *p*-type  $\text{Ti}_{0.26}\text{Sc}_{0.04}\text{Zr}_{0.35}\text{Hf}_{0.35}\text{NiSn}$  HH compound after SPS are shown in Figure 67. The temperature dependence of the electrical conductivity  $\sigma$  in the *p*-type sample exhibited semiconducting characteristics (Figure 67 a) and is diminished in the SPS-sample. The SPS-compound revealed a strong decline of the Seebeck coefficient  $\alpha$  values with temperatures (Figure 67 b). The reduction of the thermopower results from the Sc segregations in the SPS and thus the loss of *p*-type properties. The temperature dependence of the thermal conductivity  $\kappa$ , shown in Figure 67 c, is also considerably reduced after the SPS, owing to stronger phonon scattering at grain boundaries. The activation of minority carriers can be seen for temperatures above 600 K, causing an increase in  $\kappa$ . The SPS-sample revealed poor TE properties, due to the distinct decrease in the thermopower (Figure 67 d).

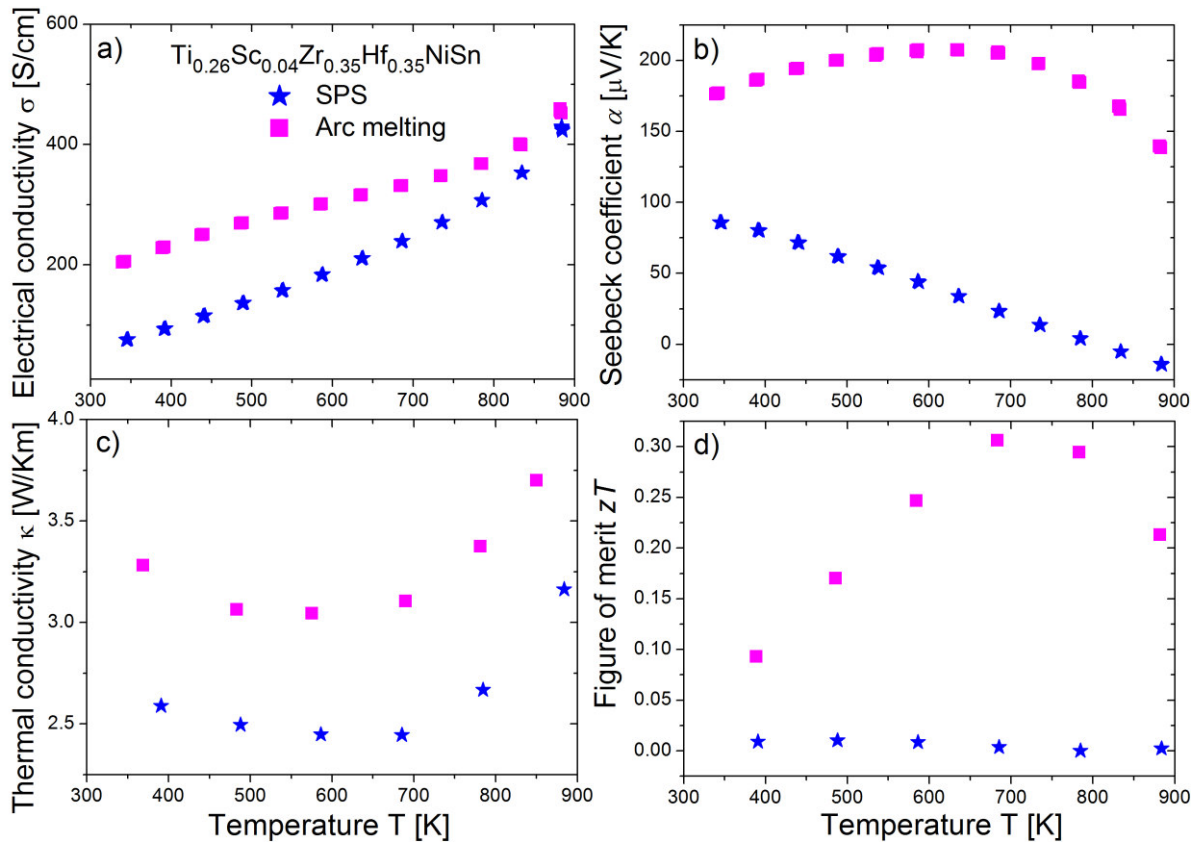


**Figure 67** Temperature dependence of a) electrical conductivity  $\sigma(T)$ , b) Seebeck coefficient  $\alpha(T)$ , c) thermal conductivity  $\kappa(T)$  and d) figure of merit  $zT(T)$  in the  $p$ -type  $\text{Ti}_{0.26}\text{Sc}_{0.04}\text{Zr}_{0.35}\text{Hf}_{0.35}\text{NiSn}$  material after spark plasma sintering from 300 to 900 K.

## 8 Conclusion

This thesis focused on the TE properties of HH compounds based on the *n*-type  $\text{Ti}_{0.3}\text{Zr}_{0.35}\text{Hf}_{0.35}\text{NiSn}$  material. This compound exhibits an intrinsic phase separation into two HH phases under a rapid solidification process. The resulting dendritic microstructure leads to a distinct reduction of the thermal conductivity due to higher phonon scattering contributions and is a key attribute to high TE efficiencies in HH materials. The TE properties and temperature stability of the phase-separated  $\text{Ti}_{0.3}\text{Zr}_{0.35}\text{Hf}_{0.35}\text{NiSn}$  compound were investigated. It was shown, that an appropriate heat treatment for 7 days at 950 °C is necessary to remove binary impurity phases and improve the structural order. An annealing treatment for 21 days at 1000 °C revealed a decrease in the thermal conductivity and thus a further improvement of the TE performance in this sample. The reduction of the thermal conductivity is probably caused by dislocation defects at the nano scale in the microstructure, which might act as additional phonon scatter centers. An increase in the annealing temperature changed the phase fraction ratio in favor of the Ti-rich HH 2 phase, leading to an improvement of the electronic properties ( $\alpha^2\sigma$ ).

Site substitution with donor and acceptor elements in the  $\text{Ti}_{0.3}\text{Zr}_{0.35}\text{Hf}_{0.35}\text{NiSn}$ -system was examined in order to create new *n*- and *p*-type materials, which can operate with high efficiencies in a moderate temperature range. The fabrication of a TE *n*- and *p*-type material pair based on the same parent compound can provide similar TE and mechanical properties, which is enormous favorable for device engineering. The effect of electronic doping with the donor dopants V, Nb and Sb, and with the acceptor dopants Sc, Y and Co was tested. The existence of  $\text{Ni}\leftrightarrow\text{Vac}$  anti-site defects in the HH structure is responsible for the strong intrinsic *n*-type behavior in  $\text{Ti}_{0.3}\text{Zr}_{0.35}\text{Hf}_{0.35}\text{NiSn}$ . The electron doping with V, Nb and Sb significantly increased the electronic properties  $\alpha^2\sigma$  in the moderate temperature regime. The maximum Seebeck coefficient was shifted to higher temperatures, owing to the donor dopant-induced shift of the Fermi energy to higher energies (conduction band). This also led to an effective suppression of minority carriers arise from thermal excitation. The thermal conductivity was reduced owing to higher phonon scattering contributions due to the site substitution and the intrinsic phase separation in the samples. With the combination of enhanced electronic features and reduced thermal conductivities, the TE performance was improved to  $zT$  values of 1 at 773 K with 1% V and 0.97 at 873 K with 0.6% Sb concentration. Furthermore, the applicability of an average mass model was proven for the Nb samples, in order to estimate the optimal carrier concentration for phase-separated HH

compounds<sup>101</sup>. The introduction of the acceptor dopants Sc, Y and Co changed the intrinsic *n*-type conduction in  $\text{Ti}_{0.3}\text{Zr}_{0.35}\text{Hf}_{0.35}\text{NiSn}$  to *p*-type behavior, owing to a shift of the Fermi energy into the valance band. The highest Seebeck coefficients of  $\alpha \sim 210 \mu\text{V/K}$  and  $\alpha \sim 230 \mu\text{V/K}$  about 600 K were attained by substitution of 4% Sc by Ti and 1% Co by Ni, respectively. These are the highest reported  $\alpha$  values for *p*-type materials based on the *MNiSn* system. Y was less sufficient as an acceptor dopant and showed poor TE properties, mainly caused by phase impurities in the Y-based samples. The electrical conductivity was significantly reduced due to diminished carrier mobilities, caused by bipolar conduction in the *p*-type samples. The thermal conductivity could be decreased owing to higher phonon scattering contributions due to the site substitution and the intrinsic phase separation. Since the transport characteristics of the *MNiSn*-based *p*-type HH materials are sophisticated, the *p*-type compounds are less efficient in their TE performance than the *n*-type materials. The best *p*-type properties were observed with Sc, leading to the highest  $zT$  value of 0.3 at 673 K with 4% Sc concentration.

Regarding to commercial applications, the TE compatibility of the exemplary *n*-type  $\text{Ti}_{0.3}\text{Zr}_{0.35}\text{Hf}_{0.35}\text{NiSn}$  and *p*-type  $\text{Ti}_{0.26}\text{Sc}_{0.04}\text{Zr}_{0.35}\text{Hf}_{0.35}\text{NiSn}$  HH compound was investigated. Both *n*- and *p*-type samples revealed similar values in their mechanical properties. The long-term stability of the *n*- and *p*-type materials has been proven after 500 heating-cooling cycles from 373 to 873 K, lasting for 1700 h. Owing to the exceptional temperature stability of the intrinsic phase separation, the dendritic microstructure was maintained and the TE properties remained stable under the cycling conditions. TEM measurements revealed the existence of dislocation defects on the nano scale in the microstructure, which might be also of great importance to other research fields, such as spintronics and magnetocalorics. SPS synthesis achieved an improvement in the *n*-type material, resulting from a further reduction in the thermal conductivity. The TE properties of the *p*-type compound were strongly deteriorated after SPS, due to Sc segregation in the sample caused by the slow cooling rate in the SPS process. This work emphasize that phase-separated HH compounds are extraordinarily suitable TE materials for the moderate temperature regime; they will fulfill all the requirements for commercial applications, ranging from environment-friendliness, low cost materials via long-term stability and industrial processability. In particular, the temperature stable eutectic microstructure can establish an entirely new area of research, where the intrinsic phase separation can be individually tailored to fulfill desired TE properties<sup>86</sup> and guide the TE research to further improvements of the TE efficiencies in HH compounds.



## Bibliography

1. F. R. Stabler and J. Yang. *J.Elect.Mat.* **2009**, 38, 1245-1251.
2. [www.eere.energy.gov/waste\\_heat\\_recovery](http://www.eere.energy.gov/waste_heat_recovery).
3. C. Chau and K.T. Yu. *Energ Convers Manage.* **2009**, 50, 1506-1512.
4. T. M. Tritt. *Annu. Rev. Mater. Res.* **2011**, 41, 433-448.
5. <http://www.cleargas.org/> [Online] **2007**.
6. Reuters, *Spiegel online* 06/24/2013, CO<sub>2</sub>-Emissionen: EU setzt schärfere Grenzwerte ab.
7. J. Vázquez, M. A. Sanzi-Bobi, R. Palacios and A. Arenas. *Proceedings of the 7th European Workshop on Thermoelectrics* **2002**.
8. T. J. Seebeck and A. Koenigl. *Akad. Wiss. Berlin.* **1822**, 265.
9. H. J. Goldsmid, *Introduction to Thermoelectricity*. Springer Heidelberg Berlin, **2010**.
10. J. Sommerlatte, K. Nielsch and H. Böttner. *Physik Journal.* **2007**, 5.
11. E. Altenkirch. *Physikalische Zeitschrift.* **1911**, 12, 920-924.
12. E. Altenkirch. *Physikalische Zeitschrift.* **1909**, 10, 560-580.
13. A. Ioffe. *Semiconductor Thermoelements and Thermoelectric Cooling.* 1957.
14. A. Ioffe. *Scientific American* **1958**, 199, 31-37.
15. R. W. Douglas and H. J. Goldsmid. *J. Appl. Phys.* **1954**, 386, 458.
16. D. M. Rowe. *Thermoelectric Handbook:macro to Nano.* CRC Press Boca Raton, **2006**.
17. G. S. Nolas, J. Sharp and H. J. Goldsmid. *Thermoelectrics: Basic Principles and New materials developments.* Springer New York, **2001**.
18. J. R. Scootsman, D. Y. Chung and M. G. Kanatzidis. *Angew. Chem.* **2009**, 48, 8616-8639.
19. G. Slack. *CRC Handbook of Thermoelectrics*, **1995**.
20. G. J. Snyder and E. S. Toberer. *Nat Mater.* **2008**, 7, 105-114.
21. M. S. Dresselhaus. *Adv.Mater.* **2007**, 19, 1043-1053.
22. L. D. Hicks and M. S. Dresselhaus. *Phys.Rev.B.* **1993**, 47, 12727-31.
23. G. S. Nolas, J. Poon and M. G. Kanatzids. *MRS Bull.* **2006**, 31, 199-205.
24. Thermoheulser Project, Robert Bosch GmbH **2011**.
25. K. Nielsch, J. Bachmann, J. Kimling and H. Böttner. *Adv. Energy Mater.* **2011**, 1, 713-731.

26. P. H. Ngan, D. V. Christensen, G. J. Snyder, L. T. Hung, S. Linderoth and N. Pryds. *Phys. Status Solidi A*. **2013**, 9-17.
27. G. J. Snyder and T.S. Ursell, *21st International Conference on Thermoelectrics*. **2002**.
28. G. J. Snyder. *Appl. Phys. Lett.* **2004**, 84, 2436-2438.
29. B. C. Sales. *Science*. **2002**, 295, 1248-1249.
30. J. Yang and T. Caillat. *MRS Bull.* **2006**, 31, 224-229.
31. Ch. Kittel, *Einführung in die Festkörperphysik*. Oldenbourg München, **2006**.
32. H. Ibach. *Festkörperphysik*. Springer Heidelberg Berlin, **1999**.
33. L. Pollmann. *PC 3 Vorlesung, Freie Universität Berlin*. **2005**.
34. J. P. Heremans, V. Jovovic, E. S. Toberer, A. Saramat, K. Kurosaki, A. Chaoenphakdee, S. Yamanaka and G.J. Snyder. *Science*. **2008**, 321, 554-557.
35. S. R. Culp, S. J. Poon, N. Hickman, T. M. Tritt and J. Blumm. *Appl. Phys. Lett.* **2006**, 88, 042106.
36. S. Chen and Z. Ren. *Materials Today*. **2013**, 16, 387-394.
37. W. Zeier. "High temperature thermoelectric transport in quaternary copper selenides and ternary Zintl-antimonides". *Dissertation*. 2013.
38. Y. Pei, H. Wang and G.J. Snyder. *Adv Mater.* **2012**, 1-11.
39. E. S. Toberer, A. Zevalkink and G. J. Snyder. *J. Mater. Chem.* **2011**, 21, 15843.
40. H. Muta, T. Kanemitsu, K. Kurosaki and S. Yamanaka. *J. Alloys Compd.* **2005**, 469, 50-55.
41. J. Callaway. *Phys. Rev.* **1960**, 120, 1149-1154.
42. E. Steigmeier and B. Abeles. *Phys. Rev.* **1964**, 136, 1149-1155.
43. M. Zebarjadi, K. Esfarjani, M. S. Dresselhaus, Z.F. Ren and G. Chen. *Energy Environ. Sci.* **2012**, 5, 5147-5162.
44. C. Yu, T.-J. Zhu and R.-Z. Shi *Acta Materialia*. **2009**, 57, 2757-2764.
45. S. Ouardi, G. H. Fecher, C. Felser, S. Ueda and K. Kobayashi. *Phys Rev B*. **2012**, 86, 0451116.
46. J. P. Heremans, B. Wiendlocha and A. M. Chamoire. *Energy Environ. Sci.* **2012**, 5, 5510-5530.
47. Y. Pei, A. LaLonde, S. Iwanaga and G. J. Snyder. *Energy Environ. Sci.* **2011**, 4, 2085-2089.

48. J. W. Simonson, D. Wu, W.J. Xie, T. M. Tritt and S.J. Poon. *Phys. Rev. B.* **2011**, 83, 235211-9.
49. Y. Pei, X. Shi, A. LaLonde, H. Wang, L. Chen and G.J. Snyder. *Nature.* **2011**, 473, 66-69.
50. D. Cahill, S. Watson and R. Pohl. *Phys. Rev. B.* **1992**, 46, 6131–6140.
51. T. Graf, C. Felser and S. Parkin. *Prog. Solid State Ch.* **2011**, 3, 1-50.
52. H. J. Goldsmid and A.W. Penn. *Phys. Lett A.* **1968**, 27, 523.
53. M. Nygren and Z. Shen. *Key Eng. Mat.* **2004**, 264, 719-24.
54. W. Jeitschko. *Met.Trans.* **1970**, 1, 3159-3162.
55. C. Felser, G.H. Fecher, B. Balke. *Angew.Chem.* **2007**, 46, 668-699.
56. S. Chadov, X. Qi, J. Kübler, G.H. Fecher, C. Felser, S.C. Zhang. *Nat.Mat.* **2010**, 9, 541-545.
57. W. Wunderlich, X. Motoyama. *Mater. Re. Soc. Symp. Proc.* **2009**, 1129, 1128-U01-10.
58. H. C. Kandpal, C. Felser, R. Seshadri. *J.Phys.D: Appl.Phys.* **2006**, 39, 776-785.
59. S. Ögüt and K. Rabe. *Phys.Rev.B.* **1995**, 51, 10443.
60. J. Yang, H. Li, T. Wu, W. Zhang, L. Chen and J. Yang. *Adv.Funct.Mater.* **2008**, 18, 2880.
61. J. Tobola and J. Pierre. *J.Alloys Compd.* **2000**, 296, 243.
62. F. G. Aliev, N. B. Brandt, V. V Moshchalkov, V. V. Kozyrkov, R. V.Skolozdra and A. I. Belogorokhov. *Phys. B:Condens. Matter.* **1989**, 75, 167.
63. S. Ouardi, G.H. Fecher, B. Balke, X. Kozina, G. Stryganyuk and C. Felser. *Phys.Rev.B.* **2010**, 82, 085108.
64. H. J. Noh, T. U. Nahm, J. Y. Kim, W. G. Park, S. J. Oh, J.-P. Hong and C.-O. Kim. *Solid State Commun.* **2000**, 116, 137-141.
65. P. Larson, S. D. Mahanti and M. G. Kantzidis. *Phys.Rev.B.* **2000**, 62, 12754.
66. P. Qiu, J. Yang, X. Huang, X. Chen and L. Chen. *Appl.Phys.Lett.* **2010**, 96, 152105.
67. J. O. Sofo and G. D. Mahan. *Phys.Rev.B.* **1994**, 49, 4565.
68. R. S. Culp, J. W. Simonsom, S. J. Poon, V. Ponnambalam, J. Edwards and T. M. Tritt. *Applied Physic Letters.* **2008**, 93, 022105.
69. S. Sakurada and N. Shutoh. *Appl. Phys. Lett.* **2005**, 86, 082105.
70. J. Tobola, J. Pierre, S. Kaprzyk, R.V. Skolozdra and M.A. Kauacou. *J.Phys.:Condens. Matter.* **1998**, 10, 1013-1032.
71. S. Ouardi, G.H. Fecher and C. Felser. *Appl. Phys. Lett.* **2010**, 97, 252113.

72. G. Joshi, T. Dahal, S. Chen, H. Wang, J. Shiomi, G. Chen and Z. Ren. *Nano Energy*. **2013**, 2, 82-87.
73. X. Yan, W. Liu, S. Chen, H. Wang and Z. Ren. *Adv. Energy. Mater.* **2013**, 3, 1195-1200.
74. C. Uher, J. Yang, S. Hu, D.T. Morelli, G.P. Meisner. *Phys.Rev.B*. **1999**, 59, 8615-21.
75. S. J. Poon, D. Wu. *J. Mater. Res.* **2011**, 26, 2795-2802.
76. W. Xie, A. Weidenkaff, X. Tang, J. Poon, T. M. Tritt. *Acta Mater.* **2013**, 61, 2087-2094.
77. J. P. Makongo, D. K. Misra, X. Zhou, A. Pant, M. R. Shabetai, X.Su, C. Uher, K. L. Stokes, P. F. P. Poudeu. *J.Am.Chem.Soc.* **2011**, 133, 18843.
78. H. Hohl, A. Ramirez, C. Goldmann, G. Ernst, B. Wölfing, E. Bucher. *J. Phys.:Condens. Matter.* **1999**, 11, 1697-1709.
79. D.-Y. Jung, K. Kurosaki, C.-E. Kim, H. Muta and S. Yamanaka. *J. Alloys Compd.* **2010**, 489, 328-331.
80. S. Populoh, M. H. Aguirre, O. C. Brunko, K. Galazka, X. Lu and A. Weidenkaff. *Scripta Mater.* **2012**, 66, 1073-1076.
81. K. Bartolomé, B. Balke, D. Zuckermann, M. Köhne, M. Müller, K. Tarantik, J. König. *J. Electron. Mater.* **2013**, DOI 10.1007/s11664-013-2863-x.
82. C. Yu, K. Xiao, J. Shen, S. Yang and X. Zhao. *Electr Mater.* **2010**, 39, 2008.
83. K. Kurosaki, T. Maekawa, H. Muta and S. Yamanaka. *J Alloys Compd.* **2009**, 397, 296.
84. J. E. Garay. *Annu.Rev.Mater.Res.* **2010**, 40, 445-68.
85. M. Schwall and B. Balke. *Phys. Chem. Chem. Phys.* **2013**, 15, 1868-1872.
86. M. Koehne, T. Graf, H.-J. Elmers, Semi-Heusler/Heusler alloys having tailored phase separation. *US patent 0156636*, Jun. 20, **2013**.
87. U. Akerlind and H. Fredriksson. *Solidification and Crystallization Processing in Metals and Alloys*. John Wiley & Sons, Ltd., **2012**.
88. H. Jones. *J Mater Sci.* **1984**, 19, 1043-1076.
89. E. Riedel. *Moderene Anorganische Chemie*. de Gruyter GmbH & Co, Berlin. **2007**.
90. H. Berns, W. Theisen. *Eisenwerkstoffe:Stahl und Gusseisen* . Springer-Verlag, Berlin-Heidelberg. 2013.
91. G. Gottscheid. *Materialwissenschaften und Werkstofftechnik* Springer-Verlag, Berlin. **2014**.
92. N. Shutoh, S. Sakurada, N. Kondo, N. Takezawa. *Thermoelectric material and thermoelectric element*. *US patent 0037199A1*, Feb 16, **2012**.

93. S. Sakurada, N. Shutoh, S. Hirono, *Thermoelectric material and thermoelectric device. US patent 7,745,720 B2*, June 29, **2010**.
94. H. Xie, H. Wang and Y. H. Pei, *Adv. Funct. Mater.* **2013**, 23, 5123-5128.
95. K. Kurosaki, H. Muta and S. Yamanaka. *J. Alloys Compd.* **2004**, 384, 51-56.
96. H. H. Xie, J. L. Mi, L. P. Hu, N. Lock, M. Christensen, C. G. Fu, B. Brummerstedt Iversen, X.B. Zhao and T.J. Zhu. *Cryst. Eng. Comm.* **2012**, 14, 4467-4471.
97. P. Schnabel. *Die Elektronik-Fibel.* **2007**.
98. Y. Kimura, T. Tanoguchi and T. Kita. *Acta Materialia.* **2010**, 58, 4354-4361.
99. I. Skovsen, L. Bjerg, M. Christensen, E. Nishibori, B. Balke, C. Fesler and B.B. Iversen. *Dalton Trans.* **2010**, 39, 10154-10159.
100. Y. Stadnyk, A. Horyn, V.V. Romaka, Y. Gorelenko, L.P. Romaka and E.K. Hill. *J. Solid State Chem.* **2010**, 183, 3023-3028.
101. J. Krez, J. Schmitt, G.J. Synder, C. Felser, W. Hermes and M. Schwind, **2014**, submitted.
102. P.-J. Lee and L.-S. Chao. *J. Alloys Compd.* **2010**, 504, 192-196.
103. J. H. Goldsmid. *Introduction to thermoelectrics.* Springer-Verlag, Heidelberg. **2010**.
104. V. A. Romaka, M. G. Shelyapina, Y. K. Gorelenko, D. Fruchart, Y. V. Stadnyk, L. P. Romaka and V. F. Chekurin. *Semiconductors.* **2006**, 40, 655-661.
105. H.-H. Xie, C. Yu, B. He, T.-J. Zhu, X.-B. Zhao. *J Electron Mat.* **2012**, 41, 1826-1830.
106. E. Hatzikraniotis, K. T. Zorbas, I. Samaras, Th. Kyratsi, K. M. Paraskevopoulos. *J. Electron. Mater.* **2010**, 39, 2112-2116.
107. J. Krez, B. Balke, C. Felser, W. Hermes and M. Schwind, **2014**, submitted.
108. K. Kurasaki, T. Maekawa, H. Muta and S. Yamanaka. *J. Alloys and Compd.* **2005**, 397, 296-299.

# Curriculum Vitae

## Persönliches

Julia Krez

Diplom-Chemikerin

Geburtsdatum/-ort:

5. Oktober 1985; Kapal / Kasachstan

## Promotion

06/2011 – andauernd

Dissertation in Anorganischer Chemie bei Prof. Dr. C. Felser,  
Johannes Gutenberg-Universität, Mainz  
Thema: „Thermoelektrische Eigenschaften in phasenseparierten halb-Heusler  
Materialien“

## Studium

05/2010 – 01/2011

Diplomarbeit in Anorganischer Festkörperchemie bei Prof. Dr. G. Kickelbick,  
Universität des Saarlandes  
Thema: „Oberflächenfunktionalisierung von Seltenerd-Nanobausteinen und  
ihr Photolumineszenzverhalten“

2005 – 2011

Studium der Chemie/Diplom, Universität des Saarlandes  
Schwerpunkt in Anorganischer Festkörperchemie, Physikalischer und  
Makromolekularer Chemie  
**Abschluss:** Diplom Chemie mit Note „sehr gut mit Auszeichnung“

## Schulbildung

1996 – 2005

Gymnasium am Krebsberg in Neunkirchen/Saar

1992 – 1996

Grundschule, Landsweiler-Reden

## Auslandsaufenthalt

05/2013 – 10/2013

Northwestern University (Chicago, USA) bei Prof. Dr. M. G. Kanatzidis  
Mitarbeit am US-Forschungsprojekt „Towards Self formed Nanostructured  
Bi<sub>2</sub>Te<sub>3</sub>-based materials“  
- Synthese thermoelektrischer Materialien via Spark Plasma Sintering

10/2010

Technische Universität Wien (Österreich),  
BET-Messungen am Institut für Materialchemie bei Prof. Dr. U. Schubert

## Berufspraxis

2011-2014

Mitarbeit am BMBF-Verbundprojekt TEG2020

2011-2014

Mitglied der Graduiertenschule *Materials Science in Mainz MAINZ*

2012-2014

Forschungsarbeiten am Max-Planck-Institut für Chemische Physik fester Stoffe,  
Dresden

2011-2012

Betreuung von Bachelorstudenten der Chemie und Biologie, Johannes  
Gutenberg-Universität, Mainz

03/2011-06/2011

Wissenschaftliche Mitarbeiterin am Institut für Anorganische Festkörperchemie,  
Albert-Ludwigs-Universität, Freiburg

2009 – 2011

Studentische Hilfskraft an der Universität des Saarlandes

2008 – 2011

Nebenberufliche Tätigkeit, Saarland Heilstätten GmbH

## Sonstiges

- 2013 Ehrenamtliches Mitglied der Deutschen Hirntumorhilfe e.V.  
2009 –2011 Stellvertretende Sprecherin des „JungChemikerForum“ der Gesellschaft Deutscher Chemiker e.V.  
2008 Mitglied der Gesellschaft Deutscher Chemiker e.V.  
2008 Sachkunde gemäß §5 der Chemikalien-Verbotsverordnung

## Sprachkenntnisse

Englisch fließend in Wort und Schrift  
Russisch gute Kenntnisse  
Französisch Grundkenntnisse  
Deutsch Muttersprache

## Konferenzen/Vorträge

- 2014 DPG-Frühjahrstagung, TU Dresden, Dresden (Vortrag)  
2013 International Conference on Thermoelectrics, Kobe, Japan (Poster)  
2013 Hemdsärmelkolloquium, Freiburg  
2012 Studenten Seminar Graduiertenschule „MAINZ“, Cambridge, England (Vortrag)  
2012 International Conference on Thermoelectrics, Aalborg, Dänemark (Poster)

## Qualifikationen

- 2014 New Business Development, GdCH Tagung, Frankfurt a.M.  
2013 Application and Assessment, Graduiertenschule MAINZ  
2013 Lösungsorientiertes Konfliktmanagement, Johannes Gutenberg-Universität Mainz  
2013 Presence-Performance-Impact, Graduiertenschule MAINZ  
2012 Seminar „Wärmeleitfähigkeit“, Linseis, TU Bochum  
2012 Summer school „Superconductivity“, IBM, San Jose, USA  
2011 Winter school „Nanomaterials for Energy Application“, Duisburg  
2011 Publishing in English, Max-Planck-Institut für Polymerforschung, Mainz

## Publikationen

- 2014 **J.Krez**, B.Balke, C.Felser. Long-term stability of phase-separated half-Heusler compounds, submitted  
2014 **J. Krez**, J. Schmitt, G.J. Snyder and C. Felser. Optimization of carrier concentration in phase-separated half-Heusler compounds, submitted  
2013 L.M. Schoop, **J. Krez**, R. Cava,  $\beta$ -HfCuGe - A new polymorph of HfCuGe with a novel structure type, *J. Solid State Chem.*, 199 (2013), 66-70